DLR-IB-AS-BS-2020-91

Investigation of Benchmark
Turbulent Flows

Forschungsbericht

Autor
Akshaya Govindan Nair Rajendran

DLR Deutsches Zentrum für Luft- und Raumfahrt

Bericht des Instituts für Aerodynamik und Strömungstechnik
Report of the Institute of Aerodynamics and Flow Technology

DLR-IB-AS-BS-2020-91

Investigation of Benchmark Turbulent Flows

Akshaya Govindan Nair Rajendran

Herausgeber:
Deutsches Zentrum für Luft- und Raumfahrt e.V.
Institut für Aerodynamik und Strömungstechnik
Lilienthalplatz 7, 38108 Braunschweig

ISSN 1614-7790

Stufe der Zugänglichkeit: 1
Braunschweig, im Juli 2020

Institutsdirektor:
Prof. Dr.-Ing. habil. C.-C. Rossow

Verfasser:
Akshaya Govindan Nair Rajendran

Abteilung: Center of Computer Applications in Aerospace Science and Engineering

Abteilungsleiter:
Prof. Dr. S. Görtz

Der Bericht enthält:
80 Seiten
39 Bilder
6 Tabellen
37 Literaturstellen

Declaration

I, Akshaya Govindan Nair Rajendran, hereby declare that the project work entitled **'Investigation of Benchmark Turbulent Flows'** is a record of bonafide research carried out by me following the stipulated guidelines under the supervision of Dr. habil. Stefan Langer, that is submitted to the Deutsches Zentrum für Luft- und Raumfahrt (DLR), Braunschweig. All sources of information referred to in this work are acknowledged with reference to the respective authors. I further declare that the thesis has not previously formed the basis for the award of any degree or other similar titles of recognition.

Braunschweig,
February 14, 2020

Akshaya Govindan Nair Rajendran
4868747

Abstract

Several benchmark test cases have been implemented over the last few years in furtherance of providing reference results for turbulent flows with high Reynolds number. With these test cases, information regarding the behavior study of accuracy and the solution methods of the available codes that were employed for solving the Reynolds-averaged Navier-Stokes equations (RANS) were investigated.
The relevant benchmark test cases that are admissible to this thesis are:

- 2D Finite Flat Plate,
- 2D NACA 0012 Airfoil,
- 3D Modified Bump,
- 3D Hemisphere Cylinder, and
- 3D ONERA M6 Wing.

The suitable parameters for all the test cases are accessed from the **"Turbulence Modeling Resource"** (TMR) website [1] of National Aeronautics and Space Administration (NASA).
The thesis contains a thorough analysis of the test cases and it is done by first extracting the meshes from the website through a FORTRAN code by which a sequence of meshes ranging from coarse to fine is generated. These meshes are excerpted to a data format that can be used for computations by the DLR-TAU (Triangular Adaptive Upwind) code [2]. The TAU code is a software for performing numerical computations especially with flows around complex geometries. Chap. 4 addresses the solution methodologies, all of which are fed into the code. Furthermore, RANS equations are solved for these meshes and the results from the computations are studied focusing on its behavioral properties.

Contents

List of Figures

List of Tables

List of Symbols

Latin Symbol	Description	Unit
$\bar{\bar{A}}$	Jacobian flux	
a	speed of sound	m/s
div (u)	divergence of u $\left(= \vec{\nabla} \cdot \vec{u} = \frac{\partial u}{\partial x} + \frac{\partial v}{\partial y} + \frac{\partial w}{\partial z}\right)$	–
D	computational domain	–
e_i	standard orthonormal basis of $\mathbb{R}^m$	J
E	specific total energy	J/kg
f	flux integral across surface **S**	–
grad T	gradient of scalar T $\left(= \vec{\nabla} \cdot T = \left[\frac{\partial T}{\partial x}, \frac{\partial T}{\partial y}, \frac{\partial T}{\partial z}\right]\right)$	–
H	total (stagnation) enthalpy	J
$\mathcal{H}$	numerical flux function (Roe scheme)	–
$I_{M_k}^{M_{k-1}}$	interpolation operator	–
M	triangulation of domain D	–
Ma	Mach number	–
$\widehat{mom}_j$	momentum of flow in x_j $\left(:= \rho u_j\right)$	kg · m/s
$\mathcal{N}$	neighbors of a point	–
n	unit normal projecting outward	–
Pr	Prandtl number	–
$P_{M_k}^{M_{k-1}}$	projection operator	–
Prec	Preconditioner	–
p	static pressure	atm
Re	Reynolds number	–
$\Re$	universal gas constant $(= 8.314)$	J/mol · K
$\mathbb{R}$	set of real numbers	–
R	residual	–
$\mathcal{S}$	strain rate tensor	s^{-1}
T	static temperature	K
$\bar{T}$	Sutherland's constant $(= 110.4)$	K
t	temporal component	s
$\|u\|_2$	2-norm of vector of u $\left(= \sqrt{\vec{u} \cdot \vec{u}}\right)$	–
u_i	velocity of general flow variables	m/s
u_1, u_2, u_3	Cartesian velocity components	m/s
V_D, R_D	integral operators	–
W	vector field of conservative variables	–
$\mathcal{X}$	space of trial solutions	–
x, y, z	Cartesian coordinate system	m

Greek Symbol	**Description**	**Unit**
α	angle of attack	$^\circ$
γ	ratio of specific heat	$-$
Δ	difference operator	$-$
δ	Kronecker delta	$-$
θ	heat flux	W
κ	thermal conductivity coefficient	$\mathrm{W/m \cdot K}$
Λ	eigenvalues of diagonal matrix	$-$
μ	dynamic viscosity coefficient	$\mathrm{kg/m \cdot s}$
ν	kinematic viscosity	$\mathrm{m^2/s}$
ρ	density	$\mathrm{kg/m^3}$
τ	viscous shear stress tensor	$\mathrm{N/m^2}$
Ω	vorticity	$\mathrm{s^{-1}}$

Subscripts	**Description**
bdry	boundary
c	convective part
ef	entropy fix
eff	effective quality
elem	elements
i, *j*, *k*	nodal point index
l	laminar
mean	mean flow
prec	preconditioning
Roe	Roe averaged variables
ref	reference value
SA	Spalart-Allmaras turbulence model
t, **turb**	turbulent
v	viscous part
∞	freestream conditions

Superscripts	**Description**
comp	compact discretization
n	current time level
$n+1$	new time level
Roe	usage of Roe averaged variables
T	transpose
$\hat{}$	denoting estimator
-1	inverse

Miscellaneous	**Description**
Chap.	Chapter
Eq. / Eqn.	Equation

Fig.	Figure
Ref.	Refer
Sec.	Section

Abbreviations

AoA	Angle of attack
CAD	Computer-Aided Design
CFD	Computational Fluid Dynamics
CFL	Courant-Friedrichs-Lewy
CGNS	CFD General Notation System
DLR	Deutsches Zentrum für Luft- und Raumfahrt (German Aerospace Center)
DNS	Direct Numerical Simulation
FAS	Full Approximation Scheme
FORTRAN	Formula Translation
FVM	Finite Volume Method
GG	Green-Gauss
LES	Large-Eddy Simulation
LU-SGS	Lower-Upper Symmetric Gauss-Seidel
NACA	(now NASA) The National Advisory Committee for Aeronautics, USA
NASA	National Aeronautics and Space Administration, USA
ONERA	Office National d'Etudes et de Recherches Aerospatiales (National Institute for Aerospace Studies and Research), France
pde	partial differential equations
RANS	Reynolds-averaged Navier-Stokes
RK	Runge-Kutta
SA	Spalart-Allmaras
SA-neg	Negative Spalart-Allmaras
SST	Shear stress Transport
TAU	Triangular Adaptive Upwind
TMR	Turbulence Modeling Resource
TSL	Thin shear layer
TVD	Total Variation Diminishing
$2D$	Two dimensional
$3D$	Three dimensional

Chapter 1

Introduction

Computational Fluid Dynamics (CFD) had started gaining its significance in the early 1970's. CFD was said to entail physics in addition to numerical mathematics along with the applications of computer sciences in the interest of simulating fluid flows. The evolution of the field was largely connected with that of computer technology from the existing powerful mainframes. With this development, the possibility of achieving the solution for Euler equations (beginning with two-dimensional and then proceeding later to three-dimensional) became feasible. As a result of the ever-increasing speed of the supercomputers alongside the improvement of diverse numerical acceleration techniques namely multigrid, computations for the inviscid flows even for a complete aircraft configuration was made possible. The increasing demand for the simulation of viscous flows using the Navier-Stokes equations led to the advancement of turbulence models that had various degrees of numerical complexity followed by its accuracy.

As a consequence of expanding complexity and the demand for the exactness of the flow simulations, grid generation methods were accentuated. The fairly straightforward structured meshes were constructed by using either algebraic methods or partial differential equations (pde) but when the complexity of the configurations increased it was essential to break the grids into numerous simpler blocks with similar topology (*multi-block approach*). This led to facilitate the non-matching interfaces to exist between the blocks so that the constraints affecting a single block grid-generation can be alleviated. The high computational time needed by the structured grids were met with the buildup of unstructured meshes. Sequentially, solution methodologies were introduced on these grids to obtain results by computations.

This thesis provides a run-through of all the concepts mentioned above in the forthcoming chapters. The basic idea of CFD is to solve for fluid flows, its equations of motion and also to study its interaction with the surrounding solid-bodies. These equations of motion for inviscid flow (Euler equations) and viscous flow (Navier-Stokes equations) are named the governing equations and these equations along with the flow and its mathematical description are defined in Chap. 2.

When dealing with viscous flows, solving the two types of fluid flows becomes imminent: laminar and turbulent. The solution to the Navier-Stokes equations is considerably direct for the laminar flows. However turbulent flows pose compelling difficulties. In order to model these turbulent flows Reynolds-averaged Navier-Stokes (RANS) equations are preferred. These equations are in close relation to the ones explained in Chap. 2. With the various turbulence models available to formulate the RANS equations, the one most suited for this thesis, the Spalart-Allmaras one equation model (SA-neg model) is touched upon in Chap. 3.

With the governing equations, the solution principles are necessary to proceed with the computations. The problems involving the computations of Euler and Navier-Stokes equations are usually dealt with the concept of the method of lines, wherein discretization is separated in both space and time. The fundamental concept of discretization along with the method of lines, followed by the need for an efficient solution for the equation that is met by introducing acceleration techniques is all explained in Chap. 4.

The experimental setup of five different test cases, with their configurations involving geometry and boundary conditions, flow conditions and computational mesh is presented in detail in Chap. 5. The computed results of the test cases are described under the sections of Chap. 6. A brief discussion about the extended cases that can be addressed through the work of this thesis and the summary is given in Chap. 7.

A brief introduction about the test cases is attributed to in Sec. 1.1.

1.1 Motivation

The purpose of this thesis is to

- perform a systematic mesh-refinement study for the existing RANS turbulent models to obtain accurate results, and
- to verify the correct implementation of the models.

Five test cases namely 2D Finite Flat Plate, 2D NACA 0012 Airfoil, 3D Modified Bump, 3D Hemisphere Cylinder and 3D ONERA M6 Wing are taken from the **Turbulence Modeling Resource** (TMR) website [1] for the experimental setup. The aim here is to provide for the "*verification*" [6] of these test cases. The TMR website has a compilation of simple test cases along with grids, that can be generated with the help of a Fortran code available at the website of the individual test cases. Few sample results such as the grid convergence studies from previously-verified codes are available for some turbulence models.

Through the outcome of this thesis for the turbulence model, comparison can be held against the predictions from the validation database. The main focus is to convene the fundamental phenomena for the fluid flows for the simple test cases by the turbulence model that is considered and thereby provide an appropriate basis for comparison that is reliable which further serves as a commencement for more intensive validation for flows of particular interest can be performed [7].

Chapter 2

Governing Equations

The term *fluid mechanics* in general deals with the analysis of the inter-molecular interactive motion for a wide range of distinctive particles. In most of the cases, the fluid flow is said to be in *continuum* as the density is assumed to be relatively high. Such a presumption means that even the smallest considered volume element can be defined with mean velocity and mean kinetic energy. By doing so, certain crucial properties such as velocity, density, pressure, etc., along with other properties can be determined.

The governing equations of fluid dynamics are derived based on conservation laws, which define the flow behavior of the fluid. By applying the macroscopic properties (continuum), substantial derivatives alongside the time and spatial coordinates to the governing equations, one can derive the basic equations that govern the fluid flow. Reynolds Transport theorem is applied to the continuity equation leading to the formulation of conservation of mass. Furthermore by applying basic laws, one can deduce the other famous conservation laws of momentum and energy.

Navier Stokes equations form the fundamental basis for all fluid flow problems. These equations describe a system of nonlinear conservation laws that are formed from the laws of mass, momentum, and energy. They can be written in terms of 5 integral or differential equations of order two. The following sections depict the structure of Navier-Stokes equations and its components.

The derivations and equations of CFD in general used in this thesis are an extract from the lecture notes of [4] and [5]. To provide concise content, only relevant formulas are illustrated.

2.1 Integral form of Navier-Stokes equation

The effects of flow is considered to be bounded in a domain $D \subset \mathbb{R}^m, m = 2,3$ which is an open (connected) set and within the interval range $[0,T) \subset \mathbb{R}, T{>}0$. The general conservative form of the equations are given as:

$$0 \;=\; \frac{d}{dt} V_D(W)(t) + R_{\partial D}(W)(t), \qquad t \in [0,T), \tag{2.1}$$

where V_D and $R_{\partial D}$ are integral operators defined as:

$$\begin{aligned} V_D(W)(t) &:= \int_D W(x,t)dx \\ R_{c,\partial D}(W)(t) &:= \int_{\partial D} \langle f_c(W(y,t)), n(y)\rangle \; ds(y), \\ R_{v,\partial D}(W)(t) &:= \int_{\partial D} \langle f_v(W(y,t)), n(y)\rangle \; ds(y), \\ R_{\partial D} &:= R_{c,\partial D} - R_{v,\partial D} \end{aligned} \tag{2.2}$$

and $W : D \times [0,T) \rightarrow \mathbb{R}^{m+2}$,

$$W(x,t) \coloneqq (\rho(x,t), \rho(x,t)u(x,t), \rho(x,t)E(x,t))^T, \tag{2.3}$$

where W denotes the vector on conservative variables, which facilitates the integral formulation and n is the unit normal projecting outward on ∂D. The terms $\langle f_c, n\rangle$ and $\langle f_v, n\rangle$ represent the convective and viscous fluxes respectively, that were formed from the Flux density tensor ($\bar{\bar{f}} = \bar{\bar{f}}_c - \bar{\bar{f}}_v$).

The quantities that are mentioned such as ρ, $u = (u_1, \ldots, u_m)^T$, E and

$$H \coloneqq E + p/\rho \tag{2.4}$$

denote the density, velocity, specific total energy and enthalpy of the fluid; μ is the coefficient of dynamic viscosity, τ is the viscous shear stress tensor and θ represents the heat flux in relation with energy.

From Eqn. 2.1 and 2.2 the following can be written:

$$f_c(W) = \begin{pmatrix} \rho u \\ \rho u_1 u + p e_1 \\ \vdots \\ \rho u_m u + p e_m \\ \rho H u \end{pmatrix}, \qquad f_v(W) = \begin{pmatrix} 0 \\ \tau_1(W) \\ \vdots \\ \tau_m(W) \\ \theta(W) \end{pmatrix} \tag{2.5}$$

The expression

$$\langle x, y\rangle \coloneqq \sum_{j=1}^{m} x_j y_j, \quad x, y \in \mathbb{R}^m$$

represents the standard l^2 product in $\mathbb{R}^m$ that requires a component-wise understanding for each of the equations in Eq. 2.1. The symbols $e_1, \ldots, e_m$ are used to represent the orthonormal basis of $\mathbb{R}^m$, i.e.,

$$e_1 = \begin{pmatrix} 1 \\ 0 \\ 0 \\ \vdots \\ 0 \end{pmatrix}, \; e_2 = \begin{pmatrix} 0 \\ 1 \\ 0 \\ \vdots \\ 0 \end{pmatrix}, \ldots, e_m = \begin{pmatrix} 0 \\ 0 \\ \vdots \\ 0 \\ 1 \end{pmatrix} \tag{2.6}$$

The momentum of the flow in x_j direction is given as $\widehat{mom}_j \coloneqq \rho u_j$ which is the product of density and velocity. The equation of state

$$p(W(x,t)) \coloneqq (\gamma - 1)\rho(x,t) \left(E(x,t) - \frac{\|u(x,t)\|_2^2}{2} \right) \tag{2.7}$$

is used to describe the pressure p and the gas dependent ratio of specific heats γ that is 1.4 for air. Thereby the speed of sound a, Mach number (dimensionless) M and temperature T are given as

$$a \coloneqq \sqrt{\frac{\gamma p}{\rho}}, \; Ma \coloneqq \frac{\|u\|_2}{a}, \; T \coloneqq \frac{p}{\rho \Re}, \tag{2.8}$$

where $\Re$ denotes the universal gas constant.

From Eq. 2.4 and 2.7 the speed of sound can be phrased as follows

$$\begin{aligned} a^2 &= \frac{1}{\rho}\left[p + (\gamma-1)p\right] \\ &= \frac{1}{\rho}\left[(\gamma-1)\rho\left(E - \frac{\|u\|_2^2}{2}\right) + (\gamma-1)p\right] \\ &= (\gamma-1)\left(E + \frac{p}{\rho} - \frac{\|u\|_2^2}{2}\right) \\ &= (\gamma-1)\left(H - \frac{\|u\|_2^2}{2}\right). \end{aligned} \tag{2.9}$$

Finally, with all the variables that were illustrated in this section, the governing equations can be represented in three integral form as follows [5]:

Conservation of mass

$$\frac{d}{dt}\int_D \rho(x,t)dx + \int_{\partial D}\langle(\rho u)(x,t), n\rangle ds = 0 \tag{2.10}$$

Conservation of momentum

$$\frac{d}{dt}\int_D (\rho u)_i\,(x,t)dx + \int_{\partial D}\langle(\rho u_i)\,(x,t)u(x,t) + p(x,t)e_i, n\rangle\, ds - \int_{\partial D}\mu(x,t)\langle\tau_i(x,t), n\rangle\, ds = 0, \qquad i = 1,\ldots,m \tag{2.11}$$

Conservation of energy

$$\frac{d}{dt}\int_D (\rho E)(x,t)dx + \int_{\partial D}\langle\rho(x,t)H(x,t)u(x,t), n\rangle\, ds - \int_{\partial D}\mu(x,t)\langle\theta(x,t), n\rangle\, ds = 0 \tag{2.12}$$

The integral form of the governing equations (Ref. Eqn. 2.10, 2.11 and 2.12), as described in this section are then treated with *Gauss' Divergence theorem* to build the differential form of the governing equations which is described in detail in Sec. 2.2.

2.2 Governing Equations in differential form

Gauss' divergence theorem [5] Considering that U is an open subset of $\mathbb{R}^m$ which is bounded and $\partial U \in C^1$ and also $n : \partial U \to \mathbb{R}^m$ describe the outer unit normal on ∂U. Then Gauss' divergence theorem can be written as

$$\int_U \mathrm{div}(F)\, dx = \int_{\partial U}\langle F, n\rangle\, ds \tag{2.13}$$

The differential form on Navier-Stokes equations is extracted from the integral equations by applying Gauss' divergence theorem. Through the permutation of differentiation and integration, the conservation laws can be formulated as [5]:

$$
\begin{aligned}
0 &= \int_D \frac{\partial \rho(x,t)}{\partial t}\, dx + \int_D \operatorname{div}\left((\rho u)(x,t)\right) dx, \\
0 &= \int_D \frac{\partial}{\partial t}(\rho u)_i(x,t)\, dx + \int_D \operatorname{div}\left((\rho u_i)(x,t) u(x,t)\right) dx \\
&\quad + \int_D \operatorname{div}(p(x,t) e_i)\, dx - \int_D \operatorname{div}(\mu(x,t)\tau_i(x,t)) dx \\
0 &= \int_D \frac{\partial}{\partial t}(\rho E)(x,t)\, dx + \int_D \operatorname{div}\left(\rho(x,t) H(x,t) u(x,t)\right) dx \\
&\quad - \int_D \operatorname{div}(\mu(x,t)\theta(x,t)) dx.
\end{aligned}
\tag{2.14}
$$

These equations are assumed to be valid for any open subset D that is bounded and so the differential form of the equations can be finally written as [5]:

$$
\begin{aligned}
0 &= \frac{\partial}{\partial t}\rho(x,t) + \operatorname{div}\left(\rho u\right)(x,t) \\
&= \frac{\partial \rho}{\partial t} + \sum_{j=1}^{3} \frac{\partial(\rho u)}{\partial x_j} \\
0 &= \frac{\partial(\rho u_i)}{\partial t} + \left[\sum_{j=1}^{3} \frac{\partial(\rho u_i u_j)}{\partial x_j} + \delta_{ij}\frac{\partial p}{\partial x_j}\right] \\
&\quad - \sum_{j=1}^{3} \frac{\partial}{\partial x_j}\left(\mu\left(\frac{\partial u_i}{\partial x_j} + \frac{\partial u_j}{\partial x_i}\right) - \frac{2}{3}\delta_{ij}\operatorname{div}(u)\right), \quad i = 1,2,3, \\
0 &= \frac{\partial(\rho E)}{\partial t} + \operatorname{div}\left(\rho H u\right) - \operatorname{div}(\mu\theta) \\
&= \frac{\partial \rho E}{\partial t} + \sum_{j=1}^{3} \frac{\partial(\rho H u)}{\partial x_j} - \sum_{j=1}^{3} \frac{\partial}{\partial x_j}\left(\sum_{k=1}^{3} \tau_{kj} u_j + \kappa \frac{\partial T}{\partial x_j}\right).
\end{aligned}
\tag{2.15}
$$

Sec. 2.3 marks the system of Navier-Stokes equations that are developed using the principles explained in Sec. 2.1 and Sec. 2.2.

2.3 Navier-Stokes equations using fluxes

The various system of conservation laws is characterized by one system of equations so that the different terms involved can be investigated. Two flux vectors are introduced. The convective flux vectors $\langle f_c, n\rangle$ as the name suggests, denote the convective transport of the particles in the fluid flow. The viscous flux vectors $\langle f_v, n\rangle$ consist of both the viscous stresses and the heat diffusion of the flow. Combining all the quantities that are mentioned, the Navier stokes equation can be written in the general format as

$$
\frac{d}{dt}\int_D W(x,t)dx + \int_{\partial D} \langle f_c(W(y,t)), n(y)\rangle\, ds(y) - \int_{\partial D} \langle f_v(W(y,t)), n(y)\rangle\, ds(y) = 0 \tag{2.16}
$$

In three dimensions, the Navier-Stokes equations typically express a system of five nonlinear equations corresponding to the five conservative variable ρ, ρu_1, ρu_2, ρu_3, and ρE. But there exist seven unknown field variables, namely ρ, u_1, u_2, u_3, E, p and T. Hence there arises the need for two additional equations with the condition that these equations should hold thermodynamic relations between the given state variables. Inclusive of these variables, is the demand to define

the viscosity coefficient μ and thermal conductivity coefficient k as a function of the state variables, to devise the entire system of equations. Further explanations regarding the unknown variables are dealt with detail in Chap. 3.

Chapter 3

Turbulence Modeling

Obtaining the solution of the governing equations for laminar flows, do not pose any significant complexity. However, when dealing with the turbulent flows, simulation becomes problematic because of the inherent source terms. A numerical simulation that solves the Navier-Stokes equation directly, without any turbulence models is called *Direct Numerical Simulation* (DNS), which mainly deals with flows at low Reynolds number. DNS serves as a benchmark model for new models to be developed. The next model that provides an approximation of the first level is the *Large-Eddy Simulation* (LES) model. LES model incorporates the DNS model to attain a resolution that affects both the time and the spatial components of the flow field, thereby making it expensive for computation.

Reynolds-Averaged Navier-Stokes equations (RANS) serves as the approximation of the next level wherein the Spatio-temporal flow variables are decomposed into mean and fluctuating parts. For incompressible flows, the velocity components are treated by *Favre decomposition*. By the Bousinessq's assumption the Reynolds stress tensor that is obtained, is considered to be proportional to the Shear stress tensor. When the decomposed variables are averaged by introducing them into the Navier-Stokes equations, there arise two additional terms with the existing mean variables. The viscous stress tensor is extended by the *Reynolds-stress tensor* τ_{ij} and this contains the *eddy viscosity*. The second additional term would be the *diffusive (turbulent) heat flux* that is extended from the energy equation. The basic flow of the equations is described in Sec. 3.1.

The unknown eddy viscosity (μ_t) component has to be modeled employing an equation. This modeling can be done by either of the following methods:

a) Algebraic models, such as Baldwin-Barth, Baldwin-Lomax,

b) One equation models, such as the Spalart-Allmaras model,

c) Two equation $k\omega$ or $k\varepsilon$-models such as Wilcox $k\omega$-model, Shear Stress Transport (SST) model.

To determine μ_t further integral or differential equations need to be solved, then the following holds

$$\mu_{eff} = \mu_l + \mu_t, \tag{3.1}$$

where μ_{eff} is the effective viscosity and μ_l is the laminar viscosity.

3.1 Basic equations of Turbulence

The governing equations are now combined with the turbulence modeling variables and these variables are explained in the following section.

The *Strain rate tensor* $\mathcal{S} = \mathcal{S}(u) = \mathcal{S}(u(x,t))$ is obtained from the symmetric portion of the computed total derivative of u (flow velocity).

$$\mathcal{S}(u) \coloneqq \frac{1}{2}\left(\frac{du}{dx} + \left(\frac{du}{dx}\right)^T\right). \tag{3.2}$$

The *trace free shear stress tensor* $\bar{\mathcal{S}}$ is gathered from Eq. 3.2 and is given as:

$$\bar{\mathcal{S}} \coloneqq \mathcal{S}(u) - \frac{1}{3}\operatorname{div}(u)\, Id. \tag{3.3}$$

Besides, the *vorticity* Ω term is defined by the skew-symmetric portion of the computed total derivative of u,

$$\Omega(u) \coloneqq \frac{1}{2}\left(\frac{du}{dx} - \left(\frac{du}{dx}\right)^T\right). \tag{3.4}$$

Admitting an *effective viscosity* μ_{eff} by virtue of Stoke's hypothesis, that the condition $\lambda = -2/3\mu_{eff}$ is satisfied by the bulk viscosity, the resulting *viscous stress tensor* $\tau = \tau(W) = \tau(W(x,t))$ is given by:

$$\tau(W) \coloneqq \mu_{eff}\mathcal{S} + \lambda \operatorname{div}(u) Id = 2\mu_{eff}\left(\mathcal{S} - \frac{1}{3}\operatorname{div}(u) Id\right) = 2\mu_{eff}\bar{\mathcal{S}}. \tag{3.5}$$

As a deduction, the τ that is obtained is symmetric and can certainly be indicated as:

$$\tau_{ii}(W) = 2\mu_{eff}\frac{\partial u_i}{\partial x_i} + \lambda \operatorname{div}(u) = \frac{2}{3}\mu_{eff}\left(2\frac{\partial u_i}{\partial x_i} - \sum_{j=1, j\neq i}^{m}\frac{\partial u_j}{\partial x_j}\right), \quad i = 1, \ldots, m,$$

$$\tau_{ij}(W) = 2\mu_{eff}\mathcal{S}_{ij} = \mu_{eff}\left(\frac{\partial u_i}{\partial x_i} + \frac{\partial u_i}{\partial x_i}\right), \qquad \tau_{ji} = \tau_{ij}, \quad 1 \leq i < j \leq m.$$

For the energy equation, the missing viscous flux term is computed as

$$\theta(W) = \tau(W)u + q(W), \qquad q(W) = \kappa \text{grad } T. \tag{3.6}$$

The component-wise expression for the viscous flux term from Eq. 3.6 is

$$\theta_j(W) \coloneqq \left(\sum_{k=1}^{m}\tau_{jk}(W)u_k\right) + \kappa_{eff}\frac{\partial T}{\partial x_j}, \qquad j = 1, \ldots, m. \tag{3.7}$$

From the above equation the terms effective viscosity (μ_{eff}) and effective conductivity (κ_{eff}) can be evaluated as

$$\mu_{eff} \coloneqq \mu_l + \mu_t, \quad \kappa_{eff} \coloneqq \kappa_l + \kappa_t, \tag{3.8}$$

where the laminar viscosity μ_l is computed using **Sutherland's law** as

$$\mu_l(W) \coloneqq \mu_{l,\infty}\left(\frac{T}{T_\infty}\right)^{3/2}\frac{T_\infty + \bar{T}}{T + \bar{T}}, \qquad \mu_{l,\infty} \coloneqq \frac{\rho_\infty u_\infty L}{Re}, \tag{3.9}$$

and the laminar conductivity (κ_l) is given as

$$\kappa_l(W) \coloneqq \frac{c_p\mu_l(W)}{Pr_l} \quad \text{and} \quad c_p \coloneqq \Re\frac{\gamma}{\gamma - 1}, \tag{3.10}$$

at which point $\rho_\infty > 0$ and $u_\infty > 0$ are the terms denoted as reference density and reference velocity throughout the test cases. Similarly, $L > 0$ is the constant reference length scale and $Re > 0$ is the predefined Reynolds number. Also, $\bar{T}$ that stands for *Sutherland's constant* is:

$$\bar{T} \coloneqq 110.4K, \tag{3.11}$$

$\Re$ is the universal gas constant and the laminar Prandtl number Pr_l is given as $Pr_l \coloneqq 0.72$. Deriving out of Pr_l is the definition for laminar kinematic viscosity as:

$$\nu_l(W) \coloneqq \frac{\mu_l(W)}{\rho}. \tag{3.12}$$

The main unknown additional terms that arise due to turbulence are given by Eq. 3.8 namely eddy viscosity μ_t an turbulent thermal conductivity κ_t. When the eddy viscosity μ_t is specified the turbulent thermal conductivity κ_t can be represented by the relation:

$$\kappa_t \coloneqq c_p \frac{\mu_t}{Pr_t}, \quad Pr_t \coloneqq 0.92. \tag{3.13}$$

The aim of introducing Pr_t is to reduce the number of unknowns to one.

Through turbulence modeling, the eddy viscosity is defined as a function in order to simulate the turbulent flows. As a general idea, μ_t is evaluated from the additional unknowns, as a solution to those additional equations, i.e., the turbulence flow equations. Hence the following is theorized:

$$\mu_t(W_t, W)(x,t) \geq 0 \quad \text{for all} \quad (x,t) \in D \text{ x } [0,T). \tag{3.14}$$

The RANS equation Eq. 2.1 is formulated so as to define the function μ_t. This function is assumed to be known a priori so that it can be inserted into the equations Eq. 2.1. With respect to the laminar viscosity, the turbulent kinematic viscosity is designated as

$$\nu_t(W_t, W)(x,t) \coloneqq \frac{\mu_t(W_t, W)(x,t)}{\rho}. \tag{3.15}$$

When $\mu_t \equiv \kappa_t \equiv 0$ then Eq. 2.1 is called *(laminar) Navier-Stokes equations*. Otherwise Eq. 2.1 is called the *Reynolds-averaged Navier-Stokes equation*.

3.2 Spalart-Allmaras One-equation Model

To approximate the Reynolds stresses in the RANS equations, the first order closures provide the convenient way possible. Based on Boussinesq assumptions, a turbulence model that exists should be able to evaluate the eddy viscosity μ_t. One such first-order closure model that can be applied to both structured and unstructured grids to determine μ_t by an additional scalar differential equation is the *Spalart-Allmaras* (SA) model. For an accurate prediction of turbulent flows consisting of adverse pressure gradients, this model can be used. The laminar to turbulent flow transition is reasonably smooth with the SA model. Since the main focus of the thesis is on grid convergence study, the SA model is highly preferable.

The SA model is illustrated through the following equations [8]:

$$V_D(Q_{SA}(\tilde{\nu}, W))(t) = \frac{d}{dt} V_D(\tilde{\nu})(t) + R_{\partial D, SA}(\tilde{\nu}, W)(t), \tag{3.16}$$

where

$$\begin{aligned} R_{c,\partial D,SA}(\tilde{\nu},W)(t) &:= \int_{\partial D} \langle f_{c,SA}(\tilde{\nu}(y,t),W(y,t)),n(y)\rangle \, ds(y), \\ R_{v,\partial D,SA}(\tilde{\nu},W)(t) &:= \int_{\partial D} \langle f_{v,SA}(\tilde{\nu}(y,t),W(y,t)),n(y)\rangle \, ds(y), \\ R_{\partial D,SA} &:= R_{c,\partial D,SA} \; - \; R_{v,\partial D,SA}. \end{aligned}$$

$$\begin{aligned} f_{c,SA}(\tilde{\nu},W) &:= \tilde{\nu} u, \\ f_{v,SA}(\tilde{\nu},W) &:= \frac{1}{\sigma} \begin{cases} (\nu_l + \tilde{\nu}) \, \mathrm{grad}(\tilde{\nu}), & \tilde{\nu} \geq 0, \\ (\nu_l + f_n \tilde{\nu}) \, \mathrm{grad}(\tilde{\nu}), & \tilde{\nu} < 0, \end{cases} \\ f_n(\tilde{\nu},W)(x,t) &:= \frac{c_{n1} + \left(\mathcal{X}(x,t)\right)^3}{c_{n1} - \left(\mathcal{X}(x,t)\right)^3}, \quad c_{n1} := 16, \\ \mathcal{X}(\tilde{\nu},W) &:= \frac{\tilde{\nu}}{\nu_1(W)}. \end{aligned} \tag{3.17}$$

There exists a transported variable $\tilde{\nu}$ that is necessary to estimate μ_t that is:

$$\mu_t(\tilde{\nu},W) := \begin{cases} \rho \tilde{\nu} f_{v1}, & \tilde{\nu} \geq 0, \\ 0, & \tilde{\nu} < 0, \end{cases} \qquad f_{v1}(\tilde{\nu},W) := \frac{\mathcal{X}^3(\tilde{\nu},W)}{\mathcal{X}^3(\tilde{\nu},W) + c_{v1}^3}. \tag{3.18}$$

The left-hand side of Eq. 3.16 indicates the eddy-viscosity production Pr_{SA}, diffusion in the non-conservative form $Di_{SA}$and turbulence destruction near the wall De_{SA}. So, the source term in general is given as:

$$Q_{SA} := Pr_{SA} \; - \; De_{SA} \; + \; Di_{SA}, \tag{3.19}$$

where

$$\begin{aligned} Pr_{SA} &:= \begin{cases} c_{b1}(1-f_{t2})\tilde{S}\tilde{\nu}, & \tilde{\nu} \geq 0 \\ c_{b1}(1-c_{t3})S\tilde{\nu}, & \tilde{\nu} < 0 \end{cases}, \qquad f_{t2} := c_{t3} \exp\left(c_{t4}\mathcal{X}^2\right), \\ De_{SA} &:= \begin{cases} \left(c_{w1} f_w - \frac{c_{b1}}{\kappa^2} f_{t2}\right) \left(\frac{\tilde{\nu}}{d}\right)^2, & \tilde{\nu} \geq 0 \\ -c_{w1} \left(\frac{\tilde{\nu}}{d}\right)^2, & \tilde{\nu} < 0 \end{cases}, \qquad f_w := g \left(\frac{1+c_{w3}^6}{g^6 + c_{w3}^6}\right)^{1/6}, \\ Di_{SA} &:= \frac{c_{b2}}{\sigma} \left\| \mathrm{grad} \, \tilde{\nu} \right\|_2^2. \end{aligned} \tag{3.20}$$

Here S denotes the magnitude of mean rotation rate. Detailed expansion of each of the components are given below:

$$\begin{aligned} S &:= \sqrt{2\Omega \otimes \Omega}, \quad \bar{S} := \frac{\tilde{\nu}(x,t)}{\kappa^2 d^2(x)} f_{v2}(x,t), \\ \tilde{S} &:= \begin{cases} S + \bar{S}, & \bar{S} \geq -c_{v2} S \\ S + \frac{S\left(c_{v2}^2 S + c_{v3} \bar{S}\right)}{(c_{v3} - 2c_{v2})S - \bar{S}}, & \bar{S} < -c_{v2} S \end{cases}, \\ g &:= r + c_{w2} r \left(r^5 - 1\right), \quad r := \left\{ \min \frac{\tilde{\nu}}{\kappa^2 d^2 \tilde{S}}, 10 \right\}, \\ f_{v2} &:= 1 \; - \; \frac{\mathcal{X}}{1 + \mathcal{X} f_{v1}}. \end{aligned} \tag{3.21}$$

where f_w, g and r are specified to be the terms that regulate the destruction of eddy viscosity and $d(x)$ is the distance to the wall. Moreover, certain functions that are being used for the transition of the laminar-turbulent flow is given by f_{t2}.

The different constants that are used throughout the modeling are assumed as:

$$\begin{aligned} c_{b1} &:= 0.1355, \quad c_{b2} := 0.622, \quad \sigma := \frac{2}{3}, \quad \kappa := 0.41, \\ c_{w1} &:= \frac{c_{b1}}{\kappa^2} + \frac{1 + c_{b2}}{\sigma}, \quad c_{w2} := 0.3, \quad c_{w3} := 2, \\ c_{t3} &:= 1.2, \quad c_{t4} := 0.5, \\ c_{v1} &:= 7.1, \quad c_{v2} := 0.7, \quad c_{v3} := 0.9. \end{aligned} \tag{3.22}$$

The turbulence model that is preferred for this thesis is explained in the next section.

3.2.1 SA-neg model

The need for *Negative Spalart-Allmaras One-Equation model* (SA-neg) is to deal with the existing problems regarding under-resolved grids and the transient states in the discrete state of equations, where the solution of the turbulent flow can be negative. Following are the properties with which the SA-neg model differs from SA model [9]:

- for $\tilde{\nu} \geq 0$, the values are consistent with the SA model,
- when $\tilde{\nu}$ approaches negative value, there is zero turbulent eddy viscosity,
- the functions of the pde are C^1 continuous corresponding to $\tilde{\nu}$ at $\tilde{\nu} = 0$,
- SA-neg model is stable in terms of energy,
- with non-negative boundary conditions the analytic solution remains non-negative.

The expanded form of the SA-neg model can be written as:

$$\begin{aligned} \frac{\partial \tilde{\nu}}{\partial t} + u_j \frac{\partial \tilde{\nu}}{\partial x_j} &= c_{b1}\left(1 - c_{t3}\right)\Omega\tilde{\nu} + c_{w1}\left(\frac{\tilde{\nu}}{d}\right)^2 \\ &\quad + \frac{1}{\sigma}\left[\frac{\partial}{\partial x_j}\left(\left(\nu + \tilde{\nu} f_n\right)\frac{\partial \tilde{\nu}}{\partial x_j}\right) + c_{b2}\frac{\partial \tilde{\nu}}{\partial x_i}^2\right], \end{aligned} \tag{3.23}$$

with

$$f_n(\tilde{\nu}, W)(x,t) := \frac{c_{n1} + \left(\mathcal{X}(x,t)\right)^3}{c_{n1} - \left(\mathcal{X}(x,t)\right)^3}, \quad c_{n1} := 16.$$

It is to be noted that the destruction term in the source $c_{w1}\left(\frac{\tilde{\nu}}{d}\right)^2$ has a positive sign contrary to that of the SA model (Ref. Eq. 3.20).

The SA-neg model is modified to be applied also for higher-order methods. By doing so the requirement of further artificial dissipation or limiting function is deemed inessential. For coarser grids, negative turbulent eddy viscosity is expected near the boundary and the wake regions. However, with mesh-refinement, these negative characteristics are likely to disappear in both the physical and magnitude limit of these regions.

With the Navier-Stokes equations that are gained from Chap. 2 along with the turbulence model that is discussed in this chapter, the whole system of equations is now solved for the flow variables. The discretization techniques that can be applied and their function are discussed in Chap. 4.

Chapter 4

Discretization Strategy

The following section is to discuss the discretization techniques applied to the Navier-Stokes equation with the Boussinesq eddy viscosity assumption, focusing on the RANS equations. The equations used in this thesis, in general, are an extract from the notes of [4] and [5].

The flow that is to be evaluated is defined in a definite space called the *physical space* which in turn comprises of extensive geometrical elements called *grid cells*. This computation is termed as *grid generation*. The grids should be essentially *smooth*, meaning that there should be no sudden changes in the grid cells' volume or in particular in the stretching ratio, otherwise there is the possibility of numerical errors to show significant behavior in the solution [10].

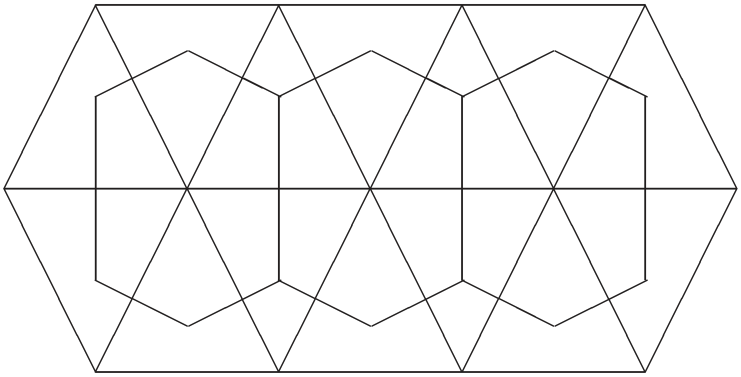

Figure 4.1: Example of a triangular primary grid and its dual grid [3].

The discretization strategy involves the finite volume method with node centered scheme on meshes. The grid that is used is often called as *dual mesh*, which is developed during the preprocessing of a primary grid. During the generation of the mesh, control volumes are established that contain the unknowns at their vertices. Fig. 4.1 shows the formation of the computational mesh from a triangular grid.

Discretization doesn't involve differentiating between the primary and dual grid, but rather on the mesh generation tool which can be different from the existing computational mesh.

In the following sections, different solution methodologies for the approximation of RANS equations, in both the time and spatial coordinates followed by the application of turbulence modeling with the boundary discretization is addressed.

4.1 Spatial Discretization

The spatial discretization of the Navier Stokes equation is generally the discretization involving the numerical approximation of the fluxes (convective and viscous fluxes) along with the source term mentioned in Sec. 3.2. For this purpose, methods such as finite volume, finite element, and finite difference are available. The two types of grids: *Structured* and *Unstructured* grids form the basis of which the computational mesh is setup.

- *Structured* grids - the indices of the grids *i,j,* and *k* are arranged in an orderly manner such that the connectivity between them is not only easy but also quick, so much so that by simple mathematical addition or subtraction of an integer from the existing index, leads to establish the connection with the neighboring grids e.g., $(j+3)$, $(i-5)$ etc. These grids exist as a quadrilateral in $2D$ and hexahedral in $3D$. To conserve memory space and also for high resolution and better convergence, structured grids are put into practice.
- *Unstructured* grids - disordered connectivity that calls for a distinct correlation between adjacent grids, thereby leading to more memory consumption. These can ideally exist as triangles in $2D$ and tetrahedral in $3D$. These meshes further lead to the formation of *hybrid* meshes. Unstructured meshes can also exist as mixed elements that are a combination of both structured and unstructured meshes wherein triangles and quadrilaterals can exist together.

For this thesis, the finite volume method of discretization on structured and unstructured meshes based on node centered scheme is considered. The general functional procedure of this method is touched upon in the following sections, Sec. 4.1.1 and 4.1.2.

Some common definitions are required for the discretization throughout the thesis. They are as follows [3]:

Definition 4.1.1. *Consider $D \subset \mathbb{R}^m$ to be a bounded domain. Also assume that there are a finite set of open domains $\{D_i\}_{i=1,\dots,N_{elem}}$, $D_i \subset \mathbb{R}^m$, $D_i \neq \emptyset$, covering D i.e.,*

$$D_i \subset D, \quad \bar{D} = \bigcup_{i=1}^{N_{elem}} \bar{D}_i, \quad D_i \cap D_j = \emptyset, \ i \neq j.$$

Then the set

$$M := \{D_i : 1, \dots, N_{elem}\}$$

is then said to be a mesh or a grid or a decomposition covering D.

Definition 4.1.2. *For this thesis a feasible decomposition of M of $D \subset \mathbb{R}^m$ is called a triangulation or finite volume mesh.*

Definition 4.1.3. *With the assumption that $D \subset \mathbb{R}^m$ is a bounded domain,*

a) the volume of the domain D is given by

$$\mathrm{vol}(D) := \int_D 1 \, dx.$$

b) The point $x \in \mathbb{R}^m$,

$$x_i := \frac{1}{\mathrm{vol}(D)} \int_D y_i \, dy, \quad i = 1, \dots, m,$$

is termed as the barycenter of domain D.

Definition 4.1.4. *Consider M is a triangulation of D, and $D_i \in M$,*

a) $\mathcal{N}(i)$ is used to represent the neighbors of vertex i, and to denote the number of neighbors or the degree of i, the notation $\#\mathcal{N}(i)$ is used.

b) The barycenter of D_i is given by p_i.

c) Assume $e_{ij} \in E(M)$ so that the euclidean distance of the barycenters p_i of D_i and p_j of D_j is given by

$$\operatorname{dist}\left(e_{ij}\right) := \left\| p_i - p_j \right\|_2 .$$

4.1.1 Finite Volume Method

The integral form of the Navier-Stokes equation acquired directly from the conservation laws are taken into account in the finite volume method (FVM). The dependent values are stored at the nodes of the cell, thus ensuring that the conservative quantities are balanced. In this method, the computational domain is divided into numerous finite-sized sub-domains (control volume) that are represented as a finite number of grid points (nodal points). Then computation is done by applying the integral form of the pde over each of the subdomains. At the grid points, the results are represented as algebraic quantities (fluxes of conservative variables).

FVM is suited for both Structured and Unstructured grids making it flexible, thereby applicable to complex geometries. Since the spatial discretization is over the entire domain, transformation of the physical domain to the computational domain and vice-versa is made possible.

An additional necessity for FVM is mentioned in Sec. 4.1.4.

4.1.2 Node-centered scheme

Node-centered finite volume discretization methods find applications for turbulent simulations that are highly complex and are nominally second-order accurate. A *median-dual partition* [11] helps in constructing the control volumes i.e., the midpoints of the surrounding faces of the primary grid cells are connected to its center. This results in a computational domain that has non-overlapping control volumes that act as dual to the primary mesh.

Proceeding further, with the general viewpoint of spatial discretization methodologies from the previous sections, the Sec. 4.1.3 focuses more on the approximation of the convective fluxes.

4.1.3 Discretization of convective fluxes

The approximation of the convective flux is done during this discretization. From the finite volume method scheme, the following are the main preferences for the discretization of convective flux [10]

- central scheme,
- flux-vector splitting,
- flux-difference splitting,
- total variation diminishing (TVD) and
- fluctuation-splitting.

Central scheme

The central scheme depends exclusively on central difference formulae (central averaging). The convention is to average the conservative variables (given in Eqn. 2.3), at the cell wall, wherein information is collected from the left and right side, by which the flux can be assessed at the cell face of the control volume. The central scheme is capable of performing high-frequency damping to achieve desired convergence. The decoupling of the solution (odd-even point) seems problematic for this scheme to discern, for both the linear and non-linear problems. Therefore, additional terms called *artificial viscosity* have to be added to bring about the balance of the solution by removing oscillations in the vicinity of shocks [12].

For structured grids, the central scheme makes use of 2nd- and 4th differences (Ref. Eq. 4.2). The convective flux Jacobian scales these differences by its maximum eigenvalue. For structured grids, the undivided Laplacian is used along with the biharmonic operator.

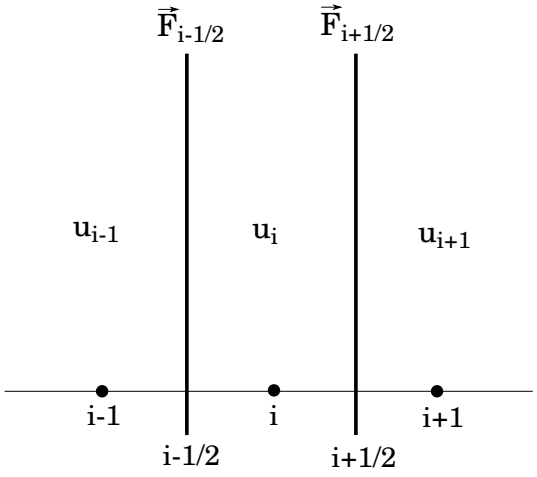

Figure 4.2: Central difference scheme notations [4].

$$\begin{aligned} \text{Forwards difference}: \ \nabla u_i &= u_{i+1} - u_i \\ \text{Backwards difference}: \ \Delta u_i &= u_i - u_{i-1} \end{aligned} \tag{4.1}$$

$$\begin{aligned} 2nd\ difference: \quad \nabla\Delta u_i &= (u_{i+1} - u_i) - (u_i - u_{i-1}) \\ &= u_{i+1} - 2u_i + u_{i-1} \\ &\approx \Delta x^2 (u_{xx}) \\ 4th\ difference: \nabla\Delta\nabla\Delta u_i &= u_{i+2} - 4u_{i+1} + 6u_i - 4u_{i-1} + u_{i-2} \\ &\approx \Delta x^4 (u_{xxxx}) \end{aligned} \tag{4.2}$$

The central scheme with 4th differences is given by Eq. 4.3, where the dissipation is of order 2 (high-frequency damping) [13].

$$\frac{\vec{W}_i^{n+1} - \vec{W}_i^n}{\Delta t} + \frac{\vec{F}_{i+1} - \vec{F}_{i-1}}{2\Delta x} = \underbrace{-k^{(4)} \frac{1}{\Delta x} \left[\nabla(|u| + c)_{i-\frac{1}{2}} \Delta\nabla\Delta\vec{W}_i\right]}_{\text{Dissipation} \approx \Delta x^3} \tag{4.3}$$

Matrix valued artificial viscosity scheme

In the case of meshes that have high aspect ratios, the scaling factor can give rise to larger numerical dissipation. By reducing the numerical dissipation, better accuracy can be achieved, and for this end, the above-mentioned scheme is manipulated to work like an upwind scheme. The improvement of the scheme can be done by manipulating these scaling factors and this process is done by the *matrix dissipation scheme* [14].

Consider Eulers equation that can be obtained from Navier Stokes equation (Ref. Eq. 2.16 by removing the viscous term. The resulting equation is as follows:

$$\frac{d}{dt}\int_D W(x,t)dx + \int_{\partial D} \langle f_c(W(y,t)), n(y)\rangle \, ds(y) = 0 \tag{4.4}$$

For discretization purpose for the central matrix-dissipation scheme, Eq. 4.4 can be written as:

$$\frac{\vec{W}_i^{n+1} - \vec{W}_i^n}{\Delta t} + \frac{\vec{F}_{i+\frac{1}{2}} - \vec{F}_{i-\frac{1}{2}}}{\Delta x} = 0 \tag{4.5}$$

$$\frac{\vec{W}_i^{n+1} - \vec{W}_i^n}{\Delta t} + \left(\frac{\frac{1}{2}\left(\vec{F}_{i+1} + \vec{F}_i\right)}{\Delta x} - \frac{\frac{1}{2}|\bar{\bar{A}}|_{i+\frac{1}{2}}\left(\vec{W}_{i+1} - \vec{W}_i\right)}{\Delta x} \right) - \left(\frac{\frac{1}{2}\left(\vec{F}_i + \vec{F}_{i-1}\right)}{\Delta x} - \frac{\frac{1}{2}|\bar{\bar{A}}|_{i-\frac{1}{2}}\left(\vec{W}_i - \vec{W}_{i-1}\right)}{\Delta x} \right) = 0, \tag{4.6}$$

where the scaling matrix $\bar{\bar{A}}_c = \frac{\partial \vec{F}}{\partial \vec{W}}$ is the convective flux Jacobian (matrix of conservative variables).

$$\frac{\vec{W}_i^{n+1} - \vec{W}_i^n}{\Delta t} + \frac{\vec{F}_{i+1} - \vec{F}_{i-1}}{2\Delta x} = \frac{1}{2\Delta x}\left[|\bar{\bar{A}}_{i+\frac{1}{2}}| \, \vec{W}_{i+1} - \left(|\bar{\bar{A}}_{i+\frac{1}{2}}| + |\bar{\bar{A}}_{i-\frac{1}{2}}| \right) \vec{W}_i + |\bar{\bar{A}}_{i-\frac{1}{2}}| \, \vec{W}_{i-1} \right] \tag{4.7}$$

For simplifications the scaling matrix is represented as $\bar{\bar{A}}$ and is defined as follows:

$$\bar{\bar{A}} = \bar{\bar{M}} \, \bar{\bar{\Lambda}} \, \bar{\bar{M}}^{-1}. \tag{4.8}$$

Here the modal matrix on the right-hand side $\bar{\bar{M}}$ and the modal matrix on the left-hand side, along with the diagonal matrix of the eigenvalues $\bar{\bar{\Lambda}}$ are considered to be the following if the corresponding eigenvectors of the Jacobian are non-linear.

$$|\bar{\bar{A}}| = \bar{\bar{M}} \, |\bar{\bar{\Lambda}}| \, \bar{\bar{M}}^{-1}. \tag{4.9}$$

According to the sign of the eigenvalues of $\bar{\bar{A}}$ upstream or downstream components in the flux vectors $\vec{F}_{i+\frac{1}{2}}$ are taken into account. Also, at the stagnation points, these eigenvalues are so limited in a way that they restrict the dissipation from approaching zero.

Upwind algorithm for improving dissipation model

The convective fluxes are evaluated from the information from the left and the right states at the face of the control volume by solving for the Riemann problem which was introduced by Godunov [15]. Also, approximate Riemann solvers were introduced to reduce the high computational effort that is needed to achieve the exact solution for the Riemann problem [4]. Roe's method is commonly preferred due to its increased accuracy in terms of boundary layers and for shocks to have a better resolution. The following subsection implies the method in detail.

Roe scheme

Riemann problem includes constructing a convective flux $\langle f_c, n\rangle = \langle f_c(W_i, W_j), n\rangle$ at the face e_{ij} in conjunction with the information given by the left state variables W_i and the right state variable W_j (Ref. Fig. 4.3). For the discretization of the convective flux the certain definitions and assumptions are required as follows [3]:

Definition 4.1.5. *Assume $D \subset \mathbb{R}^m$ to be a bounded domain and consider M to be a triangulation of D. Let two domains $D_{i\in M}$ and $D_j \in M$, $i \neq j$ satisfy*

$$\bar{D}_i \cap \bar{D}_i = \partial D_i \cap \partial D_j$$

then an edge (face) is defined in the mesh M that connects D_i with D_j by $e_{ij} := \partial D_i \cap \partial D_j$. This set of edges (faces) is denoted by

$$E(M) := \left\{ e_{ij} : i, j = 1, \dots N_{elem}, e_{ij} \neq \emptyset \right\}$$

Definition 4.1.6. *Considering M to be a triangulation of D, $D_i, D_j \in M$. A mapping $\mathcal{H} : C(D_i) \times C(D_j) \times \mathbb{R}^m \to L^1\left(\partial D_i \cap \partial D_j\right)$ is said to be a numerical flux function in condition that it holds for*

$$\begin{aligned} \mathcal{H}\left(W, W, n\right)|_{e_{ij}} &= \langle f_c(W), n\rangle \\ \mathcal{H}(U, W, n) &= -\mathcal{H}(W, U, -n). \end{aligned}$$

In the direction of n (Ref. Fig. 4.3), a numerical flux function $\mathcal{H}$ is defined that corresponds to the Roe scheme as follows:

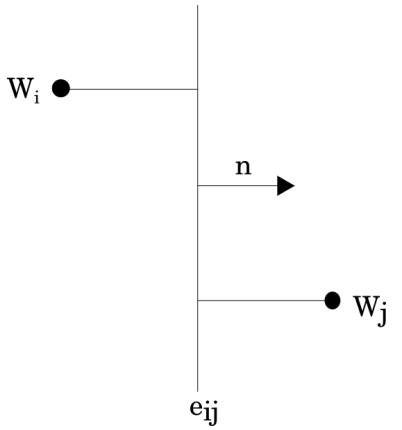

Figure 4.3: Riemann problem for the edge (face) [5].

$$\begin{aligned} \mathcal{H}^{1st,Roe}(W_i, W_j, n) := \frac{1}{2}\left[\langle f_c(W_i), n\rangle + \langle f_c(W_j), n\rangle\right] \\ - \frac{1}{2}|\mathbf{A}_{ij}^{Roe}|(W_j - W_i) \end{aligned} \tag{4.10}$$

$$\mathbf{A}_{ij}^{Roe} := \frac{\partial \langle f_c(W_{ij,Roe}), n\rangle}{\partial W}$$

Roe averaged variables indicate the approximate Riemann solver that is implemented on the structure of the dual mesh control-volume. At the face of the control volume, Roe scheme enforces the breakdown of the flux difference as a sum of wave contributions, all the while preserving the conservation laws. This decomposition is described as,

$$f_c(\vec{W}_i) \; - \; f_c(\vec{W}_j) \; = \; \bar{\bar{A}}_{ij,Roe}(\vec{W}_i \; - \; \vec{W}_j), \tag{4.11}$$

where $\bar{\bar{A}}_{ij,Roe}$ is the *Roe-matrix* and i and j indicate the left and the right states respectively.

$$\bar{\bar{A}}_{ij,Roe} \; = \; \frac{\partial \langle f_c(W_{ij,Roe}), n \rangle}{\partial W}, \tag{4.12}$$

which is equivalent to the convective flux Jacobian $\bar{\bar{A}}$ where Roe-averaged variables replace the conservative variables.

Roe-averaging of conservative variables

$$\begin{aligned} \rho_{ij,Roe} \; &\coloneqq \sqrt{\rho_i \rho_j}, \\ (u_{ij,Roe})_k \; &\coloneqq \frac{(u_i)_k \sqrt{\rho_i} \; + \; (u_j)_k \sqrt{\rho_j}}{\sqrt{\rho_i} + \sqrt{\rho_j}}, \quad k \; = \; 1, \cdots, m, \\ H_{ij,Roe} \; &\coloneqq \frac{H_i \sqrt{\rho_i} + H_j \sqrt{\rho_j}}{\sqrt{\rho_i} + \sqrt{\rho_j}}. \end{aligned} \tag{4.13}$$

The eigendecomposition similar to the matrix dissipation scheme is given by $\bar{\bar{A}}_{ij,Roe} \; = \; \bar{\bar{G}} \, \bar{\bar{\Lambda}} \, \bar{\bar{G}}^{-1}$ from which the following is computed.

$$f_c(\vec{W}_i) \; - \; f_c(\vec{W}_j) \; = \; G\Lambda \left(G^{-1} W_i \; - \; G^{-1} W_j \right) \; = \; \bar{\bar{G}} \, \bar{\bar{\Lambda}} \, (\bar{\bar{C}}_i - \bar{\bar{C}}_j), \tag{4.14}$$

where $\bar{\bar{C}}$ are the characteristic waves that represent wave amplitudes. The eigenvalues of $\bar{\bar{\Lambda}}$ are the associated wave speeds and the eigenvectors in general define the waves of the approximate Riemann problem.

4.1.4 Entropy condition

With the finite volume method, it is also the advantage to compute *weak solutions* of the general strong conservative differential equation fitting the problem. The rule to do so is known as the *entropy condition*. The eigenvalues that were obtained sometimes tend to go to zero, because there exists non-uniqueness of the weak solutions. Consequently, the resulting scheme exhibits the following irregularities [4]:

- dissipation in the scheme halts,
- instabilities that are unphysical (expansion shocks),
- possibility to violate the second law of thermodynamics (decrease in entropy).

Under these circumstances, to avoid this zero position, artificial changes in the eigenvalues are introduced. Subsequently, the *Rankine-Hugoniot* conditions hold over the discontinuity of the solution [4].

From Eq. 4.12 the following is obtained [5],

$$|A_{ij,Roe}| \; = \; \left| \frac{\partial \langle f_c(W_{ij,Roe}), n \rangle}{\partial W} \right|, \tag{4.15}$$

where the eigenpairs of $\frac{\partial \langle f_c(W_{ij,Roe}),n\rangle}{\partial W}$ are given as,

$$\left\{(V,g_1)\,,\ (V,g_2)\,,\ (V,g_3)\,,\ (V+a,g_4)\,,\ (V-a,g_5)\right\},$$

also $G \coloneqq (g_1,\ldots,g_5)$ and $G \coloneqq (q_1,\ldots,q_5)$

The entropy fix (subscript ef) of the Roe-averaged scheme is computed by replacing the absolute eigenvalues by [5]

$$|\Lambda|_{ef} \coloneqq \mathrm{diag}\left(|V|_{ef,1}\ ,|V|_{ef,1}\ ,|V|_{ef,1}\ ,|V+a|_{ef,2}\ ,|V-a|_{ef,3}\right), \tag{4.16}$$

where

$$\begin{aligned}
|V|_{ef,1} &\coloneqq |\lambda_i|_{ef,1} \coloneqq \max\left\{|V|\,,\delta_{ef}\left(|V|+a\right)\right\}, \qquad i = 1,2,3,\\
|V+a|_{ef,2} &\coloneqq |\lambda_4|_{ef,2} \coloneqq \max\left\{|V+a|\,,\delta_{ef}\left(|V|+a\right)\right\},\\
|V-a|_{ef,3} &\coloneqq |\lambda_5|_{ef,3} \coloneqq \max\left\{|V-a|\,,\delta_{ef}\left(|V|+a\right)\right\}.
\end{aligned}$$

This gives,

$$\left|A^{Roe}\right|_{ef} = \left(\sum_{j=1}^{3}\left|\lambda_j\right|_{ef,1} g_j q_j + |\lambda_4|_{ef,2}\, g_4 q_4 + |\lambda_5|_{ef,3}\, g_5 q_5\right). \tag{4.17}$$

The value of entropy fix is usually in the range $0 \le \lambda_{ef} \le 1$. For the experimental purpose here, $\lambda_{ef} = 0.2$ for the mean flow of the equations.

The discretization of viscous fluxes follows after the discretization of convective fluxes. The overall idea of the working of this discretization procedure is explained in Sec. 4.1.5.

4.1.5 Discretization of viscous fluxes

The viscous fluxes are usually composed of similar control volume as that of the convective fluxes to obtain a uniform spatial discretization. The viscous fluxes as given in Eqn. 2.16 are known to contain identical properties with the fluxes that were evaluated at the face of the control volume by the variables. Thus all the terms that are required namely the velocity components (u_1, u_2, u_3), with the dynamic viscosity μ and thermal conductivity κ for both the evaluation of stresses and viscous terms are subjected to averaging at control volume's face ($i+\frac{1}{2}$) (Ref. Fig. 4.2). The following subsections describe the discretization of viscous fluxes in brief.

Gradient approximation

Considering the viscous part f_v (Ref. Eq. 2.16) of the Navier-Stokes equation, the discretization of which is affected by the viscous stress tensor τ and thereby requiring the derivatives of velocity u and temperature T. In this thesis, a finite volume discretization of space $Sp_0(M)$ is used to approximate the unknown function W by specifying it as a sum of constant ansatz functions. An indicator function required for this ansatz is given as [3]

$$\mathbb{1}_{D_i}(x) \coloneqq \begin{cases} 1, & x \in D_i \\ 0, & else \end{cases}$$

to approximate W through the barycenters p_i of D_i by $W_h \in Sp_0(M)$,

$$W(x,t) \approx W_h(x,t), \qquad W_h(x,t) \coloneqq \sum_{i=1}^{N_{elem}} W_i(t)\mathbb{1}_{D_i}(x). \tag{4.18}$$

In this context the conservative variables are represented by the coefficients,

$$W_i(t) := \left(\rho(p_i,t)\,,\,(\rho u)(p_i,t)\,,\,(\rho E)(p_i,t)\right)^T, \quad i = 1,\ldots,N_{elem}. \tag{4.19}$$

Since the above function in Eq. 4.18 fails to indicate the gradients, further manipulations have to be encompassed to include all the relevant information into the scheme.

Green-Gauss gradient

The estimation of the gradients of the velocity components of the viscous fluxes given in Eqn. 2.16 and 2.5 can be done by using Green's theorem.

Definition 4.1.7. *Consider M to be a triangulation of D and $D_i,\ D_j \in M,\ i \neq j$. There is said to be a function*

$$g(x) := \sum_{i=1}^{N_{elem}} g_i \mathbb{1}_{D_i}(x), \quad g_i \in \mathbb{R}. \tag{4.20}$$

Definition 4.1.8. *Consider M to be a triangulation of D and $D_l \in M$. By using the function in Eq. 4.20, the Green-Gauss method of approximating the derivative in x_k direction for the control volume D_l is given as*

$$\left(\frac{\partial g(x)}{\partial x_k}\right)_{D_l}^{GG} = \begin{cases} \frac{1}{\mathrm{vol}D_l}\sum_{j\in\mathcal{N}(l)} \mathrm{svol}(e_{lj})\frac{n_{k,lj}}{2}\left(g_l, g_j\right), & x \in D_l \\ 0, & else. \end{cases} \tag{4.21}$$

This equation Eq. 4.21 is termed as **Green-Gauss gradient**.

The Green's theorem methodology is preferred with the finite volume method and it involves the development of an added control volume to compute the gradients. When these derivatives at the faces of the control volume are computed along with the values of the corresponding flow variables, the total contribution by viscous fluxes is obtained.

Thin shear layer approximation (TSL)

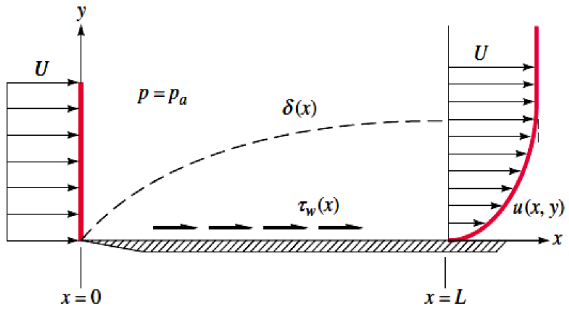

Credit: *Addisu Dagne Zegeye* [16].

Figure 4.4: Velocity profile on a boundary layer.

When flows with high Reynolds number are considered, viscous stresses play a major role in directing the flow towards the narrow region surrounding the profile of the body with the condition that there is no large boundary layer separation area Fig. 4.4. Resultantly, it can be assumed that gradients only in the normal direction influence the velocity, leading to the conclusion that the gradients from the other directions can be neglected. This condition is known as the *Thin shear layer approximation*.

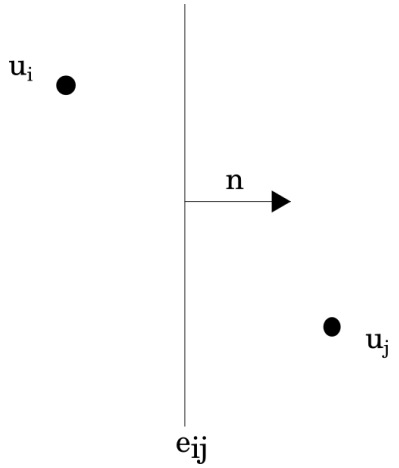

Figure 4.5: Thin shear layer approximation for the edge (face) [5].

According to the definition, the gradients only in the vertical (normal) direction are examined and the approximation follows as (Ref. Fig. 4.5),

$$\left(\frac{\partial u}{\partial x_i}\right)_{e_{ij}} \approx n_{k,ij}\frac{u_j - u_i}{\|p_i - pj\|_2} \tag{4.22}$$

TSL is applied for the approximation of the Navier-Stokes equations. The viscous terms that are computed are not only comparatively less expensive in computations but also considerably accurate. With the high Reynolds number flow cases, it is essential to refine the grid as fine as possible in the wall-normal direction so that the boundary layer can be resolved correctly whereas coarser grids are resolved in other directions.

Discretization of viscous terms

From Fig. 4.5, the discretization of the viscous flux $\langle f_c, n\rangle$ on the face e_{ij} is carried out by gathering information on either side of the face and averaging it as follows:

$$\begin{aligned}
\mu_{l,e_{ij}} &= \frac{1}{2}\Big(\mu_l(W_i) + \mu_l(W_j)\Big), \quad & \mu_{t,e_{ij}} &= \frac{1}{2}\Big(\mu_{t,i} + \mu_{t,j}\Big), \\
\kappa_{l,e_{ij}} &= \frac{1}{2}\Big(\kappa_l(W_i) + \kappa_l(W_j)\Big), \quad & \kappa_{t,e_{ij}} &= \frac{1}{2}\Big(\kappa_{t,i} + \kappa_{t,j}\Big), \\
\mu_{\text{eff},e_{ij}} &= \mu_{l,e_{ij}} + \mu_{t,e_{ij}}, & \kappa_{\text{eff},e_{ij}} &= \kappa_{l,e_{ij}} + \kappa_{t,e_{ij}}, \\
u_{e_{ij}} &= \frac{1}{2}\Big(u_i + u_j\Big).
\end{aligned} \tag{4.23}$$

Then follows the gradients for temperature and velocity for the complete discretization of the viscous fluxes. They can be determined by either of the following ways: By method of Green-Gauss Gradient:

$$\begin{aligned}
\left(\frac{\partial u}{\partial x_k}\right)^{\text{GG}}_{e_{ij}} &= \frac{1}{2}\left[\left(\frac{\partial u}{\partial x_k}\right)^{\text{GG}}_{D_i} + \left(\frac{\partial u}{\partial x_k}\right)^{\text{GG}}_{D_j}\right], \\
\left(\frac{\partial T}{\partial x_k}\right)^{\text{GG}}_{e_{ij}} &= \frac{1}{2}\left[\left(\frac{\partial T}{\partial x_k}\right)^{\text{GG}}_{D_i} + \left(\frac{\partial T}{\partial x_k}\right)^{\text{GG}}_{D_j}\right],
\end{aligned} \tag{4.24}$$

or by the method of TSL:

$$\begin{aligned}\left(\frac{\partial u}{\partial x_k}\right)_{e_{ij}}^{\text{TSL}} &= \frac{n_{k,ij}}{\text{dist}(e_{ij})}\left(u_j - u_i\right),\\ \left(\frac{\partial T}{\partial x_k}\right)_{e_{ij}}^{\text{TSL}} &= \frac{n_{k,ij}}{\text{dist}(e_{ij})}\left(T_j - T_i\right),\end{aligned} \tag{4.25}$$

$$\Rightarrow \int_{e_{ij}} \langle f_v(W_h), n_{e_{ij}}\rangle \, ds \;\approx\; \text{svol}(e_{ij})\langle f_v(W_{\mathcal{N}(i,j)}), n_{e_{ij}}\rangle \tag{4.26}$$

Discrete set of equations

The mean flow equation (2.1) can be represented by the ansatz function obtained from the equations (4.18) and (4.19) i.e., the coefficient vector,

$$\mathbf{W}_{\text{mean}}(t) \;:=\; \left(W_1(t), \ldots, W_{N_{elem}}(t)\right). \tag{4.27}$$

The mean flow equations (2.1) are then discretized forming the system of ordinary differential equations

$$\frac{d}{dt}\mathbf{W}_{\text{mean}}(t) \;=\; -\mathbf{M}_{\text{mean}}^{-1}\mathbf{R}_{\text{mean}}(\mathbf{W}(t)), \tag{4.28}$$

where $\mathbf{M}_{\text{mean}} := \text{diag}(\text{diag}(\text{vol}(D_i))) \in \mathbb{R}^{5N_{elem}\times 5N_{elem}}$ is the mass matrix of mean flow equatins Eq. 2.1.

In order to compute the solution of Eq. 4.28 assumptions are made such that the mean flow equations are dependent on $\mathbf{W}$ where $\mathbf{W}_t$ is seen as a variable. For the turbulence flow equations the converse holds (where flow is dependent on $\mathbf{W}_t$ and $\mathbf{W}$ is the variable. Therefore, Eq. 4.28 can be altered as

$$\frac{d}{dt}\mathbf{W}(t) \;=\; -\mathbf{M}_{\text{mean}}^{-1}\mathbf{R}_{\text{mean}}(\mathbf{W}(t);\mathbf{W}_t(t)), \tag{4.29a}$$

$$\frac{d}{dt}\mathbf{W}_t(t) \;=\; -\mathbf{M}_{\text{turb}}^{-1}\mathbf{R}_{\text{turb}}(\mathbf{W}_t(t);\mathbf{W}(t)). \tag{4.29b}$$

The equations 4.29a and 4.29b are then solved with focus on obtaining steady state solutions. Accordingly, in the Eq. 4.28 the left hand side terms approach zero.

$$\frac{d}{dt}\mathbf{W}(t) \;=\; 0, \quad \frac{d}{dt}\mathbf{W}_t(t) \;=\; 0. \tag{4.30}$$

By this assumption the system of equations (4.29) is reduced to

$$0 = \; \mathbf{R}_{\text{mean}}(\mathbf{W}(t);\mathbf{W}_t(t)), \tag{4.31a}$$

$$0 \;=\; \mathbf{R}_{\text{turb}}(\mathbf{W}_t(t);\mathbf{W}(t)). \tag{4.31b}$$

These equations describe nonlinear set of equations that will be solved further by the forthcoming methodologies that are explained in Sec. 4.3.

4.2 Discretization of Boundary

To perform any numerical simulation, it is only possible to take into account a segment of the real physical domain. When the domain is cut back, it leads to the development of artificial boundaries, whereby the need for specification of values of certain physical quantities rises. Also, the walls that are disclosed to the flow can be assumed as natural boundaries of the physical domain. Specifying the values for the boundary plays a major role during any numerical treatment because the stability of the solution and also the convergence speed depends highly on the boundary discretization.

The following are the main types of boundary when Euler and Navier-Stokes equation are involved and also dealt with in this thesis [10],

- adiabatic solid wall,
- far-field Riemann in the external regions,
- symmetry plane,
- for constant pressure inflows: reservoir-pressure inflow, and
- for constant pressure outflows: exit-pressure outflow.

4.2.1 General treatment of boundary

The flux over the edge $e_{i,bdry}$ should satisfy its corresponding boundary conditions and this is done by flux formulations. The flux computation requires an outer artificial state to be specified, which is prescribed as [3],

$$W_{i,bdry} \;=\; \Big(\rho_{i,bdry}(t),\; (\rho u)_{i,bdry}(t),\; (\rho E)_{i,bdry}(t)\Big)\,. \tag{4.32}$$

and in case of turbulence flow equations additional boundary term such as $\tilde{\nu}_{i,bdry}$ (SA model) needs to be computed.

Successively, the boundary integrals are approximates as follows

$$\begin{aligned}\int_{\partial D_i} \langle f_c(W), n\rangle \, ds \;&\approx\; \sum_{i=1}^{N_{bdry}} \int_{e_{i,bdry}} \mathcal{H}^{1st,Roe}\Big(W_i,\; W_{i,bdry},\; n_{i,bdry}\Big)\, ds \\ &\approx\; \sum_{i=1}^{N_{bdry}} \text{svol}\Big(e_{i,bdry}\Big)\; \mathcal{H}^{1st,Roe}\Big(W_i,\; W_{i,bdry},\; n_{i,bdry}\Big)\,.\end{aligned} \tag{4.33}$$

To attain stability in regions of the solid wall the numerical flux function $\mathcal{H}$ is replaced here by $\mathcal{H}^{1st,Roe}$.

4.2.2 No-slip wall boundary conditions

The viscous and turbulent flow problems are dealt with the no-slip wall boundary conditions. For simplification, considering the flow in two directions (x, y), with time t, u_1, u_2 as the velocity components, and pressure p the no-slip boundary conditions for the Navier-Stokes equations are as follows [17]:

$$\begin{aligned} u_{1,x} + u_{2,y} \;&=\; 0, \\ \rho\Big(u_{1,t} + u_1 u_{1,x} + u_2 u_{1,y}\Big) \;&=\; -p_x + \mu\Big(u_{1,xx} + u_{1,yy}\Big)\,, \\ \rho\Big(u_{2,t} + u_1 u_{2,x} + u_2 u_{2,y}\Big) \;&=\; -p_y + \mu\Big(u_{2,xx} + u_{2,yy}\Big)\,. \end{aligned} \tag{4.34}$$

The subscripts in Eq. 4.34 indicate pde. $u_{1,t} = \frac{\partial u_1}{\partial t}$ and $u_{1,x} = \frac{\partial u_1}{\partial x}$ and $u_{1,xx} = \frac{\partial^2 u_1}{\partial x^2}$. Since in all of the test cases the wall is specified to be adiabatic, heat transfer across the wall is set to zero.

4.2.3 Farfield boundary conditions

The boundary which determines the inflow of the free-stream conditions of the fluid is the farfield boundary conditions. When an angle of attack α is specified, the outer state is described as follows:

$$W_{i,bdry} \coloneqq W_\infty \coloneqq \begin{pmatrix} \rho_\infty \\ \cos\alpha\rho_\infty u_\infty \\ 0 \\ \sin\alpha\rho_\infty u_\infty \\ \rho_\infty E_\infty \end{pmatrix}. \tag{4.35}$$

This marks the end of spatial discretization, when the inviscid fluxes are summed up, which leads to the time-integration of the computed approximated governing equations that are discussed in the next section.

4.3 Temporal Discretization

The section focuses on the need to develop a flexible algorithm for the discretization of RANS equations and highlights the general solution methodology for the non-linear equations. The general flow of the structure of the algorithm is shown in Fig. 4.6. The non-linear multigrid method with the implicit Runge-Kutta method that is employed to proceed to the linear solution method along with the preconditioners needed is all discussed under this section.

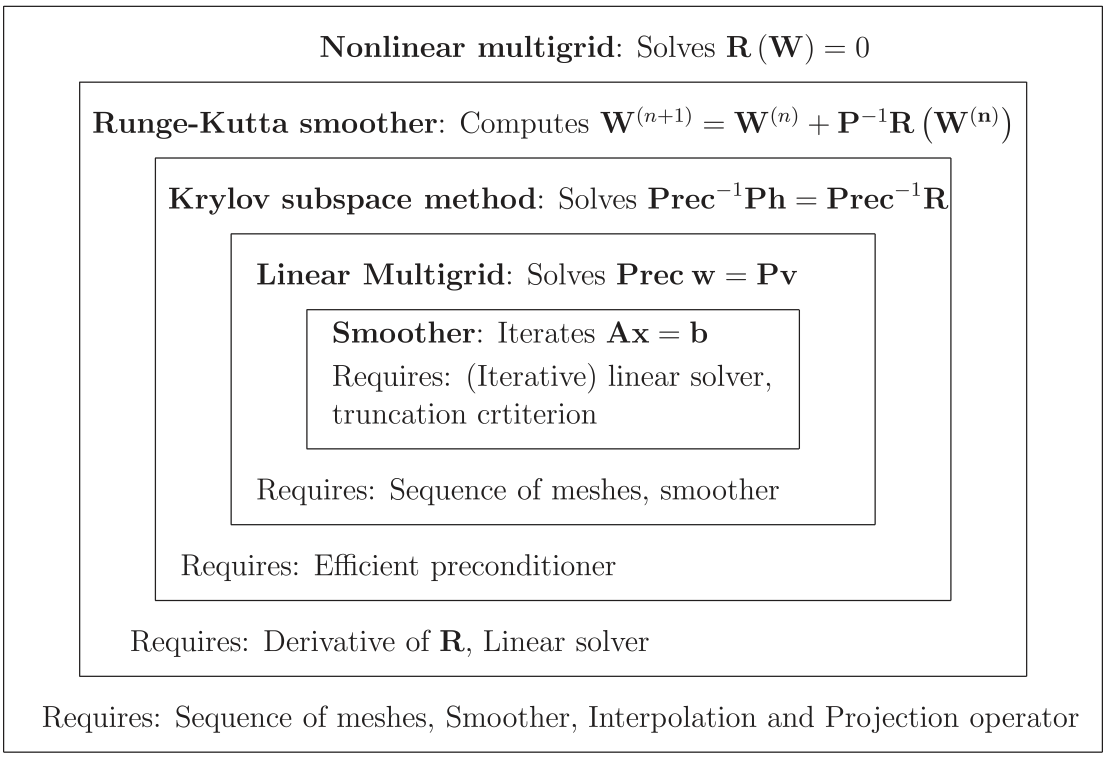

Figure 4.6: Structure of algorithm for non-linear solution method [3, p. 149].

The concept of *method of lines* renders the discretization of spatial and temporal components of the governing equations regarding each of the control volume, building a system of equations (ordinary differential equations-ode) that is time reliant. The time-stepping methods that are used

to evaluate a particular scheme are applied to the structured and unstructured grids and the step-by-step procedure is explained in the following sections.

4.3.1 Nonlinear multigrid

For solving the algebraic system of equations approximately, the concept of the nonlinear multigrid method known as *Full Approximation Scheme* (FAS) is adopted [18] [19]. The basic idea of nonlinear multigrid lies in smoothing the errors. There is the requirement for a sequence of meshes, wherein these errors are represented. The errors on these coarse meshes are subject to smoothing and the resulting corrections are then interpolated to the corresponding fine grid.

The non-linear multigrid algorithm flows in the following way: A sequence of meshes is taken and agglomeration is carried out on them. This is further defined by suitable projection and interpolation operators for the transfer of information. Finally, suitable smoothers are developed. Every single procedure is described in this section and Sec. 4.3.2.

Agglomeration

Definition 4.3.1. *Consider that*

$$M \;=\; \{D_i : i = 1, \ldots, N_{elem}\} \text{ and } M' \;=\; \{D'_i : i = 1, \ldots, N'_{elem}, \} \tag{4.36}$$

where M represents the triangulation of the bounded domain $D \subset \mathbb{R}^m$.

A sequence of triangulations is needed to develop a multigrid algorithm

$$M_n \;\subset\; \ldots \;\subset M_1.$$

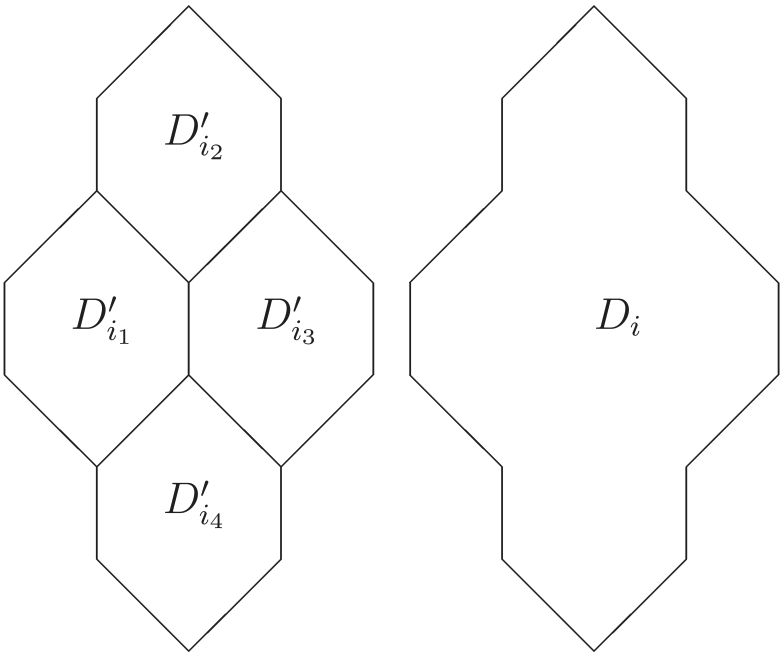

Figure 4.7: Four cells of a dual grid (left) and their agglomerated cell (right) [3, p. 152].

For dealing with meshes in large scale applications that contain sizable anisotropic cells, a directional agglomeration strategy in induced. The usual working is that a predetermined number of points are selected in a line of a fine grid, and these are fused to form one coarse cell as shown

in Fig. 4.7. In general, the fusing of two points is preferred in the interest of significantly reducing the stiffness caused by the mesh on the agglomerated grids. This ensures that for the sequence of agglomerated meshes, the complexity reduces by a factor of 2 within further progressive levels. The isotropic mesh part-**MGridGen** is commonly applied for the regions in the mesh where information about a line is not available, which approximately generates a $4:1$ fusing in $2D$ and $8:1$ fusing in $3D$ cells.

The agglomeration coarsening is of two categories. There exists in the mesh, an isotropic far-field and anisotropy near the viscous wall (no-slip). The graph coarsening algorithm MGridGen can be applied to the far-field region but does not work on the anisotropic mesh area. Hence, a pseudo mesh is developed for the anisotropic part and is fed into MGridGen, wherein the predetermined lines are transformed correspondingly to be represented as points. Then the usual coarsening is performed on the pseudo mesh and afterward, these points are unloaded in the coarse mesh. These are further coarsened by the basic strategy of fusing two adjacent cells, leading to the coarsening ratio of $2:1$ defined along all the lines. The remaining area has the coarsening ratio defined by MGridGen.

Projection and Interpolation operator

Once the coarse grids are obtained, projection and interpolation operators are required to effectively transfer information between successive grids. To develop the nonlinear FAS, the following nonlinear equation is considered:

$$\mathbf{R}_{M_1} \; : \; \mathbb{R}^{\#M_1} \; \rightarrow \; \mathbb{R}^{\#M_1}, \quad \mathbf{R}_{M_1}(\mathbf{W}_{M_1}) \; = \; \mathbf{f}_{M_1}), \tag{4.37}$$

where, the operator $\mathbf{R}_{M_1}$ is to represent in a mesh, the discretization involving either a partial difference equation or an integral equation.

Furthermore, the operators for the Eq. 4.37 is defined for $2 \leq k \leq n$ as:

$$\begin{aligned} P_{M_k}^{M_{k-1}} \; &: \; \mathbb{R}^{\#M_{k-1}} \; \rightarrow \; \mathbb{R}^{\#M_k}, \\ I_{M_k}^{M_{k-1}} \; &: \; \mathbb{R}^{\#M_k} \; \rightarrow \; \mathbb{R}^{\#M_{k-1}}. \end{aligned} \tag{4.38}$$

where

$$\begin{aligned} P_{M_k}^{M_{k-1}} \; &:= \left(\frac{1}{\mathrm{vol} D_i} \left(\mathrm{vol}\left(D_{i1}^{'}\right), \ldots, \mathrm{vol}\left(D_{iN}^{'}\right) \right) \right)_{i=1,\ldots,N_{elem}}, \\ I_{M_k}^{M_{k-1}} \; &:= (1_{i1}, \ldots, 1_{iN})_{i=1,\ldots,N_{elem}}^{T} \end{aligned} \tag{4.39}$$

From Eq. 4.38 the operator $P_{M_k}^{M_{k-1}}$ is termed as the *projection operator*, which instigates the projection from a fine mesh to the immediate next coarser mesh. Similarly, the operator $I_{M_k}^{M_{k-1}}$ is the *interpolation operator* that is responsible for information transfer from one coarse mesh to the successive finer mesh.

The multigrid, in general, can be constituted as a prototype by the *cycling strategies*, that are chosen to be defined either as explicit or recursive. Noted cycling strategies include the *V*-cycles, *W*-cycles and the *F*-cycles.

4.3.2 Runge-Kutta smoother

The nonlinear system of equations given in Eq. 4.31a and 4.31b are to be discretized in consideration with 4.29. Time accurate methods do not tend to be the objective of the discretization. For this reason, a smoother that is based on multistage implicit Runge-Kutta (RK) smoother is derived. An s-stage, diagonally implicit RK method that is attained from the butcher scheme:

c	$\mathcal{A}$
	b^T

Table 4.1: Butcher scheme [3, p, 163].

where

$$\mathcal{A} \coloneqq \begin{pmatrix} \alpha_{11} & 0 & \dots & 0 \\ \alpha_{22} & \ddots & \ddots & \vdots \\ \vdots & \ddots & \ddots & 0 \\ 0 & \dots & \alpha_{s,s-1} & \alpha_{ss} \end{pmatrix}, \quad b \coloneqq \begin{pmatrix} 0 \\ \vdots \\ 0 \\ \alpha_{s+1,s} \end{pmatrix}, \quad \text{and} \quad c \coloneqq \begin{pmatrix} 0 \\ \vdots \\ 0 \end{pmatrix}. \tag{4.40}$$

The discrete evolution at T_n is indicated by $\mathbf{W}^{T_n}$ and when the Butcher scheme is applied to Eqn. 4.29a and 4.29b the stages along with the further discrete evolution is given as [3]:

$$\begin{aligned} k_1 &= -\mathbf{M}^{-1}\mathbf{R}\left(\mathbf{W}^{T_n} + \alpha_{11}\Delta t k_1\right) \\ k_2 &= -\mathbf{M}^{-1}\mathbf{R}\left(\mathbf{W}^{T_n} + \alpha_{21}\Delta t k_1 + \alpha_{22}\Delta t k_2\right) \\ &\vdots \\ k_s &= -\mathbf{M}^{-1}\mathbf{R}\left(\mathbf{W}^{T_n} + \alpha_{s,s-1}\Delta t k_{s-1} + \alpha_{ss}\Delta t k_s\right) \\ \mathbf{W}^{T_{n+1}} &= \mathbf{W}^{T_n} + \alpha_{s+1,s}\Delta t k_s. \end{aligned} \tag{4.41}$$

Newton's method is applied to approximate the solution of the nonlinear systems $k_1, \dots, k_s$ wherein the method is truncated after only one iteration so as to approximate the root of the function

$$g_j(k) \coloneqq k + \mathbf{M}^{-1}\mathbf{R}\left(\mathbf{W}^{T_n} + \alpha_{j,j-1}\Delta t k_{j-1} + \alpha_{jj}\Delta t k\right)$$

and the derivative is given as

$$\frac{dg_j(k)}{dk} = \mathbf{I} + \alpha_{jj}\Delta t \mathbf{M}^{-1}\frac{d\mathbf{R}}{d\mathbf{W}}\left(\mathbf{W}^{T_n} + \alpha_{j,j-1}\Delta t k_{j-1} + \alpha_{jj}\Delta t k\right),$$

where the initial guess is taken as $k^{(0)} = 0$. Hence an approximate root for the stages $j = 1, \dots, s$ is given by

$$k_j = -\left[\frac{dg_j\left(k^{(0)}\right)}{dk}\right]^{-1}\left(g_j\left(k_j^{(0)}\right)\right). \tag{4.42}$$

With the approximate root defined by Eqn. 4.42, the implicit RK method in Eqn. 4.41 can be

reformulated into the following algorithm

$$\begin{aligned}
k_1 &= -\left[\frac{dg_1\left(k^{(0)}\right)}{dk}\right]^{-1} \mathbf{M}^{-1}\mathbf{R}\left(\mathbf{W}^{T_n}\right) \\
k_2 &= -\left[\frac{dg_2\left(k^{(0)}\right)}{dk}\right]^{-1} \mathbf{M}^{-1}\mathbf{R}\left(\mathbf{W}^{T_n} + \alpha_{21}\Delta t k_1\right) \\
&\vdots \\
k_s &= -\left[\frac{dg_s\left(k^{(0)}\right)}{dk}\right]^{-1} \mathbf{M}^{-1}\mathbf{R}\left(\mathbf{W}^{T_n} + \alpha_{s,s-1}\Delta t k_{s-1}\right) \\
\mathbf{W}^{T_{n+1}} &= \mathbf{W}^{T_n} + \alpha_{s+1,s}\Delta t k_s.
\end{aligned} \tag{4.43}$$

With the updates $\mathbf{W}^{(0)} := \mathbf{W}^{T_n}$ and

$$\mathbf{W}^{(j)} := \mathbf{W}^{T_n} - \alpha_{j+1,j}\Delta t\left[\frac{dg_j\left(k^{(0)}\right)}{dk}\right]^{-1} \mathbf{M}^{-1}\mathbf{R}\left(\mathbf{W}^{(j-1)}\right)$$

the RK scheme represented as Eqn. 4.43 can be rewritten as

$$\begin{aligned}
\mathbf{W}^{(0)} &:= \mathbf{W}^{T_n} \\
\mathbf{W}^{(1)} &:= \mathbf{W}^{(0)} - \alpha_{21}\Delta t\left[\frac{dg_1\left(k^{(0)}\right)}{dk}\right]^{-1} \mathbf{M}^{-1}\mathbf{R}\left(\mathbf{W}^{(0)}\right) \\
&\vdots \\
\mathbf{W}^{(s)} &:= \mathbf{W}^{(0)} - \alpha_{s+1,s}\Delta t\left[\frac{dg_s\left(k^{(0)}\right)}{dk}\right]^{-1} \mathbf{M}^{-1}\mathbf{R}\left(\mathbf{W}^{(s-1)}\right) \\
\mathbf{W}^{T_{n+1}} &= \mathbf{W}^{(s)}.
\end{aligned} \tag{4.44}$$

With the algorithm indicated in Eqn. 4.44 it is essential to solve for each stage the linear equation

$$\frac{dg_j\left(k^{(0)}\right)}{dk}\mathbf{x}_j = \alpha_{j+1,j}\Delta t\mathbf{M}^{-1}\mathbf{R}\left(\mathbf{W}^{(j-1)}\right).$$

An equivalent formulation of this linear equation can be specified as

$$\left((\Delta t)^{-1}\mathbf{M} + \alpha_{jj}\frac{d\mathbf{R}}{d\mathbf{W}}(\mathbf{W}^{(j-1)})\right)\mathbf{x}_j = \alpha_{j+1,j}\mathbf{R}\left(\mathbf{W}^{(j-1)}\right). \tag{4.45}$$

Since the focus is not on time accurate methods, further acceleration techniques can be applied to modify the scheme. The steady state time step Δt in Eqn. 4.45 is substituted with the local time step $\Delta T := \mathrm{diag}(\mathrm{diag}(\Delta t_i)) \in \mathbb{R}^{N_{eq}N\times N_{eq}N}$, where $N_{eq} = 5$ corresponding to the mean flow equations and $N_{eq} = N_t$ corresponding to the turbulent flow equations.

Proceeding with further acceleration techniques that permit over- and under relaxation, a relaxation parameter ε is introduced. In conclusion, a linear operator $\mathbf{P}_j$ for the stages j with the residual $\mathbf{R}$ is specified such that Eqn. 4.45 can be rewritten as:

$$\mathbf{P}_j \;=\; (\Delta T)^{-1}\mathbf{M} \;+\; \varepsilon\alpha_{jj}\frac{d\mathbf{R}}{d\mathbf{W}}\left(\mathbf{W}^{(j-1)}\right), \tag{4.46}$$

which is obtained from the general representation [20]

$$\left((\Delta T)^{-1}\mathbf{M} \;+\; \varepsilon\alpha_{jj}\frac{d\mathbf{R}}{d\mathbf{W}}(\mathbf{W}^{(j-1)})\right)\mathbf{x}_j \;=\; \alpha_{j+1,j}\mathbf{R}\left(\mathbf{W}^{(j-1)}\right). \tag{4.47}$$

The end-product is the of Newton method resulting in the stated multistage implicit Runge-Kutta method.

$$\begin{aligned}
\mathbf{W}^{(0)} &:= \mathbf{W}^{T_n} \\
\mathbf{W}^{(1)} &:= \mathbf{W}^{(0)} \;-\; (\mathbf{P}_1)^{-1}\mathbf{R}(\mathbf{W}^{(0)}) \\
&\vdots \\
\mathbf{W}^{(s)} &:= \mathbf{W}^{(0)} \;-\; (\mathbf{P}_s)^{-1}\mathbf{R}(\mathbf{W}^{(s-1)}) \\
\mathbf{W}^{T_{n+1}} &= \mathbf{W}^{(s)}.
\end{aligned} \tag{4.48}$$

where $\mathbf{W}^{T_n}$ is the discrete evolution at T_n. The application of the butcher scheme leads to the further stages (left hand side) and discrete evolution (right hand side) of the solution.

Once the non-linear multigrid algorithm is completed, it results in a system of linear equations that are then approximated efficiently using linear iterative methods. The flow of linear solution methods is described in Sec. 4.3.3.

4.3.3 Linear solution methods

The large-scale linear equations obtained in Eq. 4.46 is by analysis found to be an ill-conditioned system that needs further manipulations to gather solutions. Krylov subspace methods, that are free of matrices are preferred so that the linear solutions can be approximated within a limited number of steps, are explained in the resulting subsection.

Krylov subspace methods

There exists in general various Krylov subspace methods, with the same basic idea. The purpose is to construct a particular Krylov subspace wherein for the given linear system of equations an approximate solution in the low-dimensional space $\mathcal{K}(A, b)$, where $k << n$ is evaluated.

$$\mathcal{K}(A, b) \;=\; \text{span}\left\{b, Ab, A^2b, \ldots, A^kb\right\}. \tag{4.49}$$

When there exists the relation between matrix A and vector b as given in Eq. 4.50, then there can exist a satisfactory approximate solution $x^\dagger$ such that $x^\dagger \in \mathcal{K}(A, b)$, i.e.,

$$Ax \;=\; b, \quad x^\dagger \approx x. \tag{4.50}$$

The Krylov subspace methods work efficiently along with a suitable preconditioner. The process by which an appropriate preconditioner is selected and constructed is characterized in Sec. 4.3.4.

4.3.4 Construction of Preconditioner

The linear system of equations need to be approximately solved by,

$$\mathbf{Prec}_j^{scalar} \approx \mathbf{Prec}_j \mathbf{w} \;=\; \mathbf{P}_j \mathbf{v}_k. \tag{4.51}$$

Designing of the preconditioner involves two parts [5]:

- the existing linear operator $\mathbf{Prec}_j$,
- a linear iterative method to obtain solutions by approximation.

The exact residual for the Jacobian in Eq. 4.46 is replaced by an modification that satisfies $\tilde{\mathbf{R}} \approx \mathbf{R}$ is taken to be the preconditioner.

Finally it is acceptable to assume that,

$$\mathbf{Prec}_j \approx \mathbf{P}_j. \tag{4.52}$$

This leads to the formation of the final preconditioner from Eq. 4.46, i.e.,

$$\mathbf{Prec}_j \;:=\; (\Delta T)^{-1}\mathbf{M} \;+\; \varepsilon\alpha_{jj}\frac{d\tilde{\mathbf{R}}_{\text{prec}}^{\text{comp}}}{d\mathbf{W}}\left(\mathbf{W}^{(j-1)}\right), \tag{4.53}$$

where the subscript **prec** denotes preconditioning and the superscript **comp** denotes compact discretization.

To have an effective preconditioner it is essential to approximate a solution to the linear system of equations. To approximately solve the equations, iterative linear multigrid solution methods are applied. This is illustrated in the Sec. 4.3.5.

4.3.5 Iterative solution methods for linear equations

Proceeding with the design for preconditioners, once the operator is developed there comes the responsibility of defining a proper linear multigrid method to efficiently solve the linear system of equations. In order to compute the linear multigrid algorithm from Eq. 4.37 corresponding to Sec. 4.3.3 the following notation is used

$$A_{M_k} \coloneqq \mathbf{Prec}_j \;:\; \mathbb{R}^{\#M_k} \to \mathbb{R}^{\#M_k}, \qquad A_{M_k} x_{M_k} \;=\; b_{M_k}. \tag{4.54}$$

There is a need to extend the method in Sec. 4.3.3 to a system of equations for Navier-Stokes equations. Doing so, results in each entry of $\mathbf{Prec}_j$ being a 5×5 block matrix. Applying all the prescribed changes the following is formulated

$$A_{M_k} \coloneqq \begin{pmatrix} A_{11} & \dots & \dots & A_{1n} \\ \vdots & \ddots & \ddots & \vdots \\ \vdots & \ddots & \ddots & \vdots \\ A_{n1} & \dots & \dots & A_{nn} \end{pmatrix}, \quad A_{ij} \in \mathbb{R}^{5\times 5}, \tag{4.55}$$

$$x_{M_k} \in \mathbb{R}^{5\times 5}, \quad b_{M_k} \in \mathbb{R}^{5\times 5}.$$

Ensuing these considerations there arises the demand to include a smoother for the linear multigrid method. The *Line symmetric Gauss-Seidel* (LU-SGS) method is chosen as an approximate smoother. From Eq. 4.54 and 4.55, Gauss-Seidel method for block systems can be written as:

$$x_i^{(k+1)} \;=\; \left(A_{i,i}\right)^{-1}\left(b_i \;-\; \sum_{j=1}^{i-1} A_{i,j}x_j^{(k+1)} \;-\; \sum_{j=i+1}^{N_{elem}} A_{i,j}x_j^{(k)}\right). \tag{4.56}$$

Considering the RANS equations along with the SA-neg turbulence model upon which the discretization techniques and boundary conditions are applied, five simple benchmark test cases are taken for the experimental purpose of this thesis. The description along with the parameters specifying the flow for each of the test cases are explained in detail in the following Chap. 5.

Chapter 5

Discussion of Test cases

The goal of this thesis is to apply the discretization and solution methodologies that were discussed in the previous chapters and apply them to five benchmark test cases. The geometry, boundary and flow conditions are individually addressed for each of the test cases. The computational meshes are available as a *FORTRAN* code at the TMR website [1]. For each of the test cases a family of meshes has been generated from the FORTRAN code with the filename extension of *cgns* and for structured grids in *PLOT3D* format. These files were then imported into the mesh generation software *POINTWISE V 18.1* wherein the general boundary conditions for the meshes were mentioned. Finally, the meshes were exported to the machine-readable TAU format file. The simulation is set up for the test cases with the flow conditions as discussed in the following sections.

5.1 Flat plate configuration

The finite flat plate test case aims to perform numerical simulations on a cascade of finite flat plates to understand the characteristics such as the grid convergence, order of accuracy, etc., due to turbulent flows. The results obtained are validated against the reference solutions from other methods such as CFL3D, FUN3D [21], and TAU.

Geometry and Boundary Conditions

The finite flat plate test case is per the **"2D Finite Flat Plate"** benchmark test case described under the **" Cases and Grids for Turbulence Model Numerical Analysis"** section at the TMR website [1]. The x- and z axes of the coordinate system indicate the flow direction of the stream (horizontal) and the vertical directions respectively. In the computational domain $(-2 \leq x \leq 4, 0 \leq z \leq 4)$, the flat plate lies in the region of $(0 \leq x \leq 2,\ z = 0)$. The domain differs from the "2D Zero Pressure Gradient Flat Plate Verification Case" that is described in the "Turbulence Model Verification Cases and Grids" section of the TMR website in that, the grid of the domain is extended in the upstream and downstream direction corresponding to the plate, by which a trailing edge has been developed at $z_{TE} = 0, x_{TE} = 2$ [22]. This trailing edge specification is so done because of the drag coefficient to fall within 0.02 counts of the existing coefficient that is calculated on such a domain wherein the boundaries extend to infinity.

The boundary conditions are as follows: The boundary of the viscous wall (at the surface of the plate) is set to adiabatic no-slip conditions $(0 \leq x \leq 2, z = 0)$. The top of the domain is set to symmetry boundary condition to abstain from specifying the external state at this region $(-2 \leq x \leq 4, z = 4)$. At the upstream boundary is defined a reservoir-pressure inflow condition that corresponds to constant total pressure boundary conditions: $P_t/P_{ref} = 1.02828$, and $T_t/T_{ref} = 1.008$ in the region $(x = -2,\ 0 \leq z \leq 4)$. Also, at the downstream boundary $(-2 \leq x \leq 0$ and $2 \leq$

$x \leq 4,\ z = 0$) is specified constant pressure conditions $P/P_{ref} = 1$ which is set to exit-pressure boundary condition. The boundary conditions in general is described in Fig. 5.1.

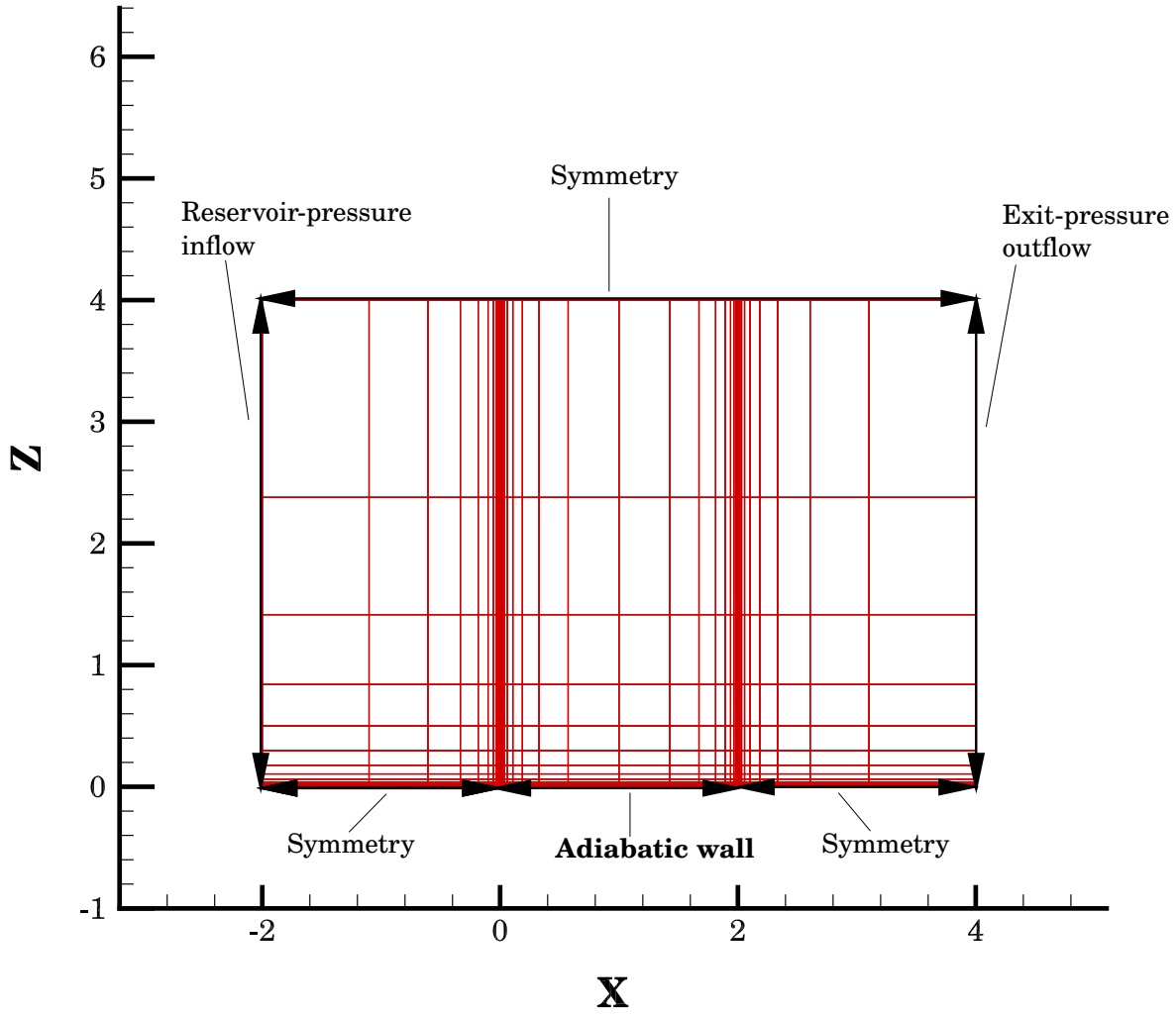

Figure 5.1: Boundary Conditions for finite flat plate geometry; 81 × 25 grid is shown

Flow conditions

An compressible turbulent flow is presumed over the flat plate with $Ma = 0.2$ and Reynolds number based on unit length of the grid $Re = 5\ million$. The Prandtl number is assumed to be a constant at $Pr = 0.72$, and the turbulent Prandtl number is assumed the constant $Pr_t = 0.9$. The farfield inflow turbulent flow variable for the SA model is $\tilde{\nu}_{farfield} = 3\nu_\infty$. From the Sutherland's Law, molecular viscosity for the flow is calculated (Ref. Eq. 3.9).

Computational mesh

A series of rectilinear-nested (stretched) grids of the same family are considered for the test case. They range from 21×7 (coarsest) to $2,561 \times 769$ (finest). This grid notation represents the numbers in the form of points that lie on the streamwise (x-axis) and vertical directions (z-axis) respectively, wherein the spanwise direction is indicated by the y-axis. Table 5.1 provides a summary of the grid elements. Each grid is extracted from a Fortran code that outputs the grids in PLOT3D format. This unformatted PLOT3D grid represents the grid in the size of $nl \times nj \times nk$,

Grid	Family 1 (hex)	
	Cells	Nodes
L1	1,966,080	3,938,818
L2	491,520	986,370
L3	122,880	247,426
L4	30,720	62,274

Table 5.1: Statistics of four finest grids for $2D$ Finite flat plate grid family

where $nl = 2$ is the number of points that lie in the spanwise region, and nj and nk represent the number of points in the streamwise and normal directions respectively. Each coarser grid differs in that, it is given as every-other-point exactly of the finer grid, ranging from the finest to the coarsest mesh. The non-dimensionalized grids are stretched in the wall-normal direction. Special attention is paid to the mesh refinement around the leading and trailing edge, where is grid points are comparatively dense. This clustering in the leading edge in the x-axis is defined by the local aspect ration $(AR_{LE} = 1)$, which is analogous to the trailing edge. At the wall of the finest grid, the normal spacing is 2.5×10^{-7}. This relates itself to the non-dimensional $z^+ = 0.1$ boundary layer in the region $x \approx 1$ (at the center of the plate). Fig. 5.1 is a view of the 81×25 grid domain.

5.2 NACA 0012 Airfoil

This study aims to validate the simulated data for the flow around a NACA 0012 with a sharp trailing edge against existing reference solutions of the SA turbulence model. The case is investigated for the variation of lift, drag, pressure coefficient, etc., and is held in comparison with the solution obtained from other discretization methods.

Geometry and Boundary Conditions

The simulated test case corresponds to the **"2D NACA 0012 Airfoil"** under the section **"Cases and Grids for Turbulence Model Numerical Analysis"** of the TMR website [1]. The flow parameters are chosen according to the description of the reference case "2D NACA 0012 Airfoil Validation Case" under the "Turbulence Model Verification Cases and Grids" section of the TMR website. The redacted formula for the development of NACA 0012 geometry for the experiment to have a closed trailing edge is as follows:

$$y = \pm 0.594689181 * [0.298222773 * \sqrt{x} - 0.127125232 * x - 0.357907906 * x^2 + 0.291984971 * x^3 - 0.105174606 * x^4] \quad (5.1)$$

The airfoil spans from $x = 0$ and $x = 1.008930411365$, with a chord length $l_c = 1$. In order to minimize the effect of boundary conditions on the near-field solution, all far-field boundaries are placed at a distance of atleast $500\ l_c$.

The boundary conditions are as specified: An adiabatic no-slip boundary condition is specified on the surface of the airfoil. A C-grid topology enclosing the computational domain with the top and bottom planes are set to symmetry plane boundary. The upstream direction of flow $(-500 < x < 1)$ up to the leading edge and the downstream flow $(1 < x < 500)$ following the direction of the flow from the trailing edge are taken as far-field boundary. Two symmetry plane boundaries lie at $y = 0$ and at $y = 1$.

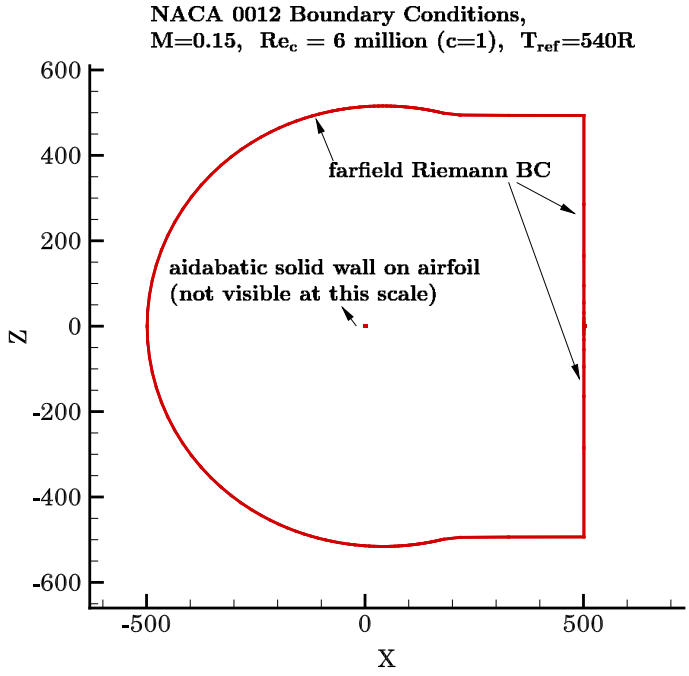

Figure 5.2: Domain and boundary conditions of NACA 0012 airfoil.

Flow conditions

The airfoil is placed under a compressible uniform turbulent flow $(Ma = 0.15)$ with the specified angles of attack (AoA): 0°, 10°, 15°. The freestream static temperature is $T_{ref} = 540°$ Rankine. The chord based Reynolds number $Re = 6\ million$. The Prandtl number is assumed to be a constant at $Pr = 0.72$, and the turbulent Prandtl number is assumed the constant $Pr_t = 0.9$. The farfield inflow turbulent flow variable for the SA model is $\tilde{\nu}_{farfield} = 3\nu_\infty$. The heat capacity ration is taken as $\gamma = 1.4$. From the Sutherland's Law, molecular viscosity for the flow is calculated (Ref. Eq. 3.9).

Computational mesh

Grid	Family 1 (hex)	
	Cells	Nodes
L1	14,680,064	29,375,484
L2	3,670,016	7,347,710
L3	917,504	1,838,848
L4	229,376	460,672

Table 5.2: Statistics of four finest grids for $2D$ NACA0012 grid family

A family of seven nested structured grids is generated ranging from the coarsest (113×13) to the finest (7169×2049) for the experiment. Figure 5.3 and 5.4a and 5.4b shows the view of a 449×129 grid from the family. Table 5.2 provides a summary of the grid elements. Each coarser grid differs in that, it is given as every-other-point exactly of the finer grid, ranging from the finest to the coarsest mesh. The hexahedral mesh around the airfoil has been generated using a 'C-grid' topology. The finest mesh contains 4,097 points on the airfoil surface with 1,537 points in

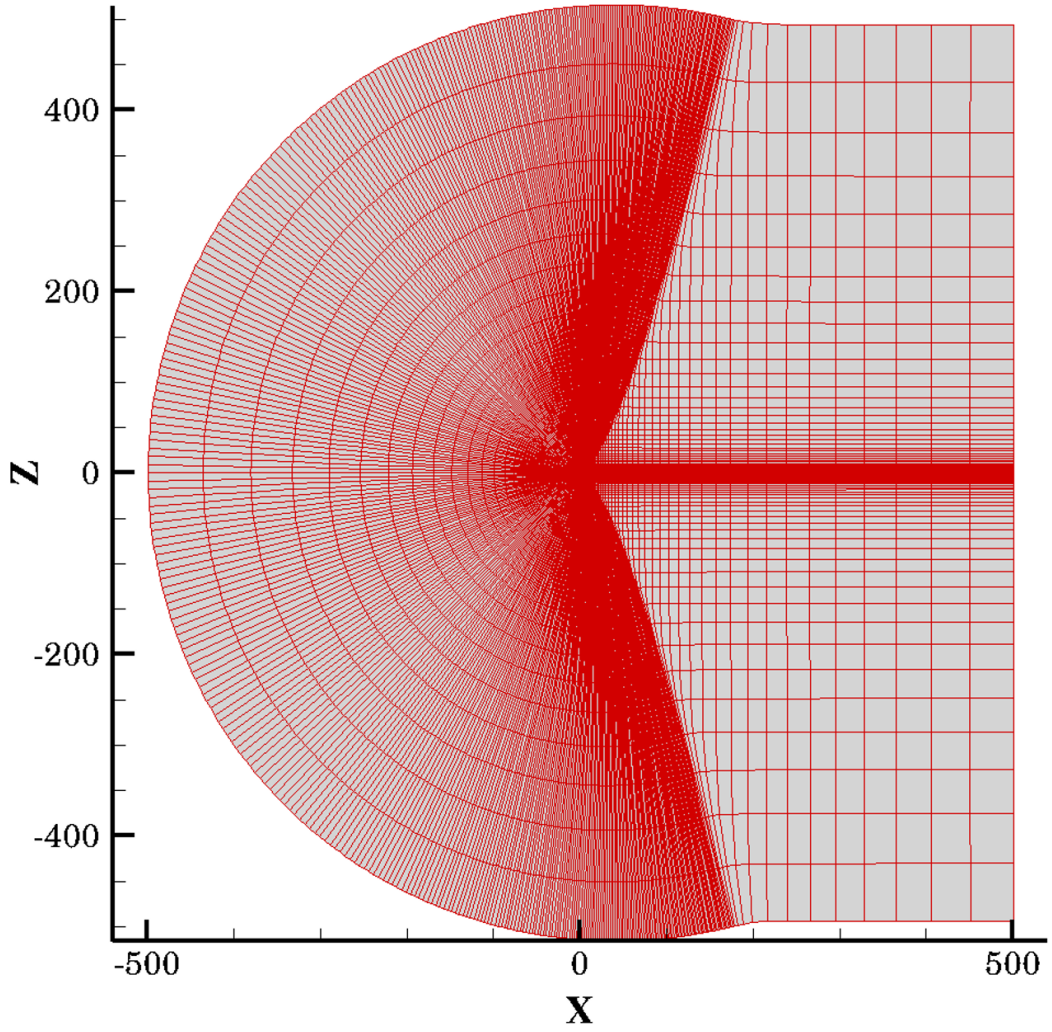

Figure 5.3: Computational domain of a 449 × 129 grid for NACA 0012 airfoil

the wake region (from the trailing edge to the outflow region). For the finest grid, the minimum normal wall spacing is 10^{-7}. The aspect ratio at the leading edge $AR_{LE} = 125$ for the spacing at the trailing edge for all the grids. Since the spacing at the trailing edge is of more importance for this experiment, the aspect ratio for this region is ten times larger than that of the leading edge.

The trailing edge spacing in the middle of the airfoil (mid-chord) $x \approx 0.5$ is $0.00123c$ and the aspect ratio which corresponds to this is $12,300$. It is to be noticed that the aspect ratio of the mid-chord is found to be approximately two orders of magnitude higher than the aspect ratio of the trailing edge.

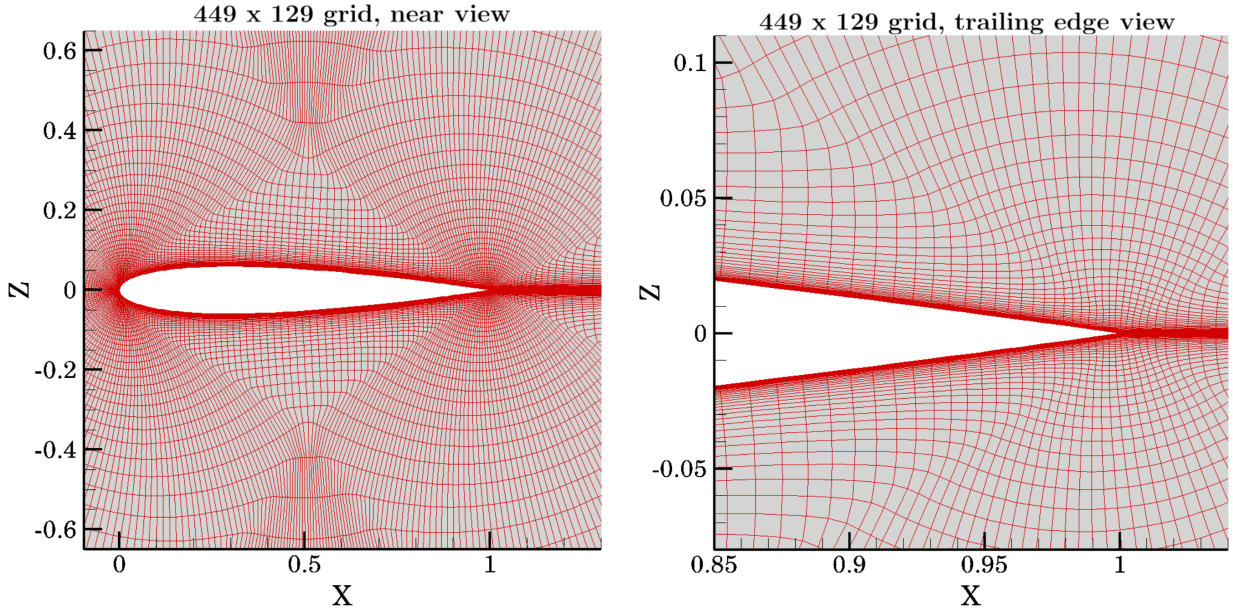

(a) Near view.

(b) Near view trailing edge.

Figure 5.4: Near view of the airfoil and the trailing edge

5.3 3D Modified Bump-in-channel

The aim of this study is mainly focused on the verification and validation of RANS solvers consisting of the SA turbulence model for the flow around the $3D$ bump profile to achieve accurate solutions that can be served as a reference for pertinent $3D$ configurations. A sequence of nested grids ranging from coarse to fine meshes of the same family is considered for this study.

Geometry and Boundary Conditions

The investigated test case is formulated as **"3D Modified Bump"** under the **"Cases and Grids for Turbulence Model Numerical Analysis"** at the TMR website [1]. The $2D$ bump in channel differs from the $2D$ finite plate configuration in that there is a bump (curvature) in the viscous wall region that leads to the development of pressure gradients. The $3D$ Modified Bump-in-channel is a three-dimensional interpretation of the $2D$ model defined in the **"2D Bump-in-channel"** under the **"Turbulence Model Verification Cases and Grids"** section of the TMR website.

The $2D$ bump profile from which the $3D$ bump configuration is developed is defined by the following:

$$\begin{cases} z = 0.05\left(\sin\left(\frac{\pi x}{0.9} - \frac{\pi}{3}\right)\right)^4, & 0.3 \leq x \leq 1.2, \\ z = 0, & 0 \leq x < 0.3 \quad \text{and} \quad 1.2 < x \leq 1.5. \end{cases} \tag{5.2}$$

The streamwise and the normal (vertical) direction of flow is indicated by the x-axis and z-axes respectively. The body reference area according to the evaluation is 1.5 units. The solid wall lies on the lower half of the geometry and the bump in general lies in the region $0 \leq x \leq 1.5$ (the actual location of the bump for $z > 0$ is at $0.3 < x < 1.2$, along the computational domain starting at $y = 0$ and running along the downstream direction at $y = -1$. The maximum height of the bump is $max(z) = 0.05$. This variation of the bump along the spanwise (y axis) direction is given by:

$$x = x_0 + 0.3(\sin(\pi y))^4, \quad -1 \leq y \leq 0, \tag{5.3}$$

where x_0 is the x-location of the bump at given point on the $2D$ configuration.

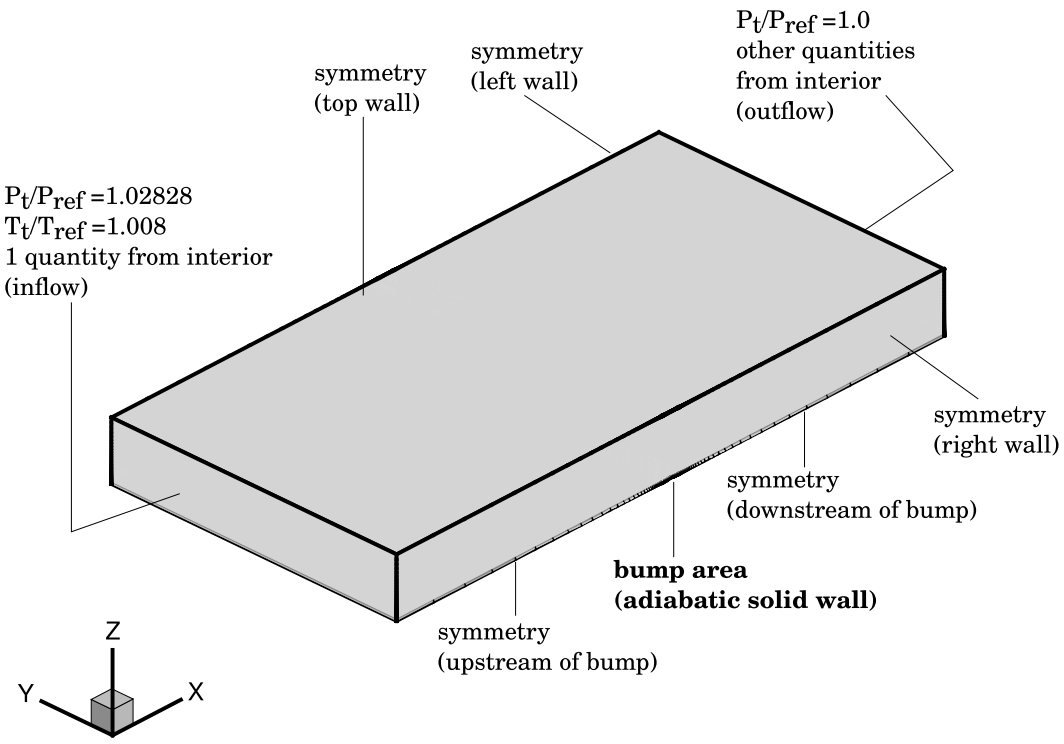

Figure 5.5: Domain and boundary conditions of $3D$ bump.

The following are the boundary conditions: The viscous solid-wall with adiabatic no-slip conditions are defined on the surface of the bump. The upstream is set to start at $x = -25$ units and downstream is located at $x = 26.5$ units. At $z = 0$, from the upstream to the leading edge of the bump ($-25 < x < 0.3(\sin(\pi y))^4$) and from the trailing edge following the downstream ($1.5 + 0.3\ (\sin(\pi y))^4 < x < 26.5$) are adjacent to the wall on the lower boundary is set to symmetry plane boundary. This is the region between the far-field and the solid wall. The top plane at $z = 5.0$ and, left and right walls that bound the computational domain at $y = 0$ and $y = -1$ are taken as symmetry planes. At the upstream boundary, there is the prescribed total pressure and total temperature conditions that complies with $P_t/P_{ref} = 1.02828$, $T_t/T_{ref} = 1.008$, whereas at the downstream boundary constant pressure conditions are given by $P/P_{ref} = 1$.

Flow conditions

A subsonic turbulent compressible flow was run at $M_{ref} = 0.2$ with the Reynolds number ($Re_L = 3\ million, (L = 1)$) calculated based on unit length of the grid. The reference temperature is $T_{ref} = 540°$ Rankine. The far-field inflow turbulent flow variable for the SA model is $\tilde{\nu}_{farfield} = 3\nu_\infty$. The Prandtl number is assumed to be a constant at $Pr = 0.72$, and the turbulent Prandtl number is assumed the constant $Pr_t = 0.9$. From the Sutherland's Law, molecular viscosity for the flow is calculated (Ref. Eq. 3.9).

Computational mesh

A family of six structured grids with the uniform mesh refinement $3D$ hexahedral grids has been considered for the experiment. A *Fortran90* program available at the TMR website [1] is modified to generate $3D$ profiles from $2D$ configurations. The family of grids ranging from the

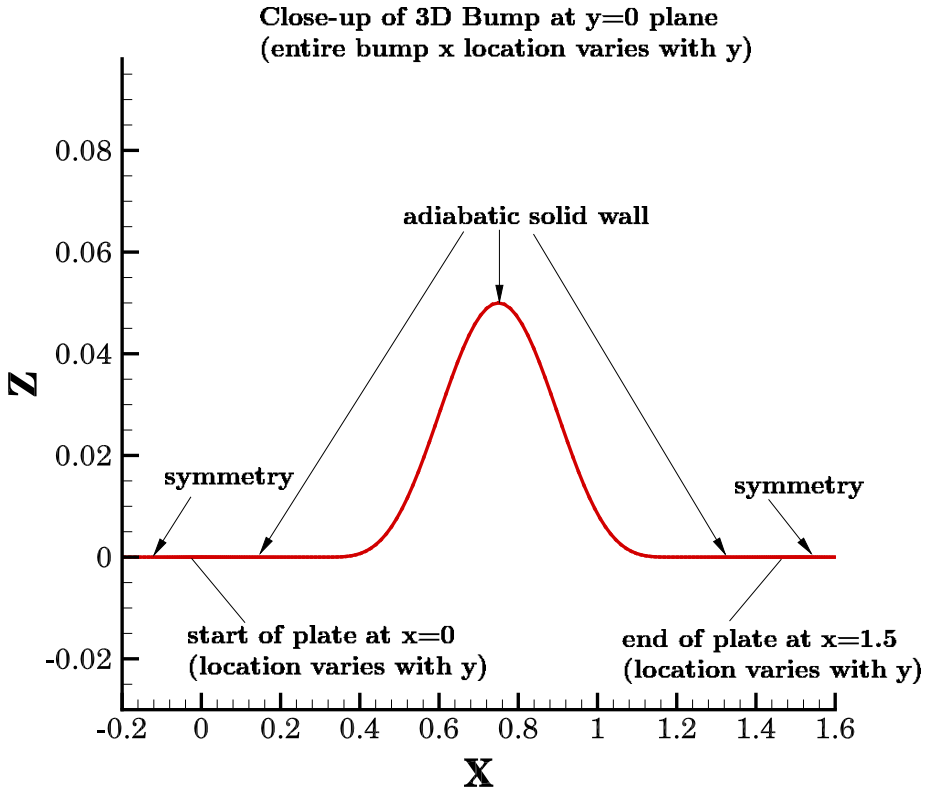

Figure 5.6: Near view of 3*D* bump.

Grid	Family 1 (hex)	
	Cells	Nodes
L1	14,417,920	14,709,825
L2	1,802,240	1,875,489
L3	225,280	243,729
L4	28,160	32,841

Table 5.3: Statistics of four finest grids for 3*D* Modified bump grid family

finest grid ($65 \times 1409 \times 641$) to the coarsest grid ($3 \times 45 \times 21$) is obtained by recursive generation of a coarser grid which is every-other grid plane of the next finer grid in all the dimensions. These numbers on the grid are the nodes that lie on the spanwise, streamwise and normal directions respectively. Table 5.3 provides a summary of the grid elements. The minimum possible wall-spacing of the finest grid is $z = 5.0 \times 10^{-7}$, which allows for the approximate average over the surface of the bump as $z^+ = 0.06$. In the case of the coarsest grid, the wall-normal spacing is acceptably fine to an extent that leads to an approximate average along the surface of the bump as $z^+ = 2.0$. There is the observable stretching in the wall-normal direction concentrating at the leading and trailing edges. Uniform spacing is applied in the spanwise direction.

5.4 3D Hemisphere Cylinder Validation Case

The study intends to perform numerical simulations and to provide reference solutions for the flow around a smooth body of revolution, which in this case is a 3*D* hemisphere-cylinder configuration. The obtained results are validated against the existing reference solutions evaluated by FUN3D, USM3D, SFE, and CFL3D on a sequence of grids for RANS solvers. This study provides a basis for the experimental and comparative study for the SA turbulence model.

Geometry and Boundary Conditions

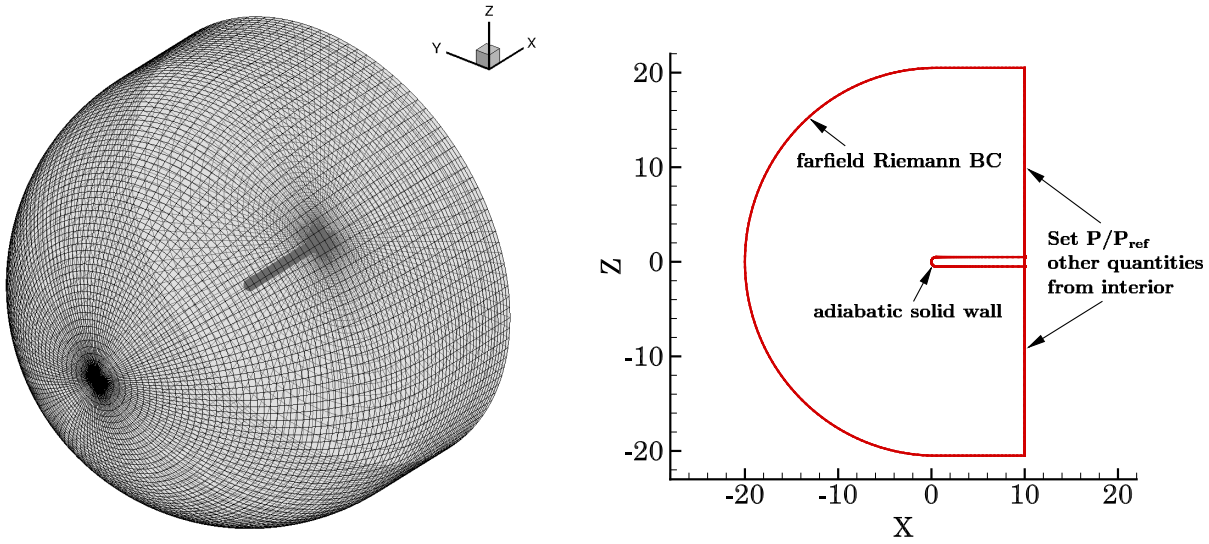

(a) Structured volume grid.

(b) Structured grid domain.

Figure 5.7: 3*D* hemisphere-cylinder volume configuration and boundary conditions

The geometry for the experimental study is taken from the report of Tsieh [23] and different other cases of the hemisphere cylinder are mentioned in [24]. The test case is described as **"3D Hemisphere Cylinder Validation Case (NEW)"** under the **"Cases and Grids for Turbulence Model Numerical Analysis"** section of the TMR website [1]. This is an updated version of the earlier study which corresponds to "3D Hemisphere Cylinder (old)" under the same section. In the provided experimental setup the diameter of the cylinder was 1 *in* and its body length was 10 *in*, with the Reynolds number per foot as 4.2 *million*. When the computational domain is considered, the unit length is taken as 1 *in* and the rest of the values are calculated accordingly. The diameter of the cylinder is 1 and the cylinder body length is 10 with the Reynolds number $Re = 0.35$ *million* per unit length. The apex of the cylinder marks the origin of the coordinate system. The streamwise direction is given by the positive x-axis which is in line with the axis of the geometry (hemisphere and cylinder).

The following are the boundary conditions: The back of the cylinder at $x = 10$ is the downstream boundary of the computational domain. The exit-pressure outflow conditions of the aforementioned region corresponds to constant pressure boundary conditions given by $P/P_{ref} = 1$. The far-field resembles an hemisphere with its center at $x = 10$, $y = 0$, $z = 0$, is set as Far-field Riemann boundary with 100 *units* as its radius.

Flow conditions

Considering the geometry conditions for the computational grid, the reference solutions have been determined for the following flow conditions: the reference Mach number $M_{ref} = 0.6$, and

the reference temperature $T_{ref} = 540°$ Rankine. The experiment has been conducted for various angles of attack of 0° , 5°, 10°, 15°, and 19°.The farfield inflow turbulent flow variable for the SA model is $\tilde{\nu}_{farfield} = 3\nu_\infty$. The Prandtl number is assumed to be a constant at $Pr = 0.72$, and the turbulent Prandtl number is assumed the constant $Pr_t = 0.9$. From the Sutherland's Law, molecular viscosity for the flow is calculated (Ref. Eqn. 3.9).

Computational mesh

Grid	Family 1 (hex)		Family 2 (tet)	
	Cells	Nodes	Cells	Nodes
L1	11,796,480	11,837,729	45,416,448	7,625,153
L2	1,474,560	1,484,945	5,677,056	960,225
L3	184,320	186,953	709,632	121,841
L4	23,040	23,717		

Table 5.4: Statistics of four finest grids for 3D Hemisphere cylinder grid families

Grids are obtained from two families consisting of both structured and unstructured grids. Both the families are obtained from Fortran codes available at the TMR website that generates corresponding grids. Table 5.4 provides a summary of both the structured and unstructured grid elements.

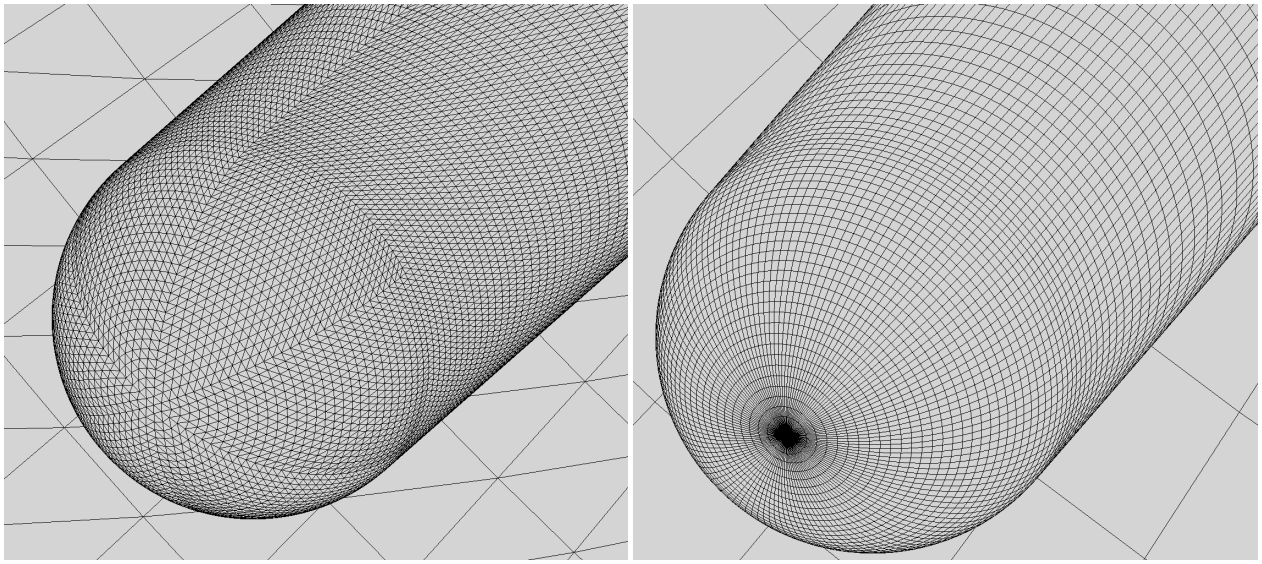

(a) Unstructured surface grid. (b) Structured surface grid.

Figure 5.8: 3D hemisphere-cylinder configuration grids

- **Unstructured grids:** A family of three nested computational grids is considered for the experiment [25]. These grids are intended to avoid polar singularity and are therefore accordingly designed, meaning that during mesh refinement, the node-sharing cells and the aspect ratio that is given for the faces at the boundary, continue to remain constrained. The grids do not exhibit axisymmetry. However, they are periodic in terms of 60° rotation and reflection symmetric in terms of the planes that have the circumferential angles, that are computed in multiples of 30°. The specified circumferential angle is given as $\phi = \tan^{-1}\frac{z}{y}$. The finest 360° grid has 45,416,448 tetrahedral elements. The surface grid of the viscous boundary layer

(on the surface of the cylinder) consists of 221,184 surface triangles. The finest surface grid is shown in Fig. 5.8a. The mesh-wall spacing at this region is at $z^+ = 0.5$. Similarly, the medium grid consists of 5,677,056 tetrahedral elements with 55,296 surface triangles defining the surface of the hemisphere-cylinder. The coarse grid has 709,632 tetrahedral elements holding 13,824 surface triangles at the viscous surface.

- **Structured grids:** Four axisymmetric computational grids from the same family are taken for the numerical experiment. These grids exhibit polar singularity at the apex of the hemisphere, along the axis i.e., hexahedral cells can degenerate into prismatic cells along this particular axis. The 360° fine grid is made up of 11,796,480 elements with 73,728 prisms and 11,722,752 hexahedra. The surface configuration comprises of 512 surface triangles and 155,136 surface quadrilaterals. The recursive generation of the grids from the finest grid results in the coarser grid level, by the process of removing every-other grid plane in each of the three dimensions. Structured grids are generated with fewer elements than their unstructured grids counterpart. The near-surface mesh spacing for this structured grid is given as $z^+ = 0.8$. The surface of the structured grid is given in Fig. 5.8b.

5.5 3D ONERA M6 Wing Validation Case

The ONERA M6 has been extensively used for validation purposes of CFD solvers. After a series of design modifications dated back to 1977, the M6 profile for the TMR website [1] was developed by two groups from ONERA strictly for CFD computations [26]. Numerical simulations are performed on the OM6 wing configuration to validate the viscous flow simulations of early $3D$ cases and also to analyze the results of the turbulence models, to provide reference solutions.

Geometry and Boundary Conditions

The M6 wing for an attached case is considered for this purpose. The outline of the test case is provided in the "**3D ONERA M6 Wing Validation Case**" under the "**3D ONERA M6 Wing**" section of the TMR website [1]. A sharp trailing edge (closed) of the M6 geometry was designed using the Computer-Aided Design (CAD) model [26] [27] for this particular experimental study and this differs from the usual M6 by that the trailing edge which is slightly thick. These models are made available at the TMR website [1] for reference. Normalization of the grids is done to have the root chord as unity. The wing chordwise extension is specified to be 0.55 percent of the local chord. The moment centers of the x-, y- and z-axis are all specified at 0.0.

The boundary conditions are as follows: The far-field represents a hemisphere of a radius of 100 unit chords and is set as a Far-field Riemann boundary. Symmetry boundary conditions are set up for the plane on which the root airfoil is located. The complete boundary conditions for the M6 profile is shown in Fig. 5.9.

Flow conditions

The flow conditions are set up for a transonic flow around the M6 wing with freestream Mach number 0.84, Reynolds number per unit root chord 14.6 *million* and angle of attack of 3.06°. These conditions were set to avoid inefficient scatter of the CFD distributions [27]. The far-field inflow turbulent flow variable for the SA model is $\tilde{\nu}_{farfield} = 3\nu_\infty$. The Prandtl number is assumed to be a constant at $Pr = 0.72$, and the turbulent Prandtl number is assumed the constant $Pr_t = 0.9$. From the Sutherland's Law, molecular viscosity for the flow is calculated (Ref. Eq. 3.9).

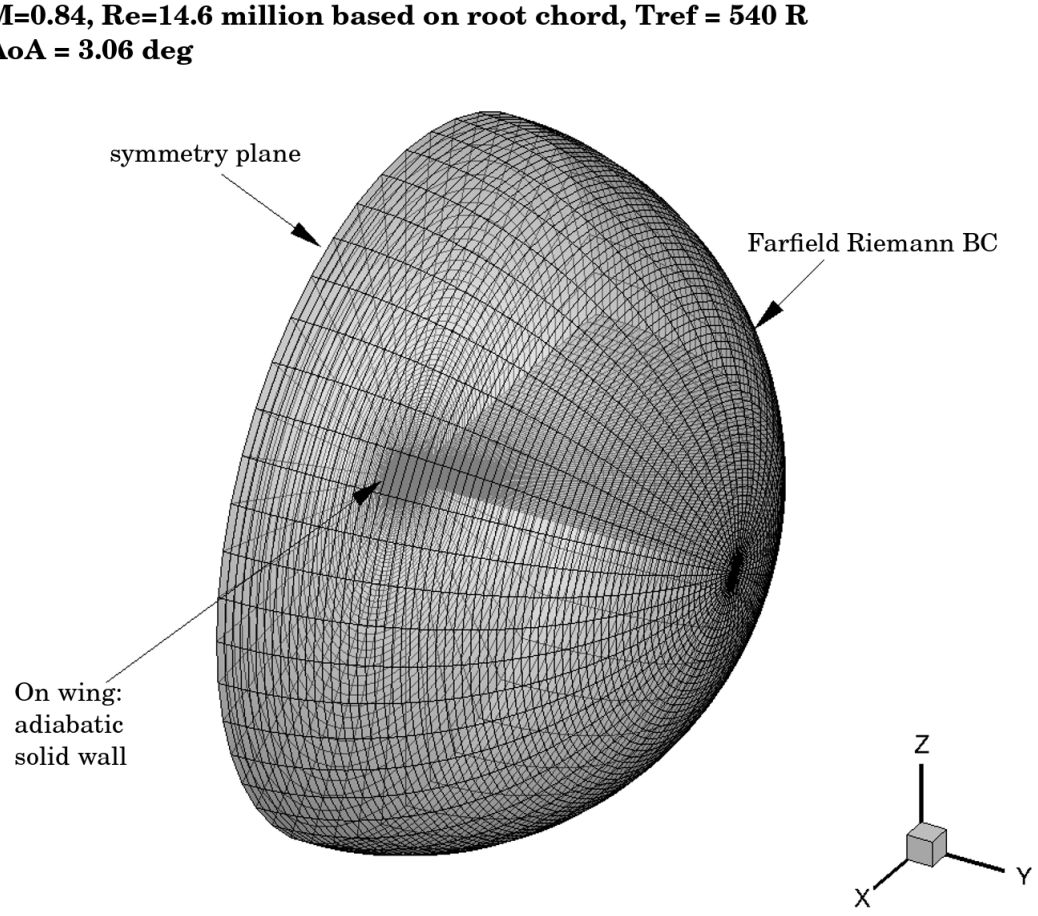

Figure 5.9: Domain and boundary conditions of 3*D* Onera M6 wing.

Grid	Family 1 (hex)	
	Cells	Nodes
L1	8,000,520	8,021,955
L2	4,345,200	4,357,796
L3	1,395,000	1,399,811
L4	122,880	124,865

Table 5.5: Statistics of four finest grids for 3*D* ONERA M6 grid family.

Computational mesh

A family of four nested computational grids is generated from the input files available at the TMR website [1] to range from fine to coarse meshes for this experiment [25]. Table 5.5 provides a summary of the grid elements. A *C-H* topology is used to build meshes around the wing, that are topologically similar to the hemisphere-cylinder test case. Therefore, the features available for the hemisphere-cylinder case is also applicable to the ONERA M6 configuration. Although there exists a distinctive feature of M6, which is its ability to regulate the stretching of the grid towards

the focus areas such as the leading and trailing edges. This stretching is done using a hyperbolic tangent function which can be modified in the input parameter.

Chapter 6

Results

The following chapter deals with the computed results that are discussed along with the benchmark reference solutions. Each of the existing results for the individual test cases is referenced accordingly throughout this chapter.

6.1 Case 1: 2D Finite Flat Plate

Turbulent flow through the surface of the finite plates has been studied. With the flow conditions as mentioned in Sec. 5.1, the following results are obtained. These results are validated against existing results [28] from solvers such as CFL3D, FUN3D, and TAU available at the TMR website [1].

Convergence studies

Results pertaining to the $2D$ Finite flat plate with respect to Sec. 5.1 are discussed in this section. Fig. 6.1 shows the convergence histories for density and turbulence residual versus multigrid cycle for the finest grid. A Full Approximation Scheme (FAS) with 3V-cycle [18] is used for the experiment. The coarsest grid (L4) takes about 573 cycles to converge to the density residual tolerance of 10^{-14} whereas the finest grid takes $7,574$ cycles to converge for the same tolerance. Each grid is computed with different CFL numbers and it is specified that for mesh refinement, the corresponding CFL number is to be reduced.

The main focus of the study is on the grid convergence study and this is vital to establish a grid-independent solution, whereby mesh refinement leads the spatial discretization errors to approach zero asymptotically which further means to point that by continuing to increase the fineness of meshes, the solution doesn't show significant improvement. For the finite flat plate test case, the convergence plot of the drag coefficient versus the grid spacing $h = \sqrt{1/N}$ (N represents the number of degrees of freedom) is shown in Fig. 6.2. To represent the drag coefficient a fine scale of 0.1 drag count is taken along the y-axis. The drag coefficient represents the first-order convergence in the finer grids for the extended leading and trailing edge of the plate with the aspect ratio close to one, $AR_{LE} = 1$. For solutions regarding other aspect ratio [29] can be referred.

The SA-neg model implemented in the TAU code agrees with the convergence quality from the other solvers [30]. The flow is completely turbulent over the flat plate with the formation of the boundary layer from the wall's surface. Complex phenomena such as separation are avoided, which led to the successful implementation of the turbulence model.

The drag convergence is investigated further on the surface of the flat plate consisting of three different sections: near the leading edge, the middle section and near the trailing edge of the plate and the regions are given by [29, p. 30]:

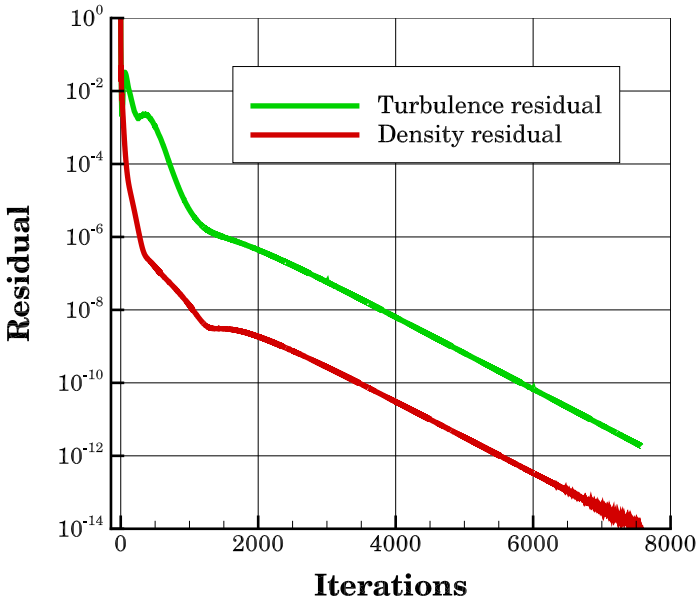

Figure 6.1: Residual convergence for the finest grid for 2D Finite flat plate.

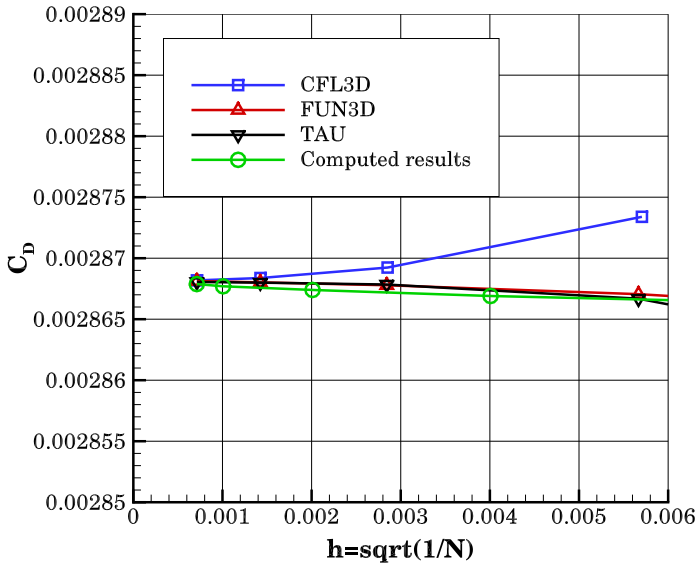

Figure 6.2: Drag coefficient convergence of finite flat plate.

- Leading edge : $0 \leq x \leq 0.107267441655523$
- Middle section : $0.107267441655523 \leq x \leq 1.89273255834448$
- Trailing edge : $1.89273255834448 \leq x \leq 2$

Fig. 6.3 shows the drag convergence in the three regions that are mentioned. The middle region of the plate has a higher-order drag convergence. In Fig. 6.3a it can be seen that the computed results show slight variation with the experimental results. This can be due to the reason that the meshes by itself differ from the ones considered for the simulation for CFL3D, FUN3D, and

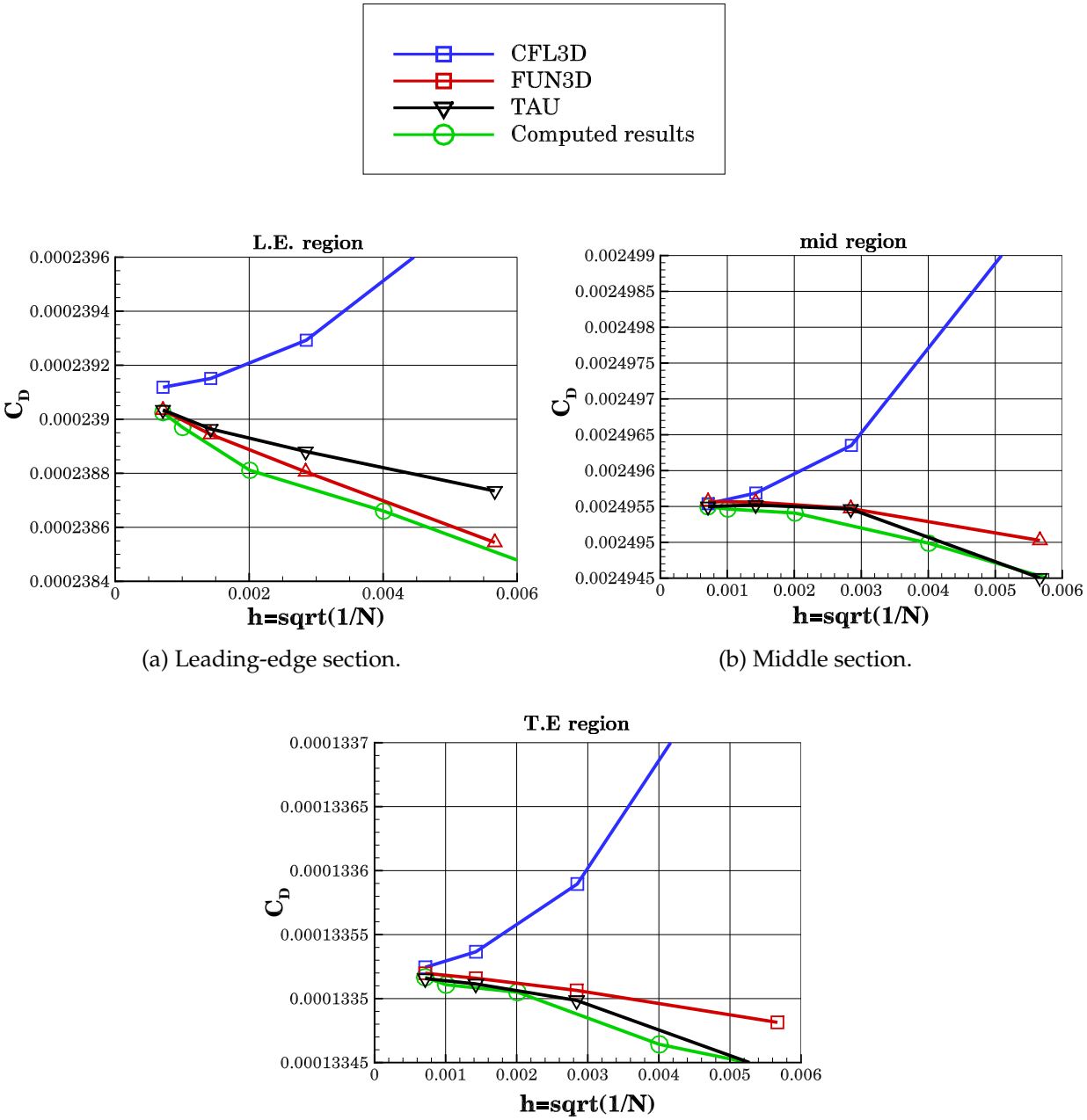

(a) Leading-edge section.

(b) Middle section.

(c) Trailing-edge section.

Figure 6.3: Grid convergence of drag within different sections of the flat plate.

TAU. The meshes considered for the thesis despite being generated from the TMR website differ in terms of grid spacing h. For all the three regions, although drag convergence occurs when moving along to finer meshes, with the coarser meshes there seems to be a noticeable difference.

Skin friction and surface pressure

The skin friction coefficient is studied at a specified location at $x = 0.8697742$ in two ways. Fig. 6.4a represents the variation of skin friction that is plotted against the function of h. In Fig. 6.4b where the skin friction is plotted against h^2 it is observed that all the codes converge relatively linear thereby leading to the inference that the convergence is more likely of second-order than first order.

Skin friction coefficient along the leading edge is shown in Fig. 6.5a and along the trailing edge is shown in Fig. 6.5b. The four grid levels that are shown here range from the finest 'grid level 1' (2,561 × 769) to coarsest 'grid level 4' (321 × 97), with further details of the mesh available in Table 5.1.

It is seen from the results that the discretization error continues to reduce quite slowly as the meshes are refined. The order of grid convergence is very close to 2 for these finest meshes.

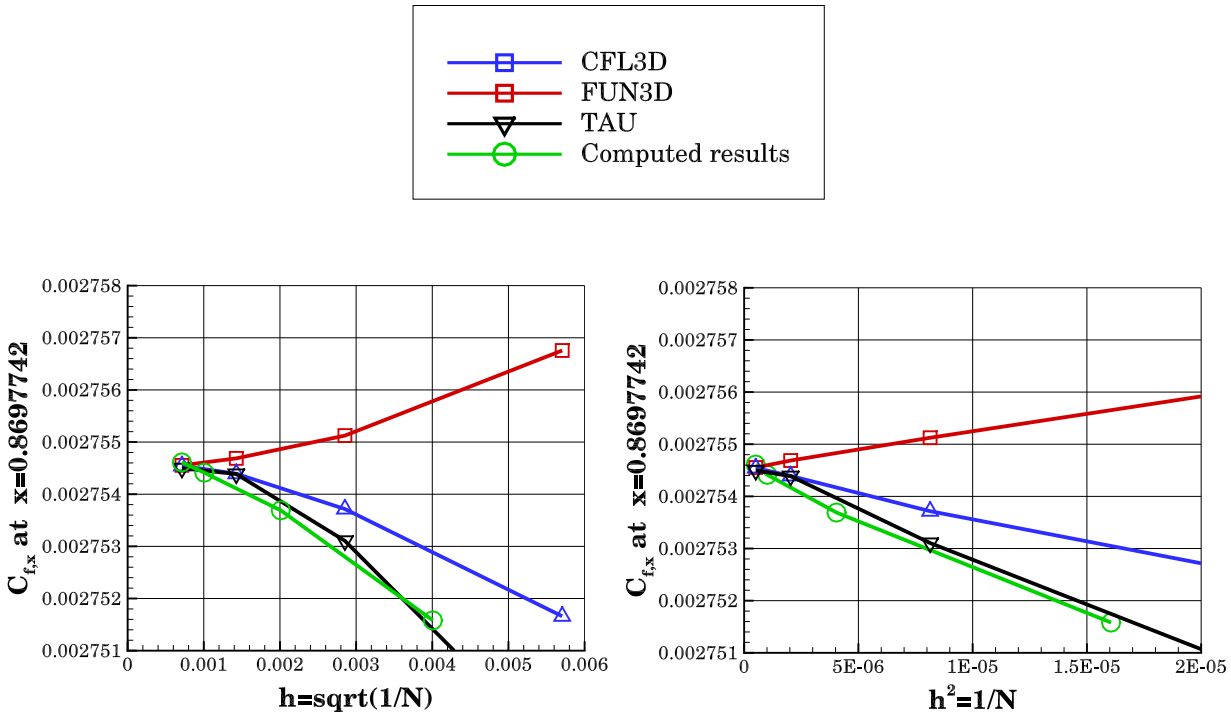

(a) Function of h.

(b) Function of h^2.

Figure 6.4: Skin friction convergence of the flat plate at $x = 0.8697742$.

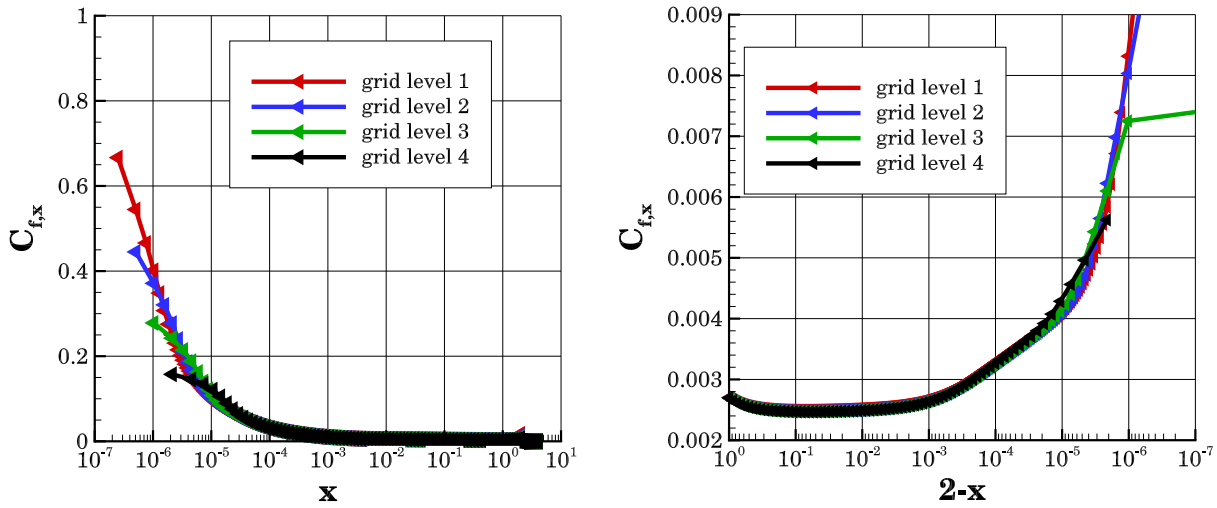

(a) Leading edge region.

(b) Trailing edge region.

Figure 6.5: Skin friction convergence on four finest grid levels of the flat plate.

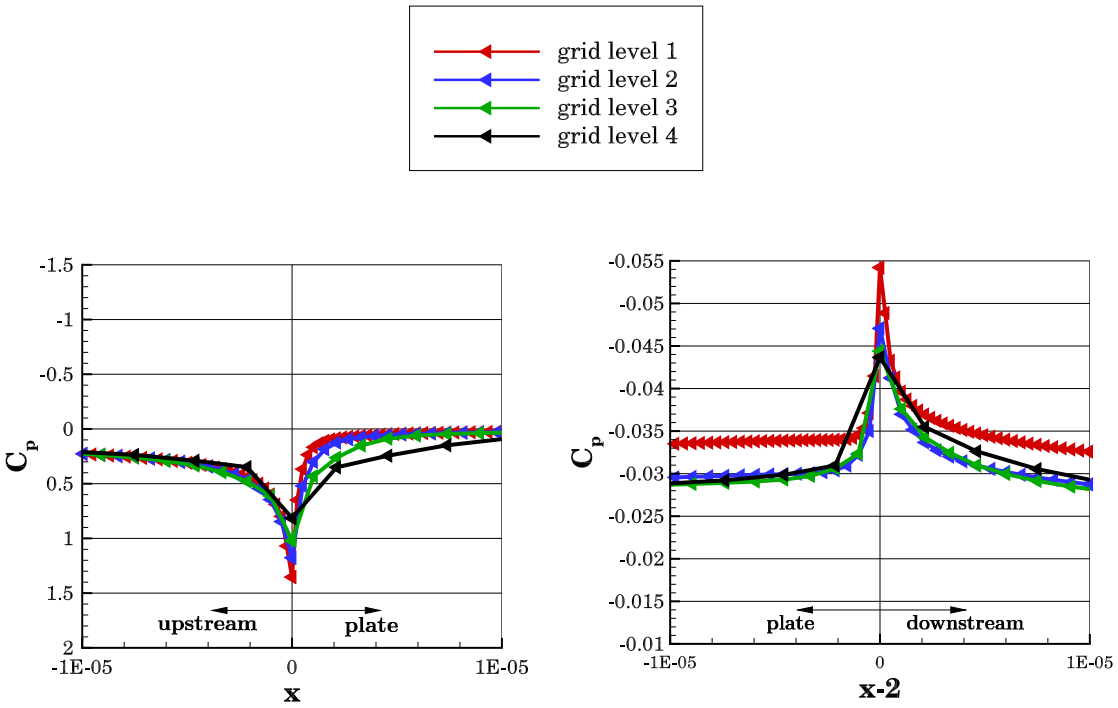

(a) Near leading edge.

(b) Near trailing edge.

Figure 6.6: Surface pressure coefficient on four grid levels.

The variation of skin friction near the trailing-edge region is shown in Fig. 6.5b. With $AR_{LE} = 1$, it is evident that the four grid points exhibit large errors when nearing the trailing edge. Although an in-depth analysis of the grid convergence at the trailing edge is not conducted, discretization errors were low and grid convergence is acceptable to some extent.

The pressure coefficient C_p convergence near the leading and the trailing edge as shown in Fig. 6.6. The pressure is observed to be discontinuous at both the leading and the trailing edges considering a tangential line along the surface of the plate, although a smooth variation of the pressure coefficient takes place in these regions. Convergence occurs slowly at regions near the edges when compared with the regions that are relatively far from the edges.

6.2 Case 2: 2D NACA0012 Airfoil

Convergence studies

Results are shown for the 2D NACA 0012 airfoil case with respect to the flow conditions that are discussed in Sec. 5.2. Fig. 6.7 shows the iterative convergence histories for density and turbulence residual versus multigrid cycle for the finest mesh with $AoA = 10°$. A Full Approximation Scheme (FAS) with 2V-cycle [18] is used for the experiment. The coarsest grid (L4) takes about $1,578$ cycles to converge to the density residual tolerance of 10^{-13}. Each grid is computed with different CFL numbers and it is specified that for mesh refinement, the corresponding CFL number is to be reduced. The convergence histories for the other AoA of the finest grid is found to be similar to the one shown in Fig. 6.7.

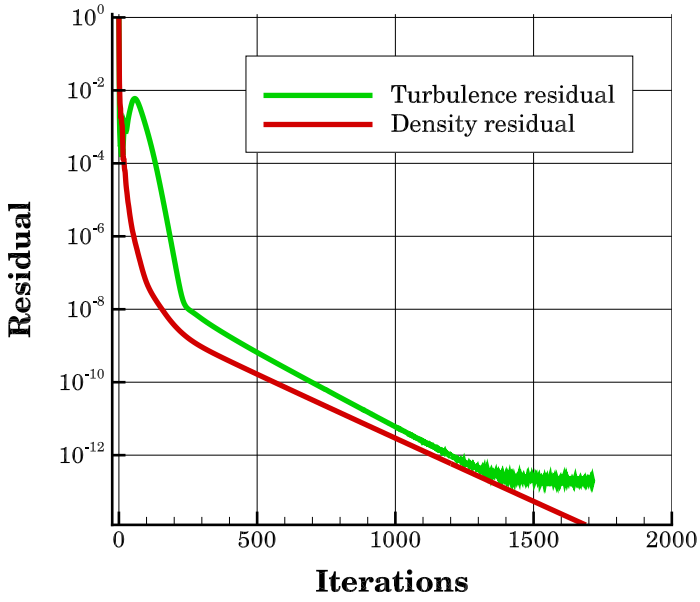

Figure 6.7: Residual convergence for the L4 grid at $AoA = 10°$ for $2D$ NACA 0012 airfoil.

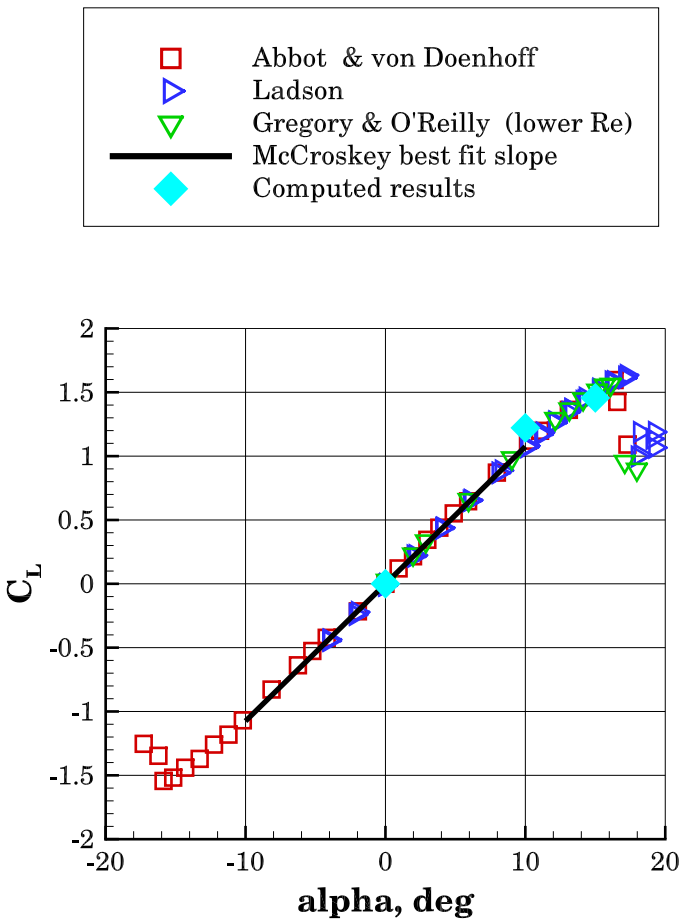

Figure 6.8: NACA 0012 experimental C_L vs alpha.

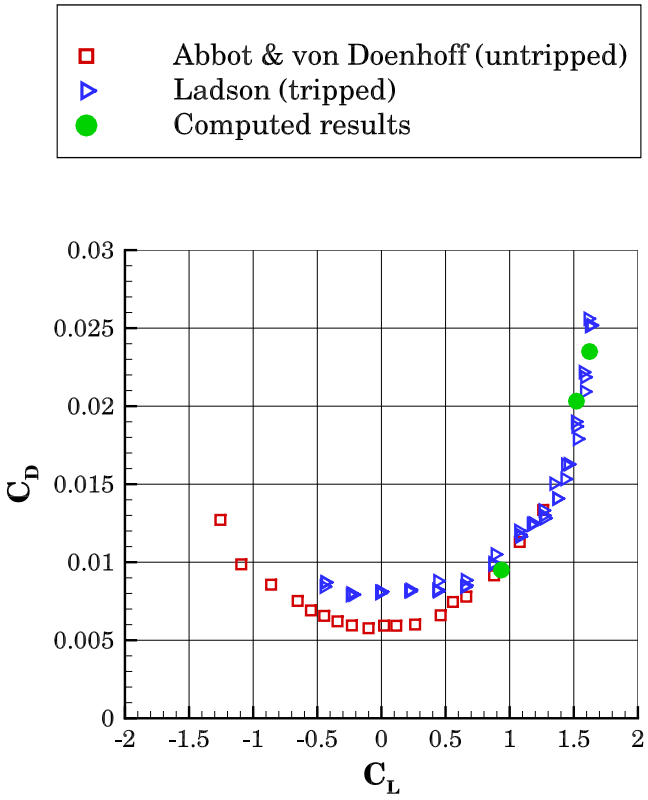

Figure 6.9: NACA 0012 experimental C_L vs C_D.

Aerodynamic coefficients

The NACA 0012 airfoil validation case mainly focuses on the following four characteristics [1] that is obtained by the numerical computation of a family of seven grids,

- Lift coefficient (C_L) versus AoA (α),
- Drag coefficient (C_D) versus C_L,
- Surface pressure coefficient (C_p) versus x/c (for $\alpha = 0, 10, 15$) and
- Surface skin friction coefficient (C_f) versus x/c (for $\alpha = 0, 10, 15$).

The computed results are held in comparison against other experimental results from the TMR [1] website, although there exists difficulty when dealing with $2D$ cases at higher angles of attack approaching stall.

The numerical simulations for the incompressible flow condition of the fluid at $Re = 6$ *million* are shown in this section. As the angle of attack increases beyond a certain point, the lift begins to decrease. This condition is referred to as *stall* and the effect of this condition is seen in Fig. 6.8. Various reference data are held in comparison against the computed simulations and these include results from McCrosky [31], where the data are obtained by tripping the boundary layer; untripped data from Abbott and von Doenhoff [32] along with Gregory and O'Reilly's data [33] that has been tripped but with a low $Re = 3$ *million*; and that of Ladson [34] that was deemed more suitable for the CFD simulations for $Re = 6$ *million*. The differences that are exhibited by all the methods under consideration are all visualized in the region of the stall of Fig. 6.8.

The significant difference between different Reynolds number is not seen in the lift data. But with Fig. 6.9, the influence of Re can been seen with the drag data. The computed results for both the lift and drag coefficients seem to be fitting with the experimental data.

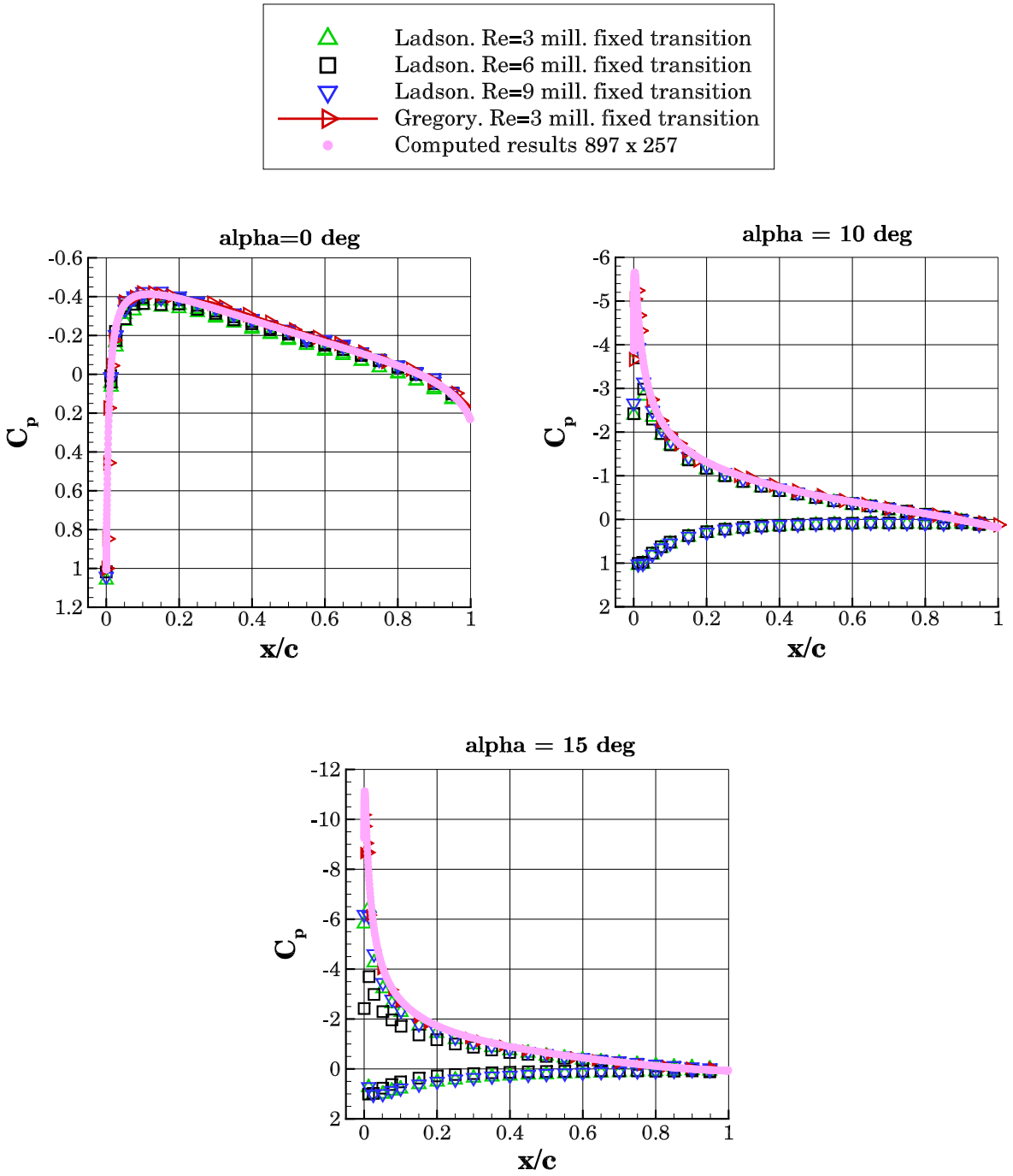

Figure 6.10: Surface pressure distribution over the airfoil at different angles of attack.

Surface pressure and skin friction

For comparing the computed results of the surface pressure coefficient, the well-resolved Gregory and O'Reilly data [33] is considered. Also, data from Ladson [34] that, from Fig. 6.10 show that the upper surface pressure for the leading edge is not well resolved when compared with other results. The surface pressure coefficient for the grid size of 897×257 for $\alpha = 0°$, $10°$, $15°$ that are consistent with the solution from other results. From Fig. 6.10 shows that the maximum surface pressure occurs near the leading edge. The computed results are more compliant with the results from Gregory and hence it can be more suitable for validation of CFD when focusing on

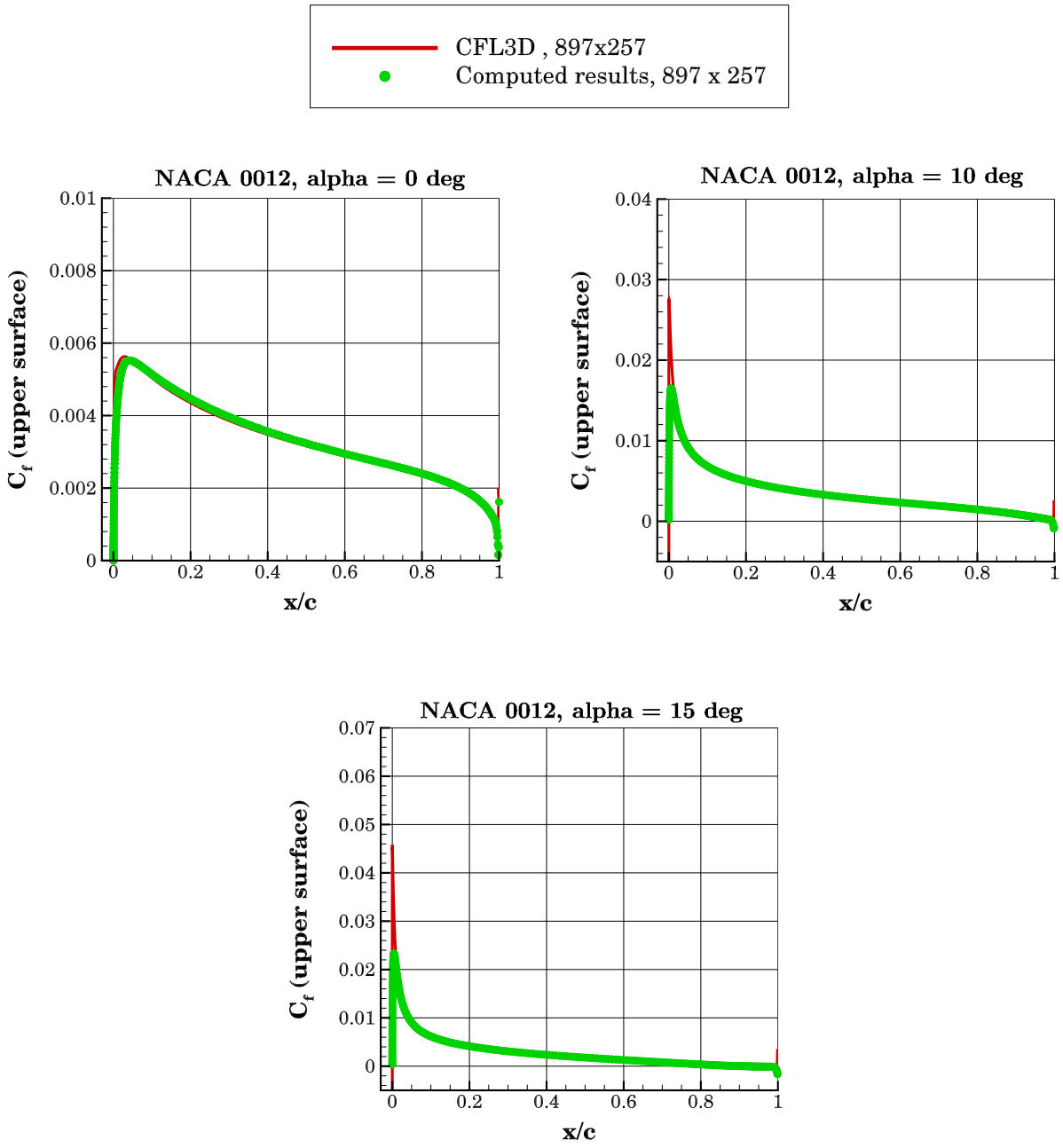

Figure 6.11: Skin friction variation over the airfoil at different angles of attack.

surface pressure. An extensive study for the skin pressure and skin friction coefficients can be found in [35] and [29].

The skin friction coefficient for the three angles of attack is shown in Fig. 6.11. The reference results obtained from the TMR website [1] exhibit point vortex far-field correction in regions near the trailing edge because these regions possess high numerical errors. This can be an explanation of the discrepancies among the computed results and the CFL3D results. However, the notable differences are seen in cases with increasing angle of attack and in this thesis, simulations with 10° and 15°.

6.3 Case 3: 3D Modified Bump

Convergence studies

Results are shown for the 3*D* modified bump-in-channel case with the flow conditions are discussed in Sec. 5.3. Fig. 6.12 shows the iterative convergence histories for density and turbulence residual versus multigrid cycle for the mesh size $17 \times 353 \times 161$. A Full Approximation Scheme (FAS) with 2V-cycle [18] is used for the experiment. The coarsest grid (L4) takes about 7,570 cycles to converge to the density residual tolerance of 10^{-12} whereas the finer grids take 43,882 cycles to the residual tolerance of 10^{-13}. Each grid is computed with different CFL numbers and it is specified that with mesh refinement the CFL number is reduced.

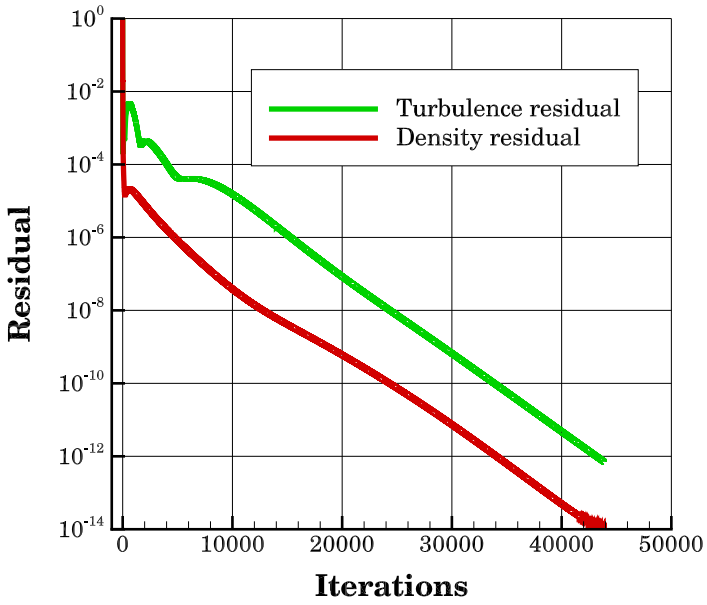

Figure 6.12: Residual convergence for mesh: $17 \times 353 \times 161$ for 3*D* bump.

Reference results for the 3*D* bump flow are taken from the TMR website [1]. However, it is observed in FUN3D solutions that there exists an odd-even decoupling on finer grids through unweighted least-square gradients for inviscid fluxes [36]. Initial studies about this instability show that the decoupling is related to the degradation of gradients on the bump surface close to the inflection point [36].

The grid convergence of total drag and lift coefficients are shown in Fig. 6.13. The characteristic mesh size h that is evaluated as $h = N^{-1/3}$ is plotted against the drag coefficient in Fig. 6.13a and against the lift coefficient in Fig. 6.13b. Also, grid convergence of pressure drag and viscous drag are shown in Fig. 6.14. It can be observed from the results that all coefficients are seen converging to the same limit with mesh refinement. However, with the coarser grids, there are deviations from the reference results and this can be due to the differences in mesh sizes obtained and generated from the TMR website [1]. Fig. 6.14b shows that viscous drag comprises of 80% of the total drag that is seen in Fig. 6.13a. There is a sharp decrease of pressure drag with mesh refinement and this could be the reason for the total drag to vary in its grid-to-grid convergence because the viscous drag shows steady convergence with increasing finer grids. The total drag convergence of USM3D has an order of convergence that is higher than second, FUN3D slightly higher than first and CFL3D has its direction changed on the finest grid.

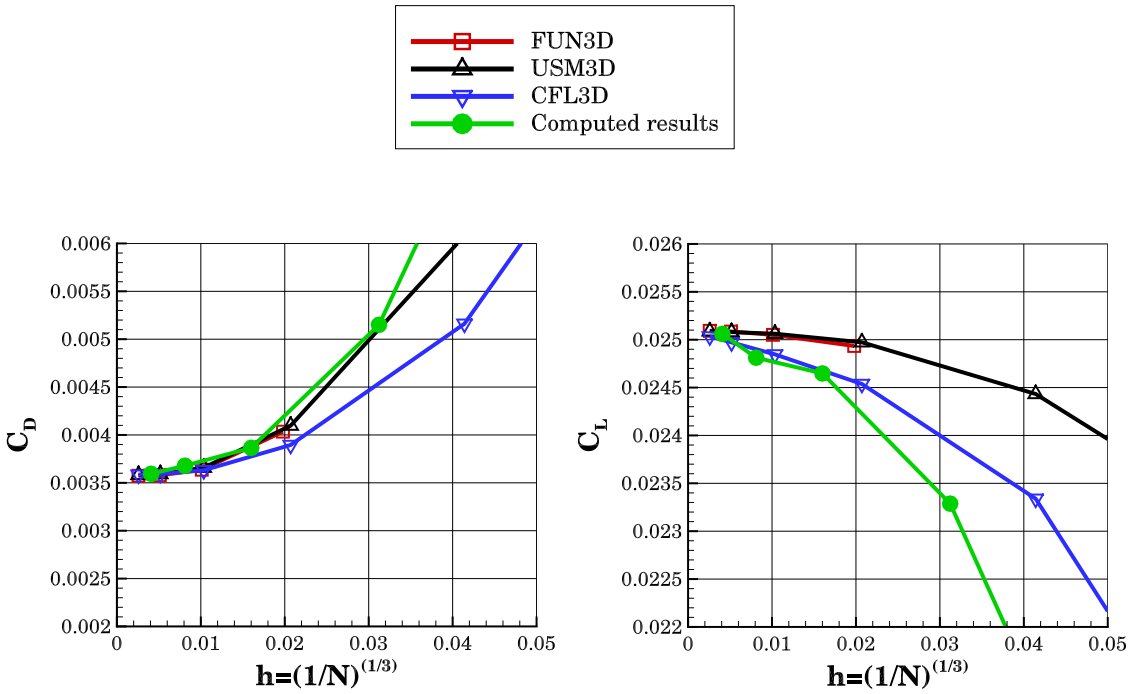

(a) Grid convergence of drag. (b) Grid convergence of lift.

Figure 6.13: Grid convergence behavior of forces for 3*D* bump.

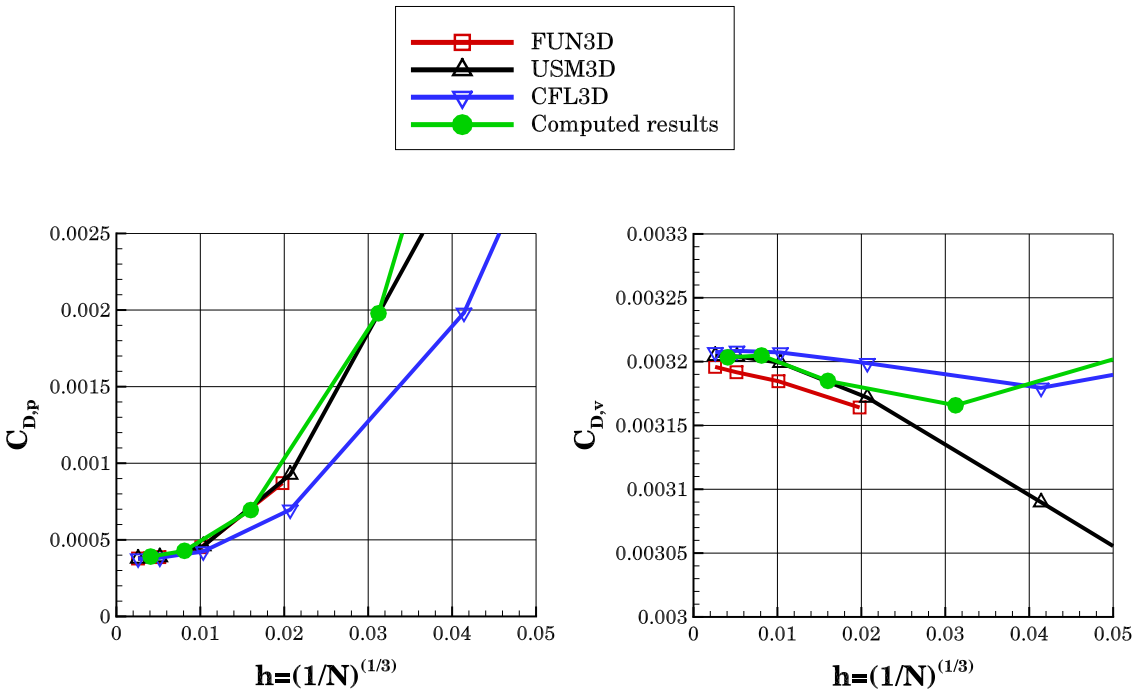

(a) Pressure drag. (b) Viscous drag.

Figure 6.14: Contributions to drag coefficient due to pressure and viscosity in a 3*D* bump.

The computed results for the total drag coefficient has an order slightly higher than first resembling that of FUN3D. The lift coefficient as shown in Fig. 6.13b is seen to monotonically increase with mesh refinement and the convergence here is of an order higher than first.

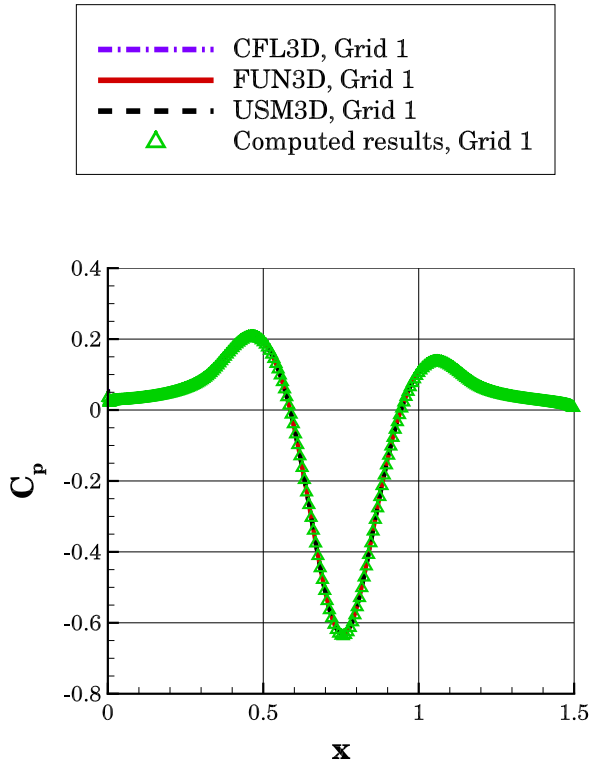

Figure 6.15: Overall pressure coefficient distribution (axially, along the body $y = 0$) on the finest grid for 3D bump. Global view.

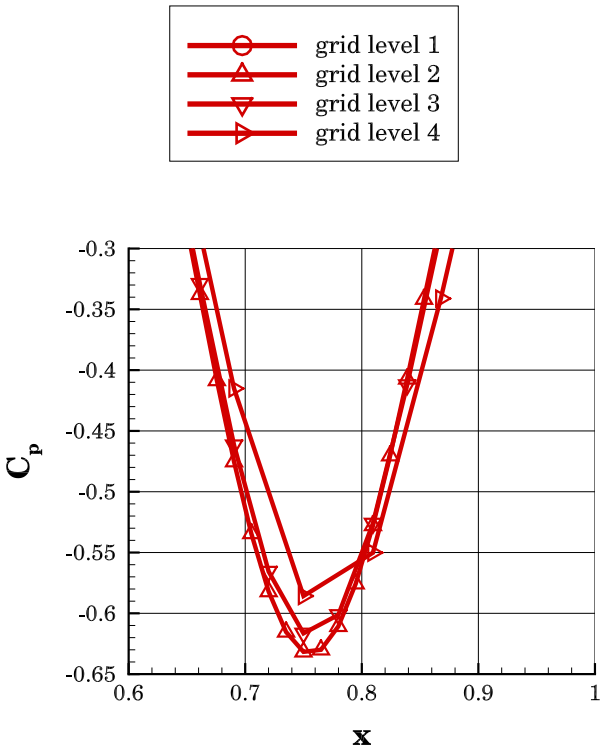

Figure 6.16: Near view of pressure coefficient distribution (axially, along the body $y = 0$) for 3D bump.

Surface pressure distribution

Fig. 6.15 shows the global view of the surface pressure coefficient along the center-line of the viscous wall surface, $y = 0$. Reference and computed results only for the finest grid are shown. The agreement between the CFL3D, FUN3D, and USM3D with the results obtained from the experiment through the TAU code are in satisfying agreement i.e solution between the codes is nearly indistinguishable.

Near views of the four finest grids for the center-line pressure variation are shown in Fig. 6.16. The solutions from the coarser to the finer meshes are analogous to each other in terms of their pressure coefficient. This leads to the inference that, in this particular RANS formulation setup with particular flow conditions, attention should be directed at the mesh refinement of grids rather than the discretization procedure.

6.4 Case 4: 3D Hemsiphere Cylinder

Convergence studies

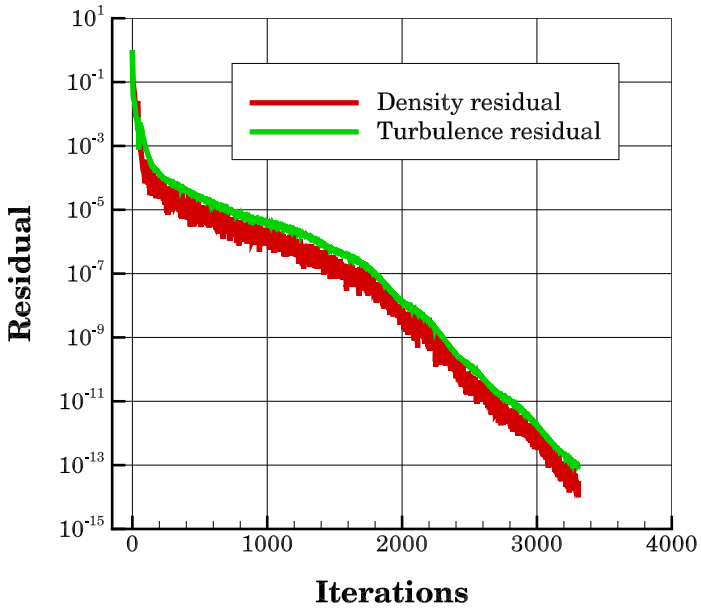

Figure 6.17: Residual convergence for the finest grid at $AoA = 19°$ for $3D$ Hemisphere cylinder.

Results are shown for the $3D$ hemisphere cylinder case with the flow conditions are discussed in Sec. 5.4. Fig. 6.17 shows the iterative convergence histories for density and turbulence residual versus multigrid cycle for the finest mesh with $AoA = 19°$. A Full Approximation Scheme (FAS) with sg-cycle [18] is used for the experiment. The coarsest grid (L4) takes about 157 cycles to converge to the density residual tolerance of 10^{-13} whereas the finest grid takes $3,358$ cycles to converge to the residual tolerance of 10^{-14}. Each grid is computed with different CFL numbers and it is specified that for mesh refinement, the corresponding CFL number is to be reduced. The convergence histories for the other AoA of the finest grid is found to be similar to the one shown in Fig. 6.17.

Grid convergence of drag and lift for various angles of attack are shown in Fig. 6.18 and 6.19. The drag coefficient is plotted against the characteristic mesh size h and is given as $h = N^{-1/3}$ in Fig. 6.18. It can be observed that all the drag components seem to converge to the same limit with

mesh refinement. FUN3D and USM3D solutions for unstructured grids are closer to each other than the CFL3D results for the structured grids. However, it has been studied that for the finest grids the difference in total drag coefficients is found to be lesser than 2 drag counts (less than 2%) [36]. The computed results for the structured meshes are seen to resemble the results of the structured codes of CLF3D and USM3D and it varies for different angles of attack. It can be seen that the drag coefficient from the computed results decreases to the same limit as that from the results of both structured and unstructured codes.

Similarly, the grid convergence of lift from various solvers is shown in Fig. 6.19. The computed results are in high accordance with the results from the CFL3D structured solver.

Surface pressure

Fig. 6.20 represents the distribution of surface pressure on the viscous wall of the $3D$ hemisphere cylinder along the streamwise ($x-$) direction for different angles of attack. The solutions of USM3D and CFL3D are computed along the surface line that is corresponding to the 30° circumferential angle whereas that of FUN3D consists of all the angles [36]. The computed results are seen to over-plot the results from the other codes and are therefore in agreement with the reference results. Fig. 6.20 contains the surface pressure distribution from both the unstructured and structured grids for $AoA = 19°$ and this plot also agrees with the existing results.

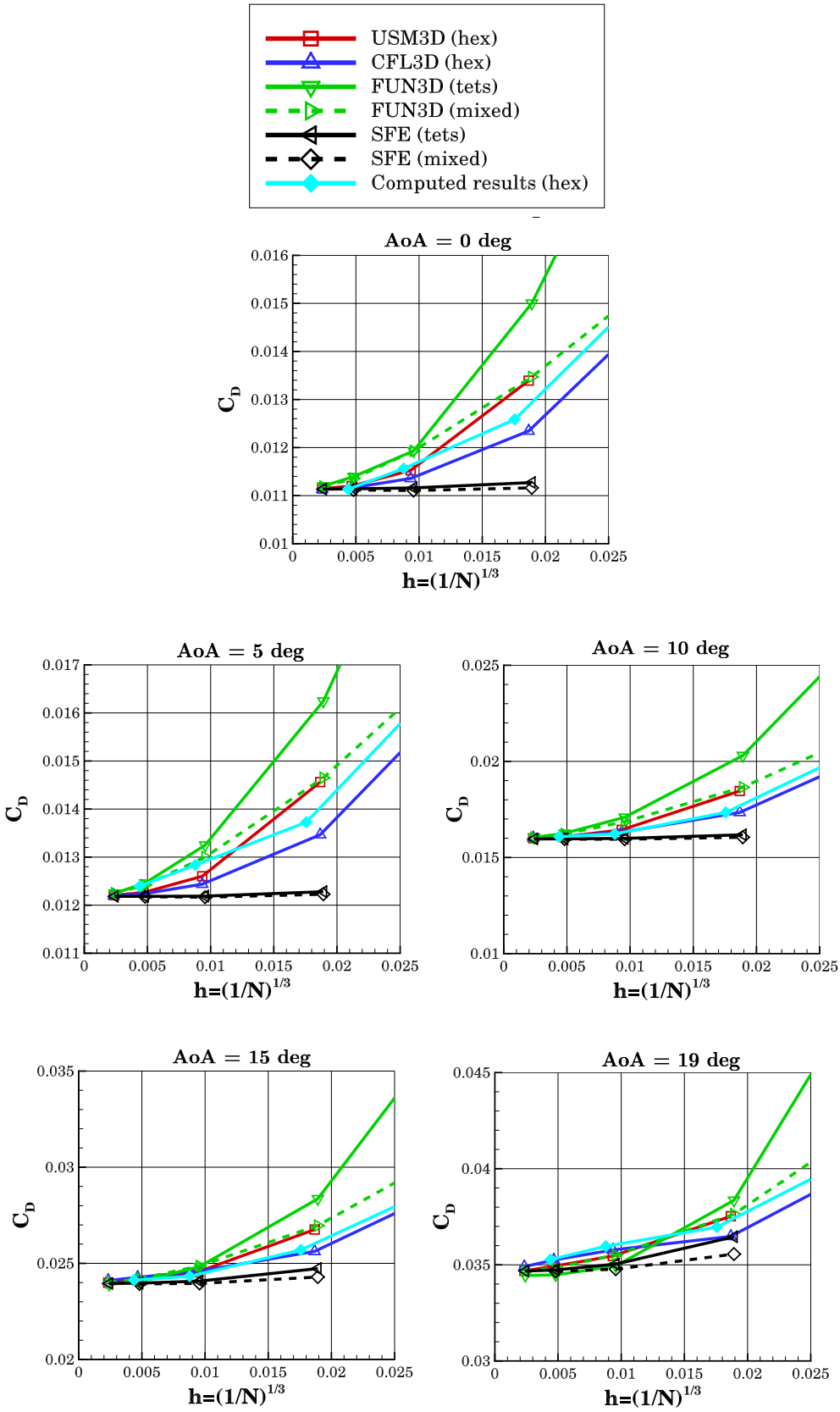

Figure 6.18: Grid convergence of drag for hemisphere cylinder at different angles of attack.

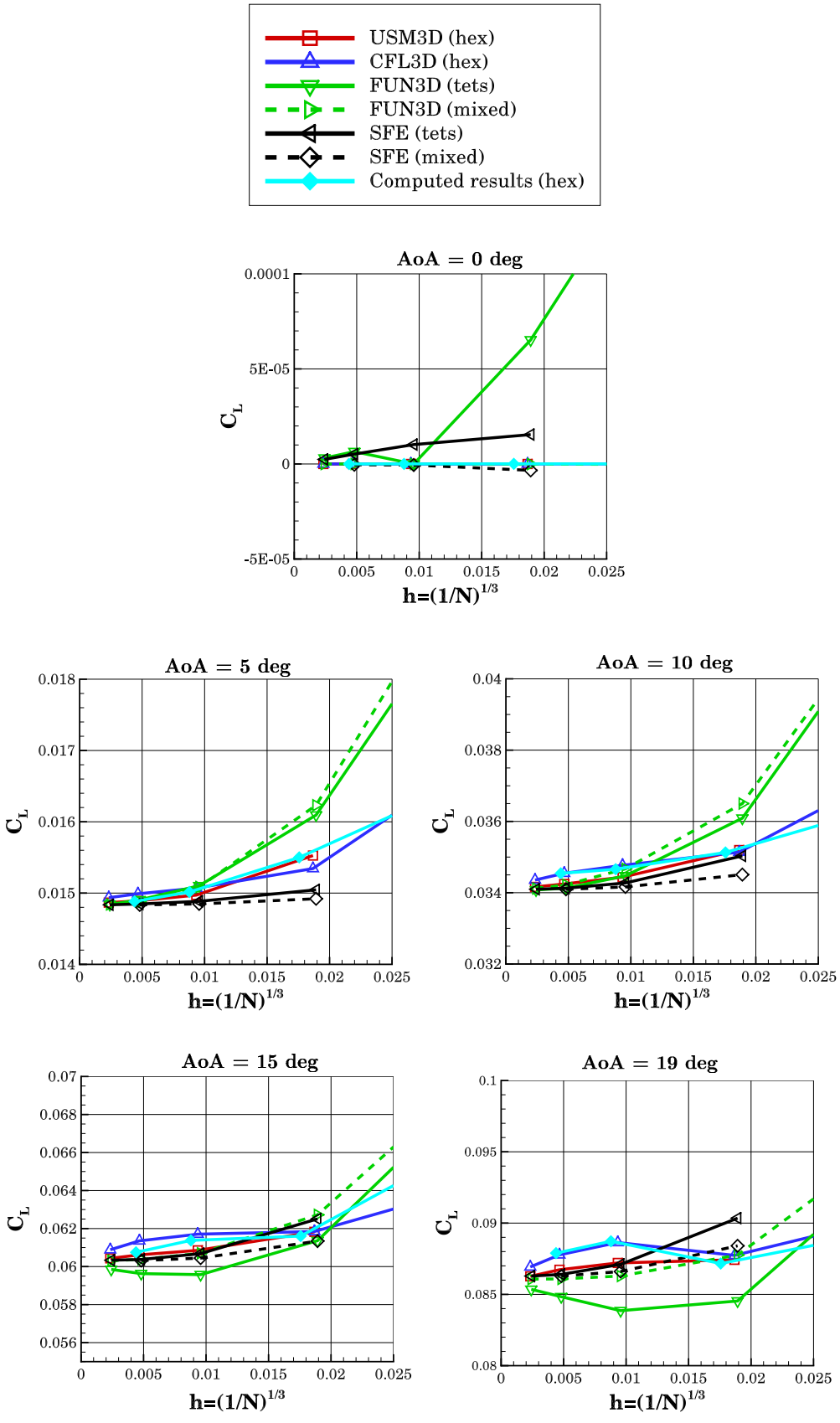

Figure 6.19: Grid convergence of lift for hemisphere cylinder at different angles of attack.

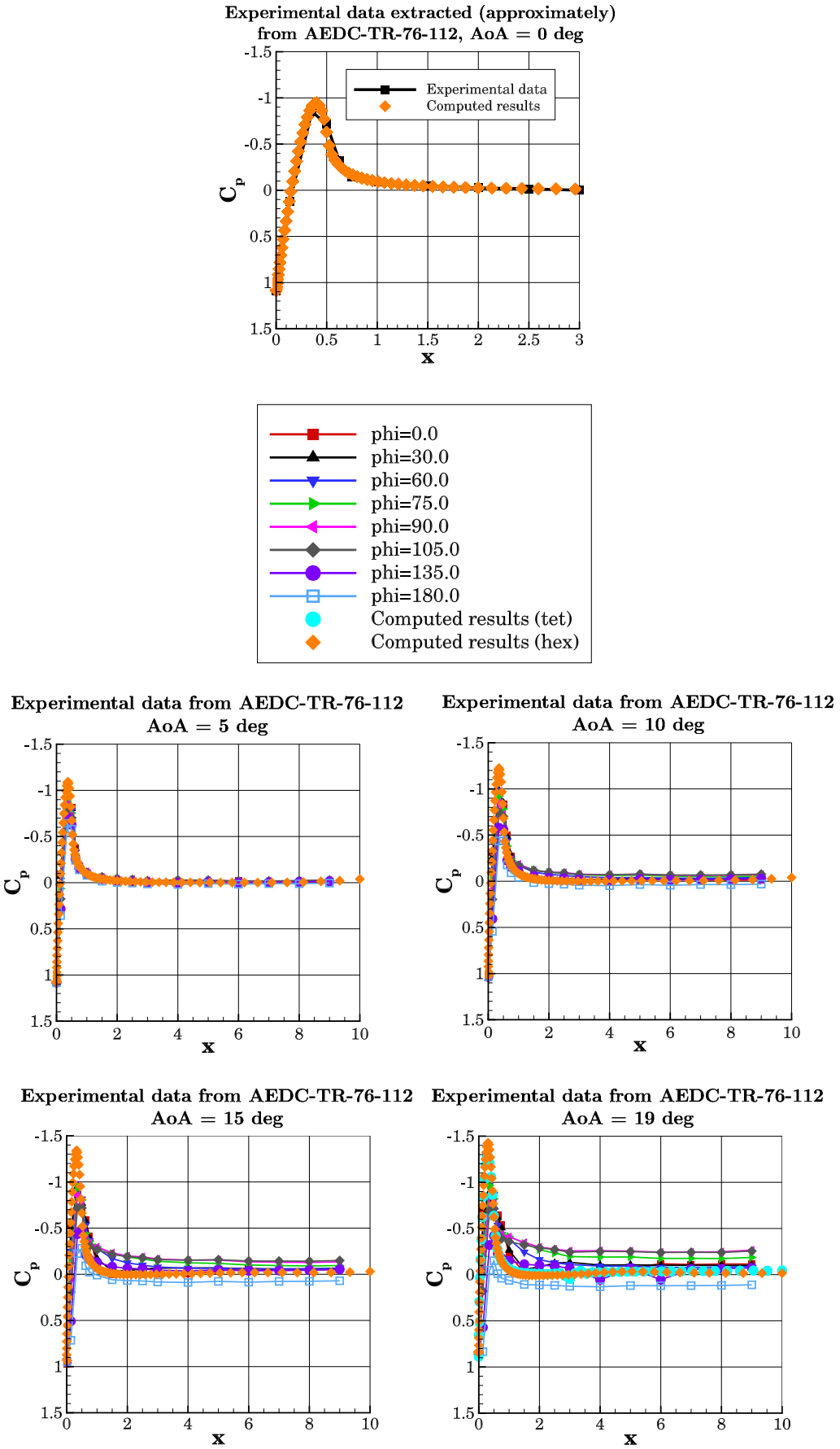

Figure 6.20: Surface pressure distribution over the cylinder at different angles of attack.

6.5 Case 5: 3D ONERA M6 Wing

Convergence studies

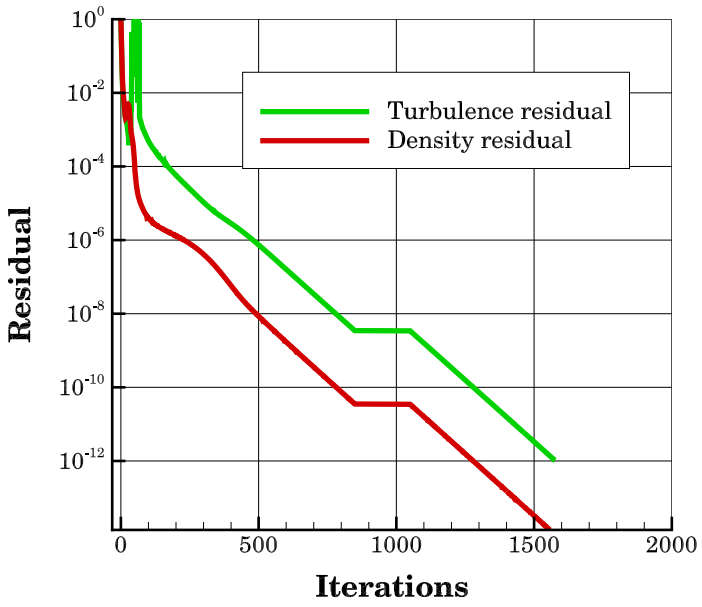

Figure 6.21: Residual convergence for the L3 grid for 3*D* ONERA M6 wing.

Results pertaining to the 3*D* ONERA M6 wing with respect to Sec. 5.5 are discussed in this section. Fig. 6.21 shows the convergence histories for density and turbulence residual versus multigrid cycle for the finest grid. A Full Approximation Scheme (FAS) with sg-cycle [18] is used for the experiment. The coarsest grid (L4) takes about 153 cycles to converge to the density residual tolerance of 10^{-15} whereas the finest grid takes 8, 174 cycles to converge for the same tolerance. Each grid is computed with different CFL numbers and it is specified that for mesh refinement, the corresponding CFL number is to be reduced.

Grid convergence of the aerodynamic coefficients of the ONERA M6 wing is shown in Fig. 6.22 and 6.23. The solutions from different codes are taken for reference. The FUN3D and USM3D have been computed for both structured and unstructured grids whereas CFL3D and the computed results are solutions from structured grids. The results from all the reference codes are computed without flux limiters [37]. Fig. 6.22 shows the grid convergence of lift and drag coefficients. The convergence isn't monotonic and therefore the order of the coefficients can not be deduced. Even so, the solutions from the different solvers are seen to approach the same limit value with mesh refinement.

The convergence of drag due to pressure and viscosity is shown in Fig. 6.23. These coefficients of drag occur with more definite slopes although the convergence pattern does not provide means that can serve for infinite-grid extrapolation. With the CFL3D and FUN3D (FV) solutions, it is noticed that the direction of convergence changes for the total and the pressure drag coefficients for the finest grid (L1). The computed results also exhibit the same property as the two mentioned codes. Similarly with the viscous drag coefficient computed from USM3D (tet) changes its direction with the finest grid. A monotonic convergence for all the drag coefficients is given only by USM3D (prism-hex). The relative variation of the drag components with mesh refinement is of more importance than that of the lift coefficient.

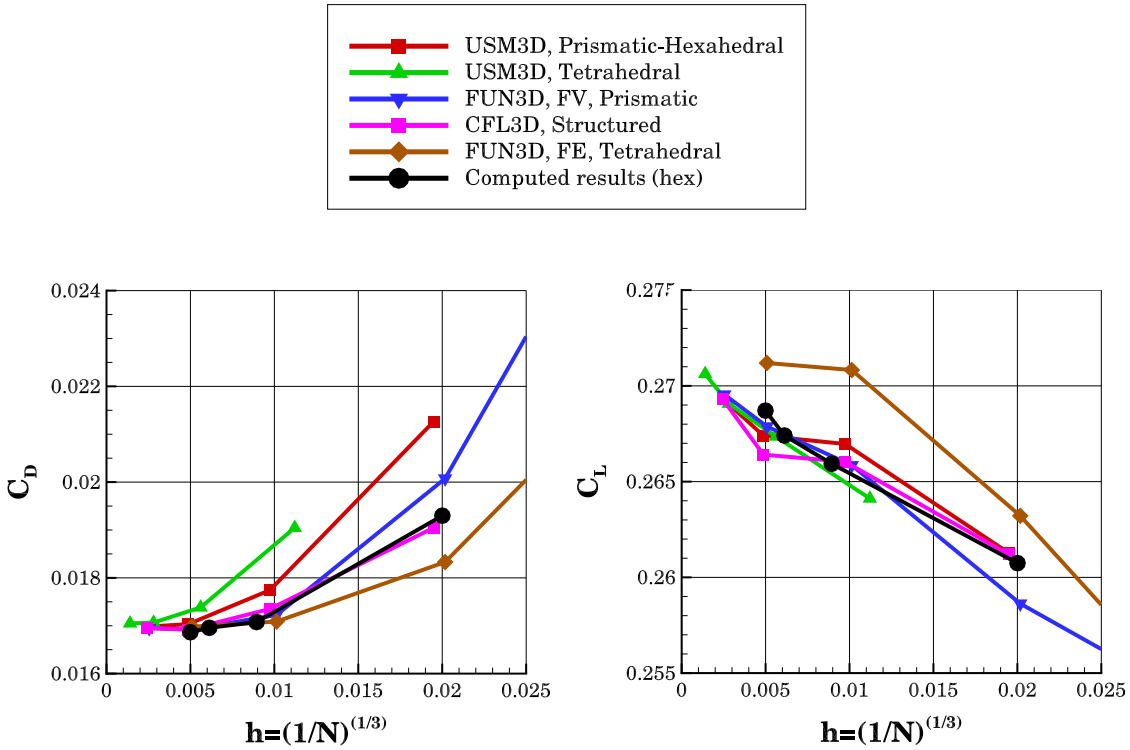

(a) Drag convergence. (b) Lift convergence.

Figure 6.22: Convergence behavior of forces for 3*D* ONERA M6 wing.

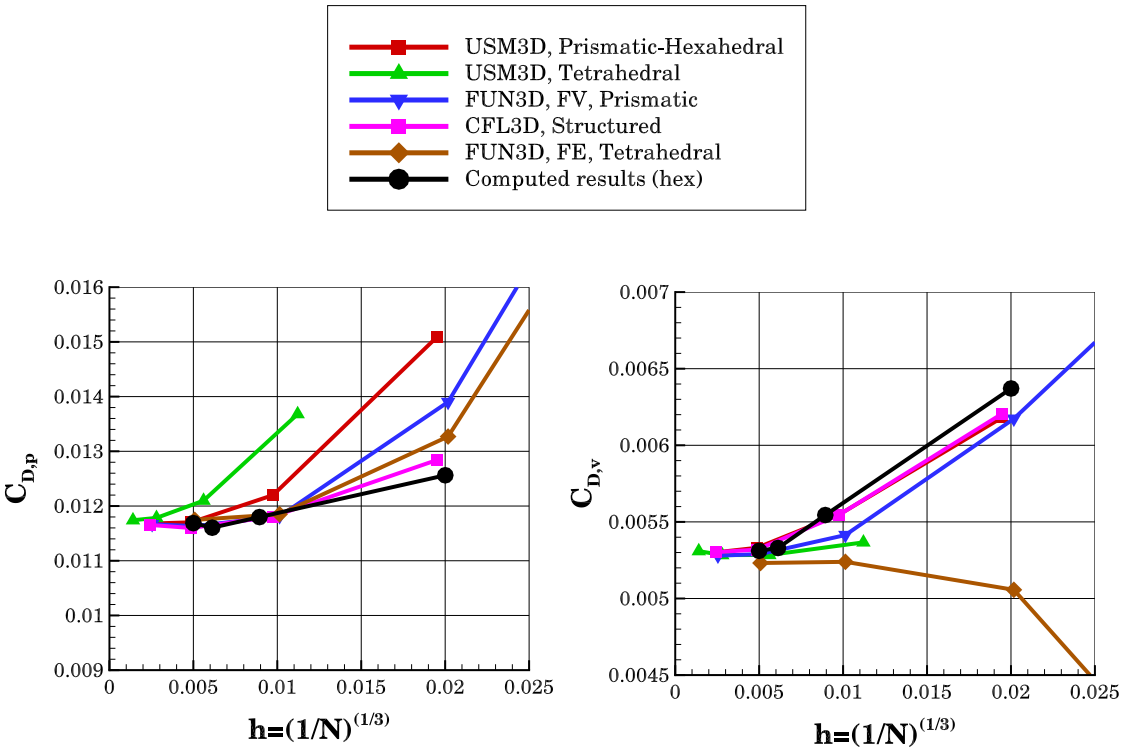

(a) Pressure drag. (b) Viscous drag.

Figure 6.23: Contribution to drag coefficient due to pressure and viscosity for 3*D* ONERA M6 wing.

Chapter 7

Summary and Conclulsion

For turbulent flows with high Reynolds number, suitable non-linear agglomeration multigrid methods were adopted to solve the Reynolds averaged Navier-Stokes equations.

The first part of the thesis deals with the definitions and basic assumptions concerning the RANS equations that are needed to describe the turbulence model along with the essential boundary conditions and solution algorithm are presented to find an approximate solution to the problems.

The second part is composed of five different benchmark test cases and the results pertaining to the above-mentioned solution algorithm with implicit RK schemes are discussed. Besides, comparisons are held with other solvers such as FUN3D, USM3D, etc., to study the efficiency and robustness of the scheme.

Nevertheless, it is not possible to determine the potential of the solver based on the five test cases. Further extended test cases are to be subjected to the discretization scheme to have a better understanding. This is done because the solution to the RANS equations, in general, does not have a fixed analytic solution. Also, the simplification of the multigrid scheme along with the CFL number seems to have a major impact on the solution algorithm in these test cases.

The study of the accuracy of the discretization scheme is one of the significant focus of this thesis and this is done through the grid convergence study with refinement. Through this, a notable conclusion is that it is not easy to determine accuracy. Two methods were employed to study the accuracy of the scheme: grid convergence of forces and grid conversions of pressure/skin friction coefficients. The former deals with the study that enables for the computation of order of convergence when the latter produces an outcome that is useful for comparison between solvers.

From the results of the experimental TAU code and the other reference solvers , a conclusion that is applicable to all the test cases can be drawn as follows [29]

- Although the limit at which the grids converge seem to be the same, each grid from the same family exhibits different convergence properties.
- The neighborhood of geometric singularities (sharp trailing edge, apex of cylinder, etc.,) is mostly observed to influence the accuracy and convergence with the mesh refinement; this localized grid resolution has a major effect than the differences in discretization schemes between the elements.
- With improved resolution in the vicinity of these singularities, the solutions from the different codes appear to be similar and when the global-scale is considered the results are almost equivalent to each other. The differences in pressure coefficients fall in a narrow range corresponding to the geometry of each of the test cases.
- Nonetheless asymptotic convergence order has not been observed even if accurate solutions from very fine grids are obtained.

The experimental results that are obtained through this thesis are a work in progress. The need to find the solutions for the RANS equations is essential in solving problems ranging from the complex applications of large-scale industries to the basic test flow cases prominent in the literature. When complications exist for solving these basic test cases the robustness of the solution methods are questioned, thereby losing its efficiency. Hence, by dealing with the simple cases, solution methods can be effectively tailored to suit the needs of large scale non-linear problems. Further extended test cases can be considered for the purpose of experiment with the groundwork that is provided by this thesis.

Bibliography

[1] Turbulence modeling resource website. `https://turbmodels.larc.nasa.gov/`.

[2] Stefan Langer, Axel Schwöppe, and Norbert Kroll. *The DLR Flow Solver TAU - Status and Recent Algorithmic Developments*. In *52nd Aerospace Sciences Meeting*, January 2014.

[3] S.Langer. *Preconditioned Newton methods to approximate solutions of the Reynolds averaged Navier-Stokes equations*. Technical report, Institut für Aerodynamik und Strömungstechnik, June 2018.

[4] C.-C.Rossow. *Analysis numerischer Methoden in der Aerodynamik*. Institut für Aerodynamik und Strömungstechnik, Braunschweig, 2018.

[5] S.Langer. *Algorithm zür Lösung der Euler und Navier-Stokes Gleichungen.* Institut für Aerodynamik und Strömungstechnik, Braunschweig, 2018.

[6] Christopher Rumsey. *Turbulence Modeling Verification and Validation (Invited)*. 01 2014.

[7] Christopher Rumsey, Brian Smith, and George Huang. *Description of a Website Resource for Turbulence Modeling Verification and Validation*. *40th AIAA Fluid Dynamics Conference*, 06 2010.

[8] Spalart-Allmaras Model. `https://turbmodels.larc.nasa.gov/spalart.html`.

[9] Steven R Allmaras, Forrester T Johnson, and Philippe R Spalart. *Modifications and Clarifications for the Implementation of the Spalart-Allmaras Turbulence Model*. Seventh International Conference on Computational Fluid Dynamics (ICCFD7) Bid Island, Hawaii, 2012.

[10] J. Blazek. *Computational Fluid Dynamics: Principles and Applications*. Elsevier, New York, 2nd ed edition, 2005. ISBN:978-0-08-043944-0.

[11] Boris Diskin, James Thomas, Eric Nielsen, Jeffery White, and Hiroaki Nishikawa. *Comparison of Node-Centered and Cell-Centered Unstructured Finite-Volume Discretizations Part I: Viscous Fluxes*. In *47th AIAA Aerospace Sciences Meeting including The New Horizons Forum and Aerospace Exposition*, Orlando, Florida, January 2009. American Institute of Aeronautics and Astronautics. ISBN:978-1-60086-973-0.

[12] R. Swanson and Eli Turkel. *Artificial dissipation and central difference schemes for the Euler and Navier-Stokes equations*. In *8th Computational Fluid Dynamics Conference*, Honolulu,HI,U.S.A., June 1987. American Institute of Aeronautics and Astronautics.

[13] R. Swanson and Eli Turkel. *On Central-Difference and Upwind Schemes*. 1990.

[14] R C Swanson, R Radespiel, and E Turkel. *Comparison Of Several Dissipation Algorithms for Central Difference* schemes.

[15] S.K. Godunov and I Bohachevsky. *Finite difference method for numerical computation of discontinuous solutions of the equations of fluid dynamics*. 47(89) No. 3, 1959.

[16] Addisu Dagne Zegeye. *Compressible flow*. `https://www.slideshare.net/ADDISUDAGNEZEGEYE?utm_campaign=profiletracking&utm_medium=sssite&utm_source=ssslideview`.

[17] S. Prabhakara and M.D Deshpande. *The No-Slip Boundary Condition in Fluid Mechanics*. 2004.

[18] U. Trottenberg, C. Oosterlee, and A. Schuller. *Multigrid*. Academic Press, 2001.

[19] Hiroaki Nishikawa, Boris Diskin, James Thomas, and Dana Hammond. *Recent Advances in Agglomerated Multigrid*.

[20] Stefan Langer. *Agglomeration multigrid methods with implicit Runge–Kutta smoothers applied to aerodynamic simulations on unstructured grids*. *Journal of Computational Physics*, 277(11):72–100, August 2014.

[21] Michael Park, Elizabeth Lee-Rausch, and Christopher Rumsey. *FUN3D and CFL3D computations for the first high lift prediction workshop*. *49th AIAA Aerospace Sciences Meeting Including the New Horizons Forum and Aerospace Exposition*, 01 2011.

[22] Robert I. McLachlan. *The boundary layer on a finite flat plate*. 3(2), February 1991.

[23] T Hsieh. *An Investigation of Separated Flow about a Hemisphere-Cylinder at 0- to 19-Deg Incidence in the Mach Number Range from 0.6 to 1.5*. Arnold Air Force Station, Tennessee. AEDC-TR-76-112.

[24] S. Le Clainche, D. Rodríguez, V. Theofilis, and J. Soria. *Formation of Three-Dimensional Structures in the Hemisphere-Cylinder*. *AIAA Journal*, 54(12):3884–3894, 2016.

[25] Hiroaki Nishikawa and Boris Diskin. *Customized Grid Generation Codes for Benchmark Three-Dimensional Flows*. In *2018 AIAA Aerospace Sciences Meeting*, Kissimmee, Florida, January 2018. American Institute of Aeronautics and Astronautics. ISBN: 978-1-62410-524-1.

[26] Vincent Gleize, Antoine Dumont, Julien Mayeur, and Daniel Destarac. *RANS simulations on TMR test cases and M6 wing with the Onera elsA flow solver*. 53rd AIAA Aerospace Sciences Meeting. Kissimmee, Florida. American Institute of Aeronautics and Astronautics. ISBN:978-1-62410-343-8.

[27] Daniel Destarac and Antoine Dumont. *ONERA M6 Wing Test-Case, Original and TMR*. September 2016.

[28] Boris Diskin and Hiroaki Nishikawa. *Evaluation of Multigrid Solutions for Turbulent Flows*. 01 2014.

[29] B. Diskin, J. Thomas, C. L. Rumsey, and A. Schwoeppe. *Grid Convergence for Turbulent Flows*. Kissimmee, Florida, January 2015. American Institute of Aeronautics and Astronautics.

[30] Boris Diskin, James L. Thomas, Christopher L. Rumsey, and Axel Schwöppe. *Grid-Convergence of Reynolds-Averaged Navier–Stokes Solutions for Benchmark Flows in Two Dimensions*. *AIAA Journal*, 54(9):2563–2588, 2016.

[31] J McCroskey. *A Critical Assessment of Wind Tunnel Results for the NACA 0012 Airfoil*. (AGARD CP-429):23, July 1988.

[32] Ira H. Abbott and Albert E. von Doenhoff. *Theory of Wing sections: including a summary of airfoil data*. Dover Publications, Inc., New York.

[33] N. Gregory and C. L. O'reilly. *Low-Speed Aerodynamic Characteristics of NACA 0012 Aerofoil Section, including the Effects of Upper-Surface Roughness Simulating Hoar Frost*. Aerodynamics Division, N.P.L., London, 1970.

[34] Ladson and Charles L. *Effects of independent variation of Mach and Reynolds numbers on the low-speed aerodynamic characteristics of the NACA 0012 airfoil section*. Technical report, Oct 1988.

[35] Charles L Ladson, Aequilla S Hill, and WUliam G Johnson. *Pressure Distributions from High Reynolds Number Transonic Tests of an NACA 0012 Airfoil in the Langley 0.3-Meter Transonic Cryogenic Tunnel*.

[36] Boris Diskin, James.L Thomas, Mohagna J. Pandya, and Christopher L. Rumsey. *Reference Solutions for Benchmark Turbulent Flows in Three Dimensions*. National Institute of Aerospace, Hampton, VA 23666. American Institute of Aeronautics and Astronautics.

[37] Boris Diskin, Kyle Anderson, Mohagna Pandya, Christopher Rumsey, James Thomas, Yi Liu, and Hiroaki Nishikawa. *Grid Convergence for Three Dimensional Benchmark Turbulent Flows*. National Institute of Aerospace, Hampton, VA 23666, 01 2018. American Institute of Aeronautics and Astronautics.

DLR-IB-AS-BS-2020-91

Investigation of Benchmark Turbulent Flows

Akshaya Govindan Nair Rajendran

Verteiler:

Institutsbibliothek	1 Exemplar
Verfasser	3 Exemplare
Institutsleitung	1 Exemplar
Abteilungsleiter	1 Exemplar
Deutsche Bibliothek in Frankfurt/Main	2 Exemplare
Niedersächsische Landesbibliothek Hannover	1 Exemplar
Techn. Informationsbibliothek Hannover	1 Exemplar
Zentralbibliothek BS	2 Exemplare
Zentralarchiv GÖ	1 Exemplar
Reserve	5 Exemplare